Gesellschaft für Anlagen- und Reaktorsicherheit (GRS) mbH

Final Evaluation of the Project “Thermal Simulation of Drift Emplacement“ (TSDE-Project)

Final Report

GRS - 194

Gesellschaft für Anlagen- und Reaktorsicherheit (GRS) mbH

Final Evaluation of the Project "Thermal Simulation of Drift Emplacement" (TSDE-Project)

Final Report

Tilmann Rothfuchs
Jürgen Dittrich
Johannes Droste
Jürgen Müller
Chun-Liang Zhang

November 2003

Anmerkung:

Die diesem Bericht zugrundeliegenden Arbeiten wurden mit Mitteln des Bundesministeriums für Wirtschaft und Technologie (BMWi) unter dem Förderkennzeichen 02E9269 gefördert.

Die Arbeiten wurden von der Gesellschaft für Anlagen- und Reaktorsicherheit (GRS) mbH durchgeführt.

Die Verantwortung für den Inhalt dieser Veröffentlichung liegt allein bei den Autoren.

GRS - 194
ISBN 3-931995-62-3

Deskriptoren:
Deformation, Endlagerung, Experiment, Langzeitsicherheit, Modell, Permeabilität, Porosität, Salz, Spannung, Technische Barriere, Temperatur, Überwachung, Verifikation

Foreword

In the Federal Republic of Germany, two emplacement concepts have been developed for the disposal of heat generating waste from nuclear power plants. The drift emplacement concept comprises the direct disposal of spent fuel assemblies by packaging the fuel rods in self shielding Pollux casks which are emplaced in the drifts of a repository in rock salt. The remaining volume of the drifts will be backfilled with crushed salt immediately after the emplacement of the casks. The borehole emplacement concept provides the disposal of vitrified high-level waste in canisters which are stacked in vertical boreholes beneath repository drifts. The upper part of the boreholes and the annulus around the canisters will be backfilled with crushed salt.

The "Thermal Simulation of Drift Emplacement" (TSDE) large-scale test had been performed in the Asse salt mine to demonstrate the technology of drift emplacement and to study the thermomechanical effects of the direct disposal of spent fuel. For the final evaluation of the test results, one test drift was uncovered and post-test investigations were performed.

The work was funded by the Bundesministerium für Bildung, Wissenschaft, Forschung und Technologie (BMBF) and since 2002, by the Bundesministerium für Wirtschaft und Arbeit (BMWA) of the Federal Republic of Germany. The test had been started in 1985 within the framework of the R&D-programme "Direct Disposal of LWR-Fuel Elements" which ended in December 1995. From January 1996 until March 2000, the GRS studies in the TSDE project had been continued under the contract number 02-E-8805-1. Since April 2000, the post-test investigations of GRS were performed under the contract number 02-E-9269. From August 1994 until April 1995, the investigations on backfill compaction and gas release had been funded by the European Commission under contract number FI2W-CT94-0127. From January 1996 to December 1998, the project had been funded by the European Commission as part of the BAMBUS ("Backfill and Material Behaviour in Underground Salt Repositories") project under the contract number FI4W-CT95-0009. From August 2000 to April 2003, uncovering and post-test investigations were funded by the European Commission as part of the BAMBUS-II ("Backfill and Material Behaviour in Underground Salt Repositories, Phase II") project under the contract number FIKW-CT-2000-00051.

During project performance, several partners were involved. Project co-ordination was in responsibility of the Forschungszentrum Karlsruhe GmbH - Projektträger für

Entsorgung (FZK-PTE), since January 2000, Projektträger für Wassertechnologie und Entsorgung (FZK-PtWT+E). In the preliminary phase of the *in-situ* experiment, the Deutsche Gesellschaft zum Bau und Betrieb von Endlagern für Abfallstoffe (DBE) had been responsible for heater cask emplacement and backfilling. Test field instrumentation had been carried out by the Bundesanstalt für Geowissenschaften und Rohstoffe (BGR) and the GSF - Forschungszentrum für Umwelt und Gesundheit GmbH - Institut für Tieflagerung (IfT) which was taken over by GRS in July 1995.

During the *in-situ* experiment, the GRS - Repository Safety Research Division (until June 1995: GSF-IfT) was concerned with the test operation and *in-situ* measurements with DBE being subcontractor and responsible for heater operation and testing of measuring techniques. Uncovering of the test field was in responsibility of DBE. Post-test analyses on retrieved measuring instruments were performed by GRS, BGR, and DBE. A large number of instrument examinations and re-calibrations were kindly conducted free of charge by the Glötzl Gesellschaft für Baumeßtechnik mbH.

Within the framework of the BAMBUS-I and BAMBUS-II projects, laboratory studies and model calculations were performed. Laboratory investigations on crushed salt were carried out by GRS, BGR, FZK/INE, the Institut für Gebirgsmechanik Leipzig (IfG), and the Groupement pour l'Etude de Structures Souterraines de Stockage (G.3S) / France. Laboratory investigations on rock salt were conducted by BGR, IfG, G.3S, and the U.S. Department of Energy - Carlsbad Field Office (US DOE-CBFO) / USA. Numerical calculations were performed by BGR, DBE, FZK/INE, G.3S, the Empresa Nacional de Residuos Radiactivos S. A. (ENRESA-CIMNE) / Spain, the Universitat Politécnica de Catalunya (UPC) / Spain, and the Nuclear Research and Consultance Group (NRG) / The Netherlands.

This report presents the results of the post-test investigations of GRS from August 2000 until April 2003. A detailed description of the GRS *in-situ* investigations during the heating phase and the following cool-down phase until March 2000 is given in the reports:

GRS-127 The TSS Project: Thermal Simulation of Drift Emplacement, Final Report Phase 2.

GRS-173 Experimental Investigations on the Backfill Behaviour in Disposal Drifts in Rock Salt (VVS-Project), Final Report.

Abstract

The Thermal Simulation of Drift Emplacement (TSDE) full-scale demonstration test was performed in the Asse salt mine in Germany to study the thermomechanical effects of the direct disposal of spent-fuel elements in a salt repository. From September 1990 until February 1999, electrically heated casks simulating spent-fuel containing Pollux casks were operated under repository-relevant conditions in two test drifts which were backfilled with crushed salt. Backfill and surrounding rock salt behaviour were observed by *in-situ* measurements. The results were compared with the results of numerical calculations for the validation of models which are used to predict the evolution of crushed salt compaction and permeability.

The geotechnical investigation programme, which included temperature, deformation, and stress measurements, required special fabrication of the measuring instruments due to the harsh environment application. The design of the measuring equipment proved to be successful during the long testing period. However, differences were observed between the results of numerical simulations and experimental data, especially regarding drift closure and backfill compaction.

For evaluation of the *in-situ* test and validation of the measuring results, one test drift was re-opened. Drift excavation started in late August 2000. Backfill samples were taken for post-test laboratory analysis of the achieved backfill compaction. The instruments which had been located in the backfill and at the surface of the heater casks were recovered for inspection and re-calibration after more than a decade of operation.

With the backfill porosity determinations in the laboratory, the results of *in-situ* measurements and model calculations were confirmed. Until re-opening of the test field, measurements and predicted data could not be directly compared. The calculated data were only valid for the central part of the test field, but corresponding measuring data were not available due to early instrument failures. Therefore, measuring data from the peripheral part of the heated area had to be taken to assess the compaction rates during the heating phase. Basing on the laboratory results and a new approach for the determination of the *in-situ* porosity, backfill compaction was re-calculated. The *in-situ* porosities determined in this way showed a much better agreement with the predicted data and confirmed the used models excellently.

Permeability measurements on backfill samples corresponded to the value derived *in situ* during the heating period. From additional permeability tests on large core samples at different porosities, a relation between permeability and porosity was determined. Laboratory hydrostatic compression tests on backfill samples indicated an *in-situ* backfill pressure that was slightly higher than the backfill pressure that had been observed *in situ* at higher temperatures and very low compaction rates. From the deviatoric compression tests, the stress – strain behaviour was obtained indicating very large deformation even after the peak strength was reached. The major component of the deformation was plastic. Comparisons with other laboratory results on Asse crushed salt allowed an appraisal of the strength of the compacted TSDE backfill.

Mineralogical investigations revealed a heterogeneous grain size distribution as well as a very high porosity of the backfill material. The observations of microstructures and textures did not confirm the initial assumption of plastic deformation and/or dynamic or static recrystallization of salt grains. The residual water content was identical to the average water content of rock salt. The residual gas concentrations corresponded to normal mine air.

The measuring equipment had been designed for a three to five years testing period, but was operated over almost ten years under final repository conditions. *In-situ* and post-test investigations revealed that the robust gauge design and the deployed sensors were very successful. Most failures were caused by damaged measuring lines. The re-calibration results proved the high reliability and low sensor drift of the applied sensors. Basing on the post-test analyses, the *in-situ* measurements of the TSDE test could be assessed as very confidential. The applied measuring systems proved to be suitable for the long-term monitoring of a final repository.

Zusammenfassung

Zum Nachweis der Realisierbarkeit der direkten Endlagerung bestrahlter Brennelemente in einem Endlager in Steinsalzformationen wurde der großmaßstäbliche Demonstrationsversuch "Thermische Simulation der Streckenlagerung" (TSS) im Salzbergwerk Asse durchgeführt, bei dem zwei mit Salzgrusversatz verfüllte Versuchsstrecken von September 1990 bis Februar 1999 mit elektrisch betriebenen Erhitzern aufgeheizt wurden. Ziel des Versuches war die experimentelle Untersuchung des Verhaltens von Streckenversatz und umgebendem Gebirge unter repräsentativen Einlagerungsbedingungen, d. h. unter der Einwirkung von Wärme und Gebirgsdruck. Die Ergebnisse von Messungen und numerischen Rechnungen wurden verglichen, um die Rechenmodelle zur Simulation des Kompaktions- und Durchlässigkeitsverhaltens von Salzgrusversatz zu validieren.

Das geotechnische Untersuchungsprogramm umfasste Temperatur-, Verformungs- und Spannungsmessungen. Die ungewöhnlichen Versuchsbedingungen erforderten die Entwicklung einer speziellen Messinstrumentierung, die sich während der langen Versuchsdauer als sehr erfolgreich erwies. Zwischen den Ergebnissen der Messungen und der Prognoserechnungen ergaben sich jedoch Abweichungen insbesondere bei den Streckenkonvergenzen und der Versatzkompaktion.

Zur Bewertung des *In-situ*-Versuches und zur Validierung der Messergebnisse wurde eine der beiden Versuchsstrecken ab Ende August 2000 wieder aufgefahren. Während der Auffahrung wurden Versatzproben für Laboruntersuchungen der erreichten Versatzkompaktion entnommen. Die im Versatz und auf der Oberfläche der Erhitzerbehälter installierte Messinstrumentierung wurde zur Begutachtung und zur Rekalibrierung der Messgeber nach über zehnjähriger Betriebsdauer geborgen.

Die Porositätsbestimmungen im Labor bestätigten die Ergebnisse der *In-situ*-Messungen und der Prognoserechnungen. Vor der Auffahrung des Versuchsfeldes war kein direkter Vergleich zwischen Messdaten und Prognoserechnungen möglich, da die Berechnungen nur für den zentralen Erhitzerbereich gültig waren. Für diesen Bereich standen jedoch keine Messergebnisse zur Verfügung, da die entsprechenden Messinstrumente bereits frühzeitig ausgefallen waren. Daher wurden für die Ermittlung der Versatzkompaktion während der Aufheizung Messdaten aus dem randlichen Erhitzerbereich herangezogen. Auf der Grundlage der Laborergebnisse und mit Hilfe

eines neuen Ansatzes zur Ermittlung der *In-situ*-Porositätswerte aus den Konvergenzmessdaten wurde der Verlauf der Versatzkompaktion neu berechnet. Die auf diese Weise ermittelten *In-situ*-Porositätswerte zeigten eine wesentlich bessere Übereinstimmung mit den Prognoserechnungen und bestätigten die verwendeten Stoffgesetze.

Die Labormessungen der Versatzpermeabilitäten zeigten eine gute Übereinstimmung mit dem Wert, der während der Aufheizung *in situ* ermittelt wurde. Mit zusätzlichen Permeabilitätstests an großen Bohrkernen, die bei verschiedenen Porositäten durchgeführt wurden, konnte eine Porositäts-Permeabilitäts-Beziehung abgeleitet werden. Mit hydrostatischen Druckversuchen wurde im Labor an Großbohrkernen des kompaktierten Versatzes der im In-situ-Versuch erreichte Versatzdruck bestimmt. Der ermittelte Wert lag über dem *in situ* bei höheren Temperaturen und sehr niedrigen Kompaktionsraten gemessenen Versatzdruck. Mit Hilfe deviatorischer Druckversuche wurde das Spannungs-Verformungs-Verhalten ermittelt, das auch nach Erreichen der maximalen Festigkeit starke Verformungen zeigte. Die Hauptkomponente der Verformung war plastisch. Vergleiche mit anderen Laborergebnissen an Asse-Salzgrus ermöglichten eine Bewertung der Festigkeit des kompaktierten TSS-Versatzmaterials.

Mineralogische Untersuchungen ergaben eine heterogene Korngrößenverteilung und eine sehr hohe Porosität des Versatzmaterials. Die ursprüngliche Annahme einer plastischen Deformation und/oder dynamischen oder statischen Rekristallisation von Salzkörnern konnte an den untersuchten Mikrostrukturen und -texturen nicht bestätigt werden. Die Restfeuchte des Versatzes war identisch mit dem durchschnittlichen Wassergehalt von Steinsalz. Die Restgaskonzentrationen entsprachen normaler Grubenluft.

Die Messinstrumentierung war ursprünglich für eine Versuchsdauer von drei bis fünf Jahren ausgelegt worden. Sie wurde jedoch über einen Zeitraum von fast zehn Jahren unter Endlagerbedingungen betrieben. Sowohl die *In-situ*-Messungen, als auch die Nachuntersuchungen bestätigten das erfolgreiche Konzept der Messinstrumentierung und der verwendeten Sensoren. Die meisten Ausfälle während der Versuchsphase waren auf defekte Messleitungen zurückzuführen. Die Rekalibrierungsergebnisse zeigten die hohe Zuverlässigkeit und niedrige Gerätedrift der eingesetzten Messgeber. Durch die Nachuntersuchungen konnte belegt werden, dass die *in situ* gewonnenen Messdaten als sehr zuverlässig anzusehen sind. Die eingesetzten Messsysteme erwiesen sich als geeignet zur Langzeitüberwachung eines Endlagers.

Table of Contents

1 Introduction

The *in-situ* experiment "Thermal Simulation of Drift Emplacement" (TSDE) /TPL 93/ had been performed from September 1990 until February 1999. The most important objective was to investigate the suitability of crushed salt as backfill in disposal drifts containing spent fuel in self-shielding Pollux disposal casks.

The experiment was conducted in two parallel test drifts on the 800-m level of the Asse mine (Fig. 1.1). Each test drift was 70 m long, 3.5 m high and 4.5 m wide and contained three simulated Pollux casks having a length of 5.5 m, a diameter of 1.5 m, and a mass of 65 tons. The Pollux cask mock-ups were electrically heated with a nominal heater power of 6.4 kW. In addition to the two test drifts, the test field included several observation and access drifts on the 800-m level and on the 750-m level. Measuring niches along the observation and access drifts contained the power supply and the data acquisition systems.

Numerous boreholes, which had been drilled from the observation drifts into the vicinity of the test drifts and from the test drifts into the surrounding rock salt, were equipped with various measuring gauges. Other devices had been installed in the backfill and at the surface of the heater casks.

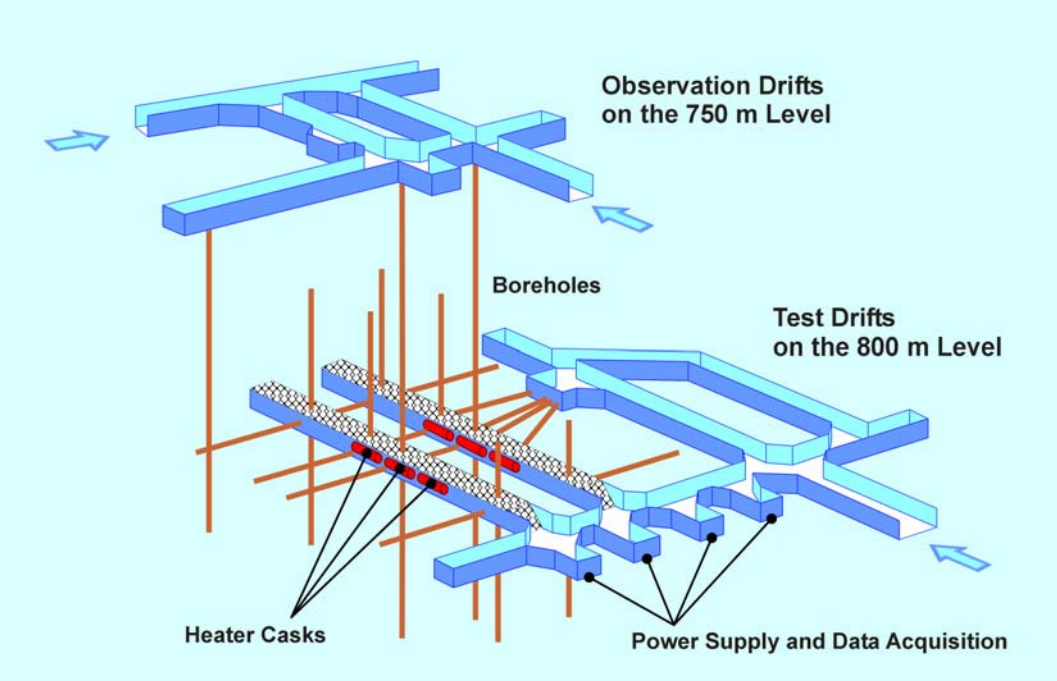

Fig. 1.1 Conceptual view of the TSDE test field in the Asse mine

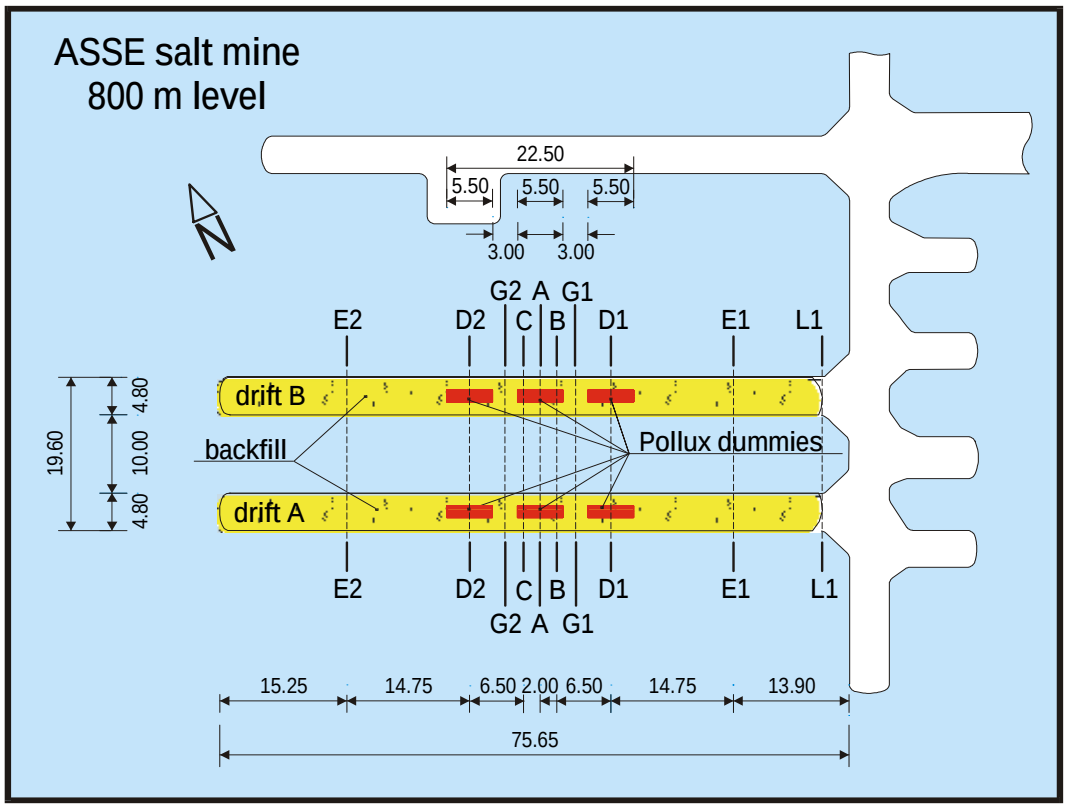

Fig. 1.2 Plan view of the TSDE test field

The measuring instruments were installed in selected monitoring cross sections (Fig. 1.2). After installation of the heaters and the geotechnical instrumentation, the drifts were backfilled with crushed salt. Over the duration of the experiment, temperatures, stresses, backfill density, rock deformations, and gas generation were measured.

Already after five months of heating, a temperature of 210 °C was reached at the heater cask surface (Fig. 1.3). Subsequently, the temperatures decreased slowly to 170 °C because of the increasing thermal conductivity of the compacting backfill /DRO 01/.

Heating caused a rapid temperature increase in the surrounding rock salt inducing high thermal stresses and thus accelerated drift closure which in turn led to the compaction of the backfill material in the drifts. Thus, backfill porosity was reduced from initially 0.35 to 0.245 - 0.206 at the termination of the heating phase.

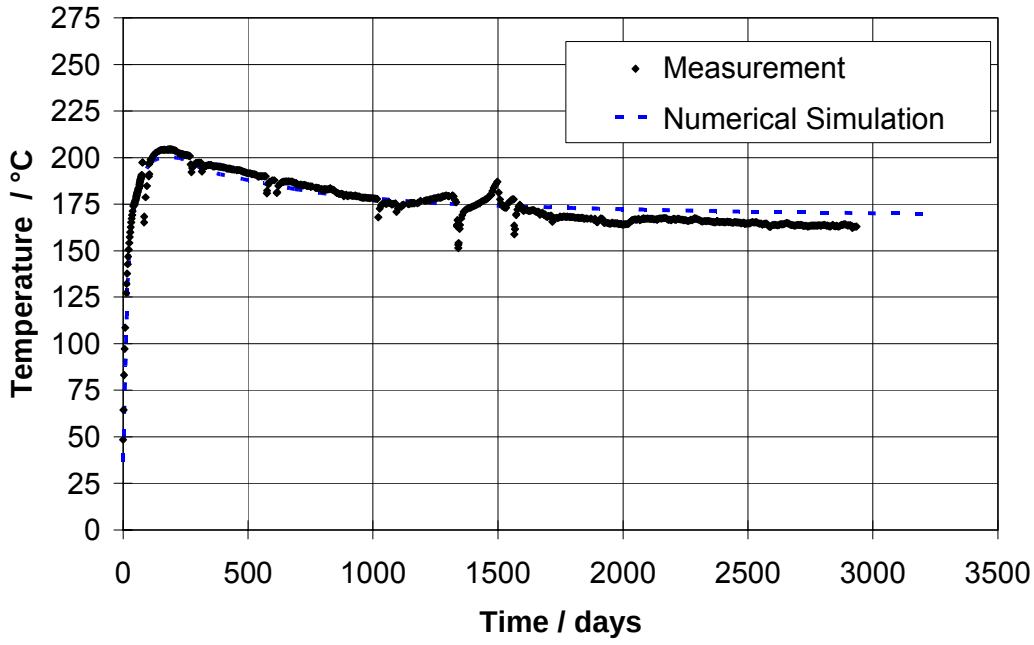

Fig. 1.3 Temperature increase at the central heater cask surface

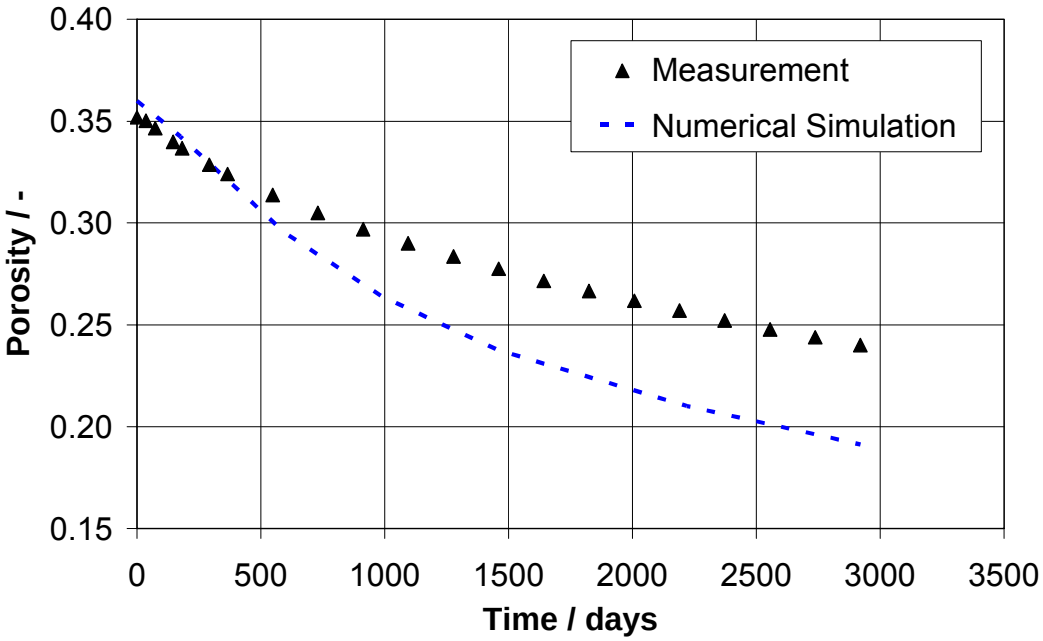

Fig. 1.4 Development of backfill porosity

The measured and calculated /PUD 98/ decrease of backfill porosity is shown in Figure 1.4. The comparison indicates an overestimation of backfill compaction in the warmer central part of the test field thus suggesting a stiffer backfill behaviour *in situ* compared to laboratory experiments on the basis of which constitutive equations and material parameters have been developed. But due to early instrument failure in the central heater area, convergence measuring data were only available from the peripheral heaters. Thus, only these values could be compared with the predictive calculations which had been performed for the central heater area.

To evaluate the true porosity distribution in the backfill especially in the central heater area and to enable post-test inspection and re-calibration of the installed measuring instruments, the northern test drift B (Fig. 1.2) was re-opened between August 2000 and May 2001. In the following, the results of the post mortem investigations of GRS are presented.

2 Objectives

The post-test investigations of GRS comprised the determination of the properties of the compacted backfill and the post-test analysis of the used measuring instruments.

In detail the objectives were:

- to sample systematically specimens from the compacted backfill to analyse the final distribution of backfill porosity and permeability at the termination of the *in-situ* test,
- to analyse the strength of the compacted backfill,
- to investigate and compare the post-test compaction behaviour of pre-compacted backfill and unconsolidated backfill used in the laboratory to determine the material parameters for actual constitutive models,
- to quantify the mineralogical and chemical backfill properties by optical and electron microscopy,
- to inspect and re-calibrate the used measuring instruments after more than a decade of operation for quality insurance and validation of the measurement results, and for providing a basis for recommendations of monitoring instruments for future deployment in a salt repository.

.

3 Uncovering of the Test Field

Uncovering of the test field was necessary to provide access to the test drifts in the TSDE test field. Thus it was possible to take samples of the compacted backfill and to retrieve the instruments for post-test analyses.

Prior to the start of excavation, a master plan was developed by the project partner DBE for excavating backfill material, taking samples from backfill material and rock salt, recovering instruments, heaters and corrosion specimens, and for performing *in-situ* permeability measurements. The original intention was to dismantle both test drifts. But with regard to the cost/benefit relation it was decided to dismantle only one drift. The northern test drift B was selected as only this test drift had been equipped with corrosion specimens.

Excavation started at the end of August 2000 after the temperatures in the drift had decreased to a level acceptable for working. Excavation and dismantling activities were finished within less than one year in May 2001. The work was done by staff from the Asse mine and supervised by DBE.

Excavation work started with the removal of backfill material from the drift entrance area. In the non-heated area up to the first measuring cross section E1, the backfill could be removed by a loader (Fig. 3.1). Subsequently, excavation of the increasingly compacted backfill was proceeded by a continuous miner (Fig. 3.2). In the vicinity of the measuring cross sections, manual work was required (Fig. 3.3 and 3.4). To enable the retrieval of the heater casks, the drift had to be widened into the surrounding rock salt by means of a continuous miner. Around the casks, the backfill material was also removed manually. Then, the casks were dismantled and retrieved (Fig. 3.5). The backfill material was removed in the first half of the drift up to the third heater cask.

During the excavation work, inspections were made at characteristic locations and samples were taken for further laboratory tests. For the determination of backfill porosity and permeability, samples were taken by drilling or slot cutting into the compacted backfill material. In Figure 3.6, the boreholes and slots in the backfill remaining from sampling at cross section B^{+1} are shown. According to the requirements of the various compaction and strength tests, boreholes were cored with a diameter of 101 mm or 280 mm (Fig. 3.7) and prepared for shipment (Fig. 3.8).

Fig. 3.1 Backfill excavation in the non-heated area using a loader

Fig. 3.2 Backfill excavation in the heated area using a continuous miner

Fig. 3.3 Manual recovery of a temperature sensor

Fig. 3.4 Manual recovery of a hydraulic pressure cell

Fig. 3.5 Dismantling of the central heater cask

Fig. 3.6 Boreholes and slots in the backfill remaining from sampling at cross section B^{+1}

Fig. 3.7 Cored drilling in the excavated test drift. The drift was widened into the surrounding rock salt to enable the retrieval of the heater casks

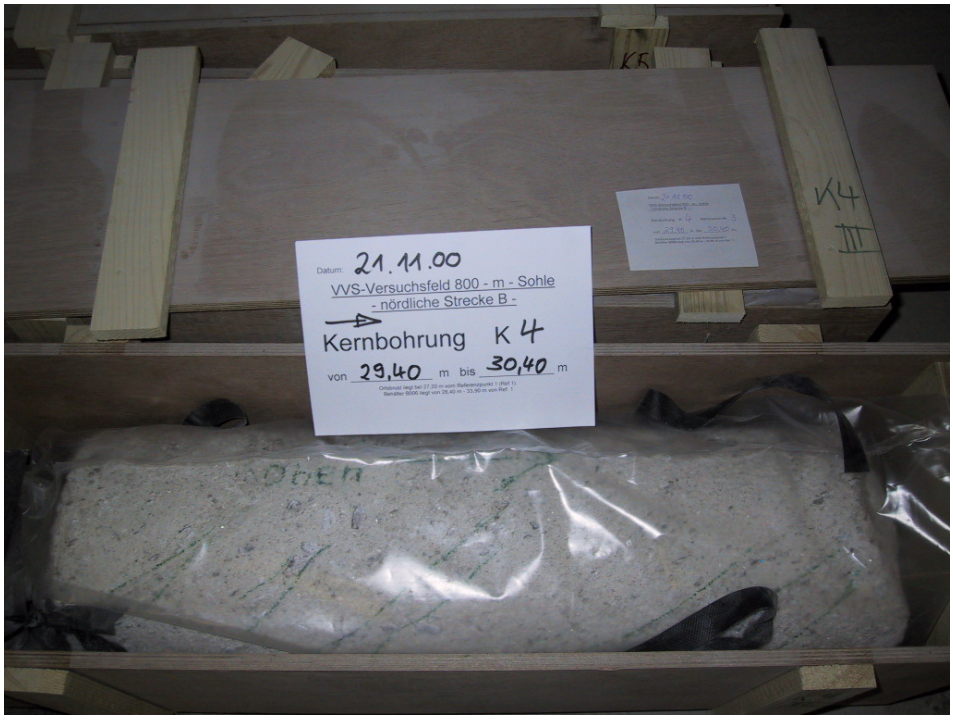

Fig. 3.8 280-mm core ready for shipment to the laboratory

4 Post-Test Investigations of the Backfill

4.1 Hydraulic Properties

For the determination of the post-test porosity and permeability of the compacted backfill, samples were taken during excavation in the heated and the non-heated area from cored borehole K3 and at the cross sections E1, D1, G1, and B^{+1} (Fig. 4.1.1). As the sampling points were located at the same cross sections as the *in-situ* measuring equipment, the laboratory data sets could be compared directly with the *in-situ* measurements.

Borehole K3 was drilled at an early stage of drift excavation when, at about 6 m, the backfill had been removed from the entry. The cored borehole extended 19.3 m from the non-heated backfill into the heated area above the first heater cask (Fig. 4.1.1). The core diameter was 101 mm.

In cross sections E1, D1, and G1, sampling was carried out along vertical profiles at 7 sampling points in each section (Fig. 4.1.2 to 4.1.4). In section B^{+1}, sampling was performed continuously along complete vertical and horizontal profiles, yielding 29 samples in the horizontal direction and 23 samples in the vertical direction (Fig. 4.1.5). Additionally, three backfill samples were taken directly from the cask/backfill-interface where the highest temperatures had been reached during the heating phase.

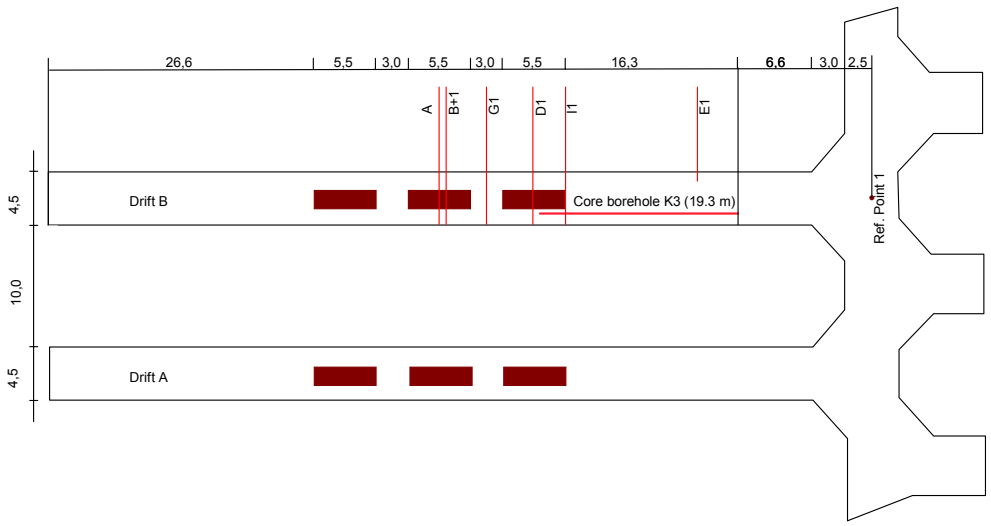

Fig. 4.1.1 Test drifts on the 800-m level with sampling cross sections E1, D1, G1, B^{+1}, and A, and cored borehole K3

For porosity and permeability examinations in the roof area of the test drifts, samples were taken from the rock salt in the heated cross sections D1, G1, and B^{+1} (Fig. 4.1.3 to 4.1.5: Fi). Sampling was performed by drilling up to 0.4-m-long cores with a diameter of 100 mm each.

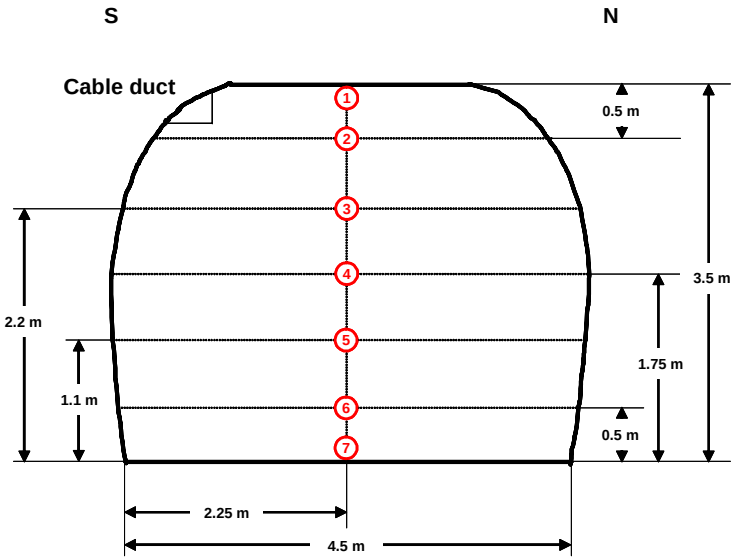

Fig. 4.1.2 Backfill sampling locations (samples 1 to 7) for porosity and permeability measurements in cross section E1

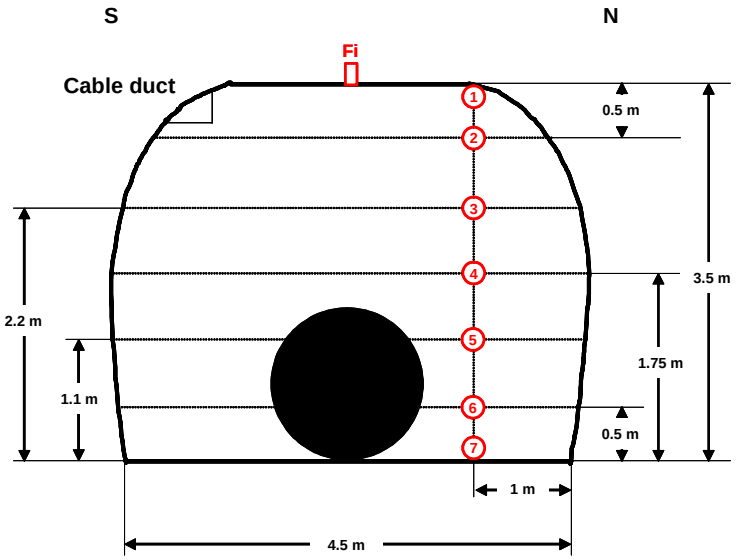

Fig. 4.1.3 Backfill sampling locations (samples 1 to 7) and rock sampling locations in the roof (samples Fi) for porosity and permeability measurements in cross section D1

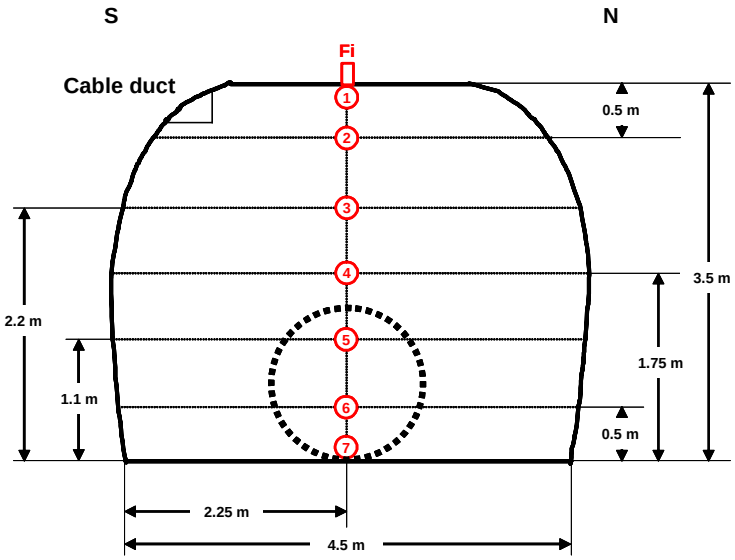

Fig. 4.1.4 Backfill sampling locations (samples 1 to 7) and rock sampling locations in the roof (samples Fi) for porosity and permeability measurements in cross section G1

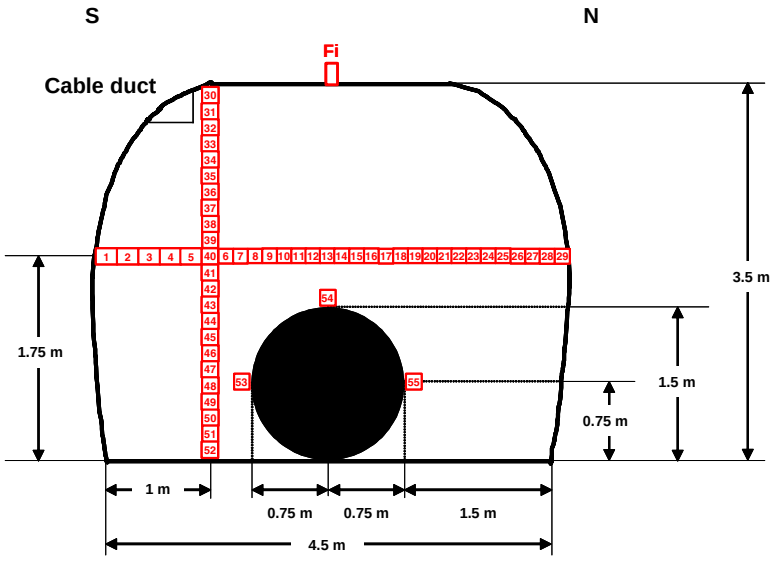

Fig. 4.1.5 Backfill sampling locations (samples 1 to 29 in horizontal direction, samples 30 to 52 in vertical direction, samples 53 to 55 at the cask/ backfill-interface) and rock sampling locations in the roof (samples Fi) for porosity and permeability measurements in cross section B^{+1}

4.1.1 Grain Size Distribution

From radiometric gamma-gamma density measurements which had been performed in the early stage of the experiment /DRO 96/ it was known that the backfill porosity was generally decreasing from the floor to the roof of the test drifts. It is assumed that this trend of increasing density towards the roof was caused by the slinger technique which had been used for drift backfilling. Because the coarser grains had been falling faster than the fine grains, the grade of sorting was high on the bottom of the drifts and decreased towards the top. A high grade of sorting implies a high porosity and a low density. Consequently, the increasing density towards the top had to be caused by the decreasing grade of sorting.

To confirm the grain segregation assumption, the grain size distribution of the undisturbed, non-heated backfill from the slope at the entrance of drift A, which had not been compacted, was analyzed (Fig. 4.1.6).

Fig. 4.1.6 Backfill slope at the entrance of drift A

Figure 4.1.7 shows the grain size distribution of 20 backfill samples taken over the whole slope from the top to the bottom of the drift with a spacing of 0.35 m. It can be seen that the grain size varies over a wide range increasing from d_{50} = 1 mm in the top region to d_{50} = 6 mm in the bottom region (d_{50} is the grain size at 50 % passage).

Using the grain size curves, the uniformity of an unconsolidated material is defined using the coefficient of uniformity U = d_{60}/d_{10} (grain sizes at 60 % and 10 % passage). In the top region, U values greater than 10 are obtained proving the low grade of sorting. Near the bottom of the test drift, however, the sorting is much higher with U values of approximately 5.

Due to the inhomogeneous grain size distribution, variations of the thermomechanical and hydromechanical properties such as porosity and permeability are evident at different locations in the backfill (cf. Section 4.1.2).

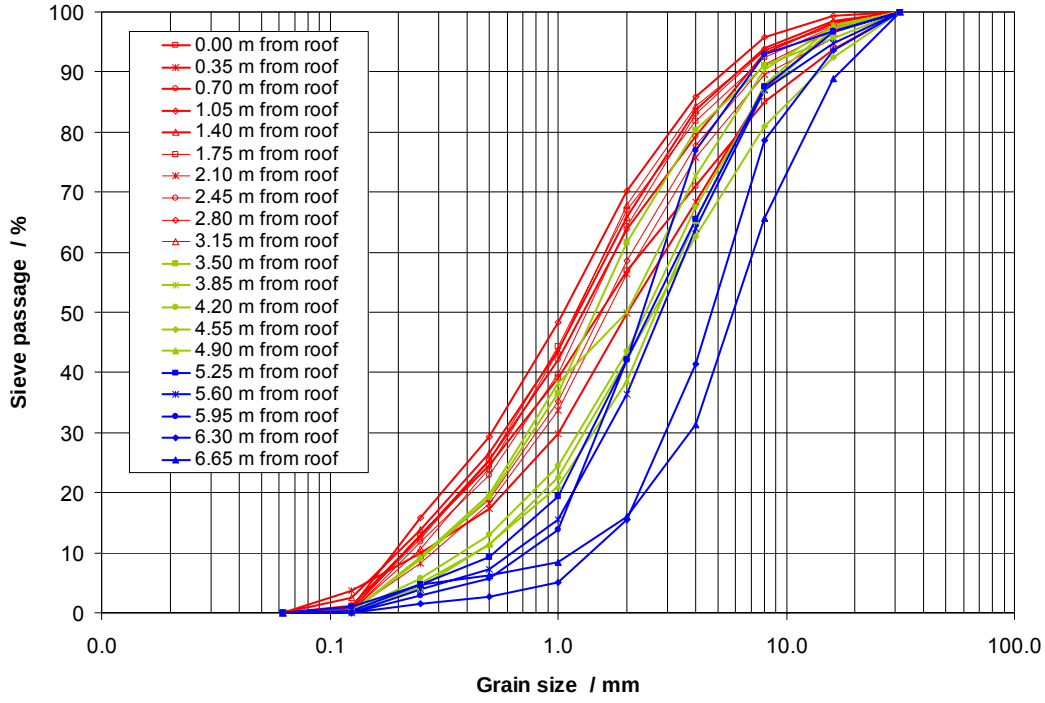

Fig. 4.1.7 Grain size distribution of 20 backfill samples taken from the top to the bottom over the whole backfill slope at the entrance of drift A

4.1.2 Porosity

The absolute porosity Φ was calculated using the grain density ρ_g and the bulk density ρ_b of the sample by

$$\Phi = 1 - \frac{\rho_b}{\rho_g} \qquad (4.1)$$

The bulk density ρ_b was obtained from the bulk volume V_b and the mass m_b of the specimen by

$$\rho_b = \frac{m_b}{V_b} \qquad (4.2)$$

The bulk volume was obtained from the dimensions of the specimen. The grain density was determined by an air comparison pycnometer and resulted in 2.186 g/m^3.

Backfill Samples

The initial porosity of the backfill was about 0.35 in 1990. At the end of the *in-situ* test in March 2000, an average backfill porosity of 0.20 to 0.23 was determined from drift closure measurements in the heated area. These values were derived from a new approach for the determination of the average *in-situ* porosity from the drift closure measurements. With this approach, which takes into account the heater casks, the resulting porosities were lower than the values presented in /DRO 01/.

The porosity data obtained by the post-test laboratory analyses are summarized in Figures 4.1.8 to 4.1.13. In borehole K3, which was drilled from the non-heated backfill into the heated area, a distinct porosity decrease is observed as the first heater cask is approached (Fig. 4.1.8).

In the non-heated cross section E1, the porosity decreases from the floor to the roof (Fig. 4.1.9). This is in agreement with the results of the radiometric gamma-gamma density measurements /DRO 96/. With these measurements, a porosity difference of 0.12 had been observed between the roof and floor in cross section E1 from 1993 to 1995. The actual difference, determined from the post-test analyses, is about 0.11. The

average porosity value of 0.31 is in excellent agreement with the average porosity of 0.31 derived from drift closure measurements at the end of the *in-situ* test /DRO 01/.

A comparable situation is found in cross section G1 (Fig. 4.1.10) between the heater casks 1 and 2, but the average porosity value of 0.26 is lower as this area was significantly influenced by heating. From the *in-situ* measurements, an average porosity value of 0.23 had been obtained in this cross section.

In section D1 at the middle of heater cask 1, the situation is different (Fig. 4.1.11). Here, the porosity increases from the floor to the roof. Assuming that horizontal drift closure is constant over the whole drift cross section, the lower porosity at the heater cask level can be explained by the fact that a smaller backfill volume was affected by drift closure than in the upper part due to the presence of the cask leading to a higher backfill compaction. The average porosity of 0.24 is almost equal to the value of 0.23 determined by the *in-situ* measurements.

In the central heater area, vertical and horizontal profiles were analyzed at cross section B^{+1} for the post-test porosity (Fig. 4.1.12 and 4.1.13). Though significant variations can be seen along the profiles, the porosity decreases generally towards the roof (Fig. 4.1.12) and from the pillar towards the opposite drift wall (Fig. 4.1.13). At the cask/backfill-interface, the measured porosity values of 0.225 and 0.232 at the mid-plane and of 0.135 at the top of the heater cask are in the same range as determined along the profiles. Actually, the porosity is lowest in the centre of the test field with average porosity values of 0.21 (vertical profile) and 0.19 (horizontal profile). These values agree very well with the porosity value of 0.20 which was derived from the new approach for the determination of the average *in-situ* porosity from drift closure measurements.

In summary, the results of the post-test analyses show a decrease of the post-test porosity from the drift entrance towards the centre of the test field. The measured values range between 0.37 and 0.19 thus validating the results of the *in-situ* measurements and the excellent performance of the applied measuring instruments throughout the experimental period of almost ten years.

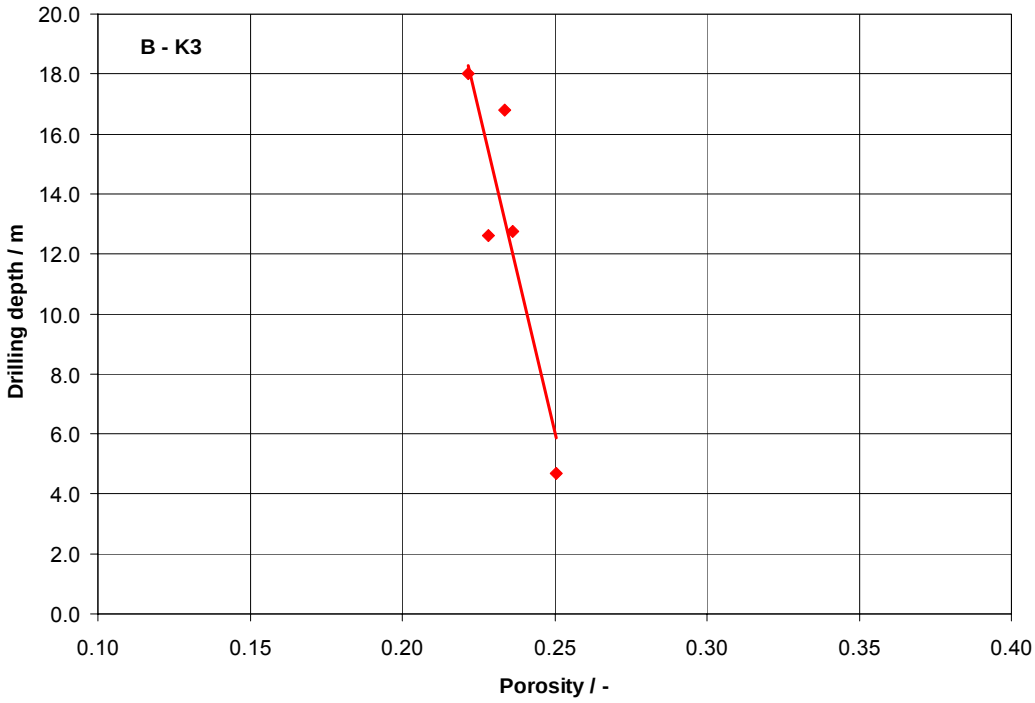

Fig. 4.1.8 Porosity distribution in cored borehole K3

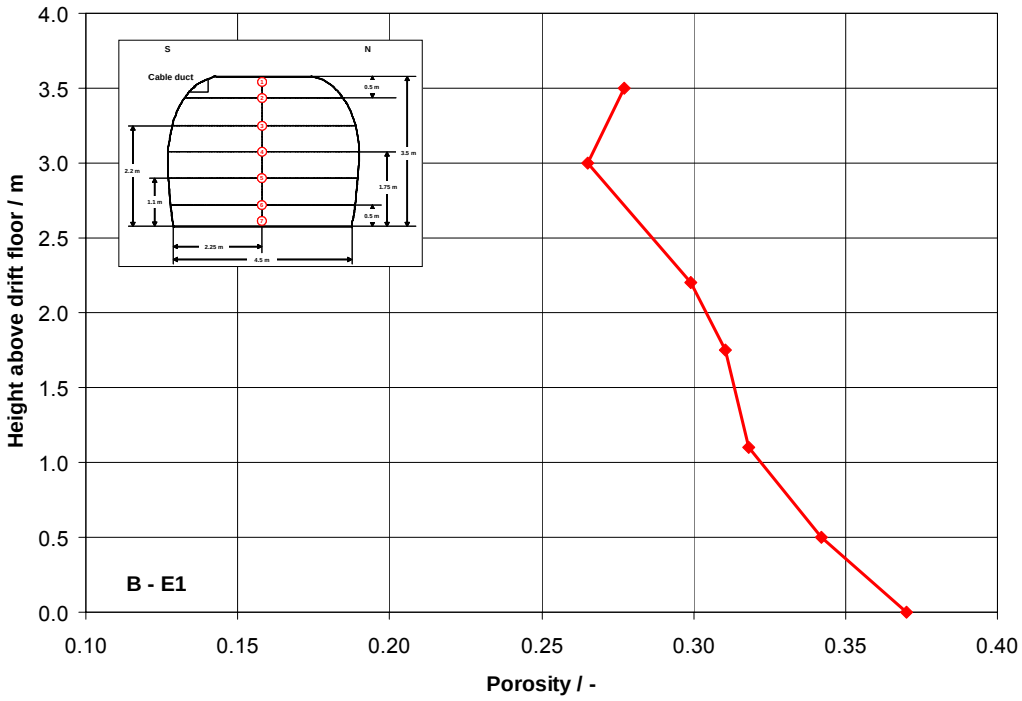

Fig. 4.1.9 Porosity distribution in cross section E1

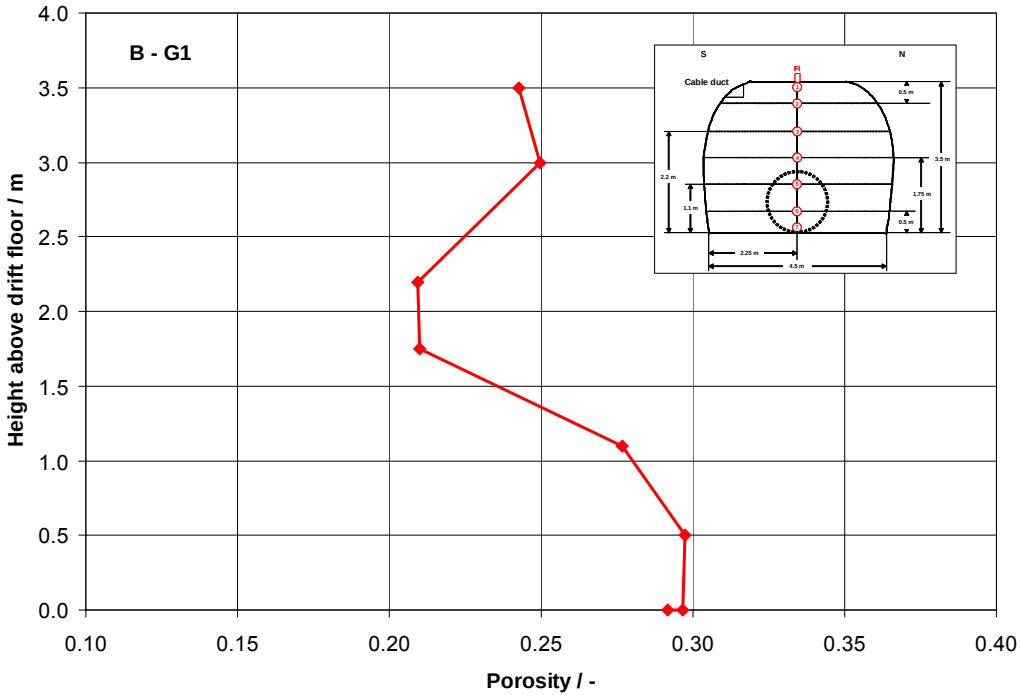

Fig. 4.1.10 Porosity distribution in cross section G1

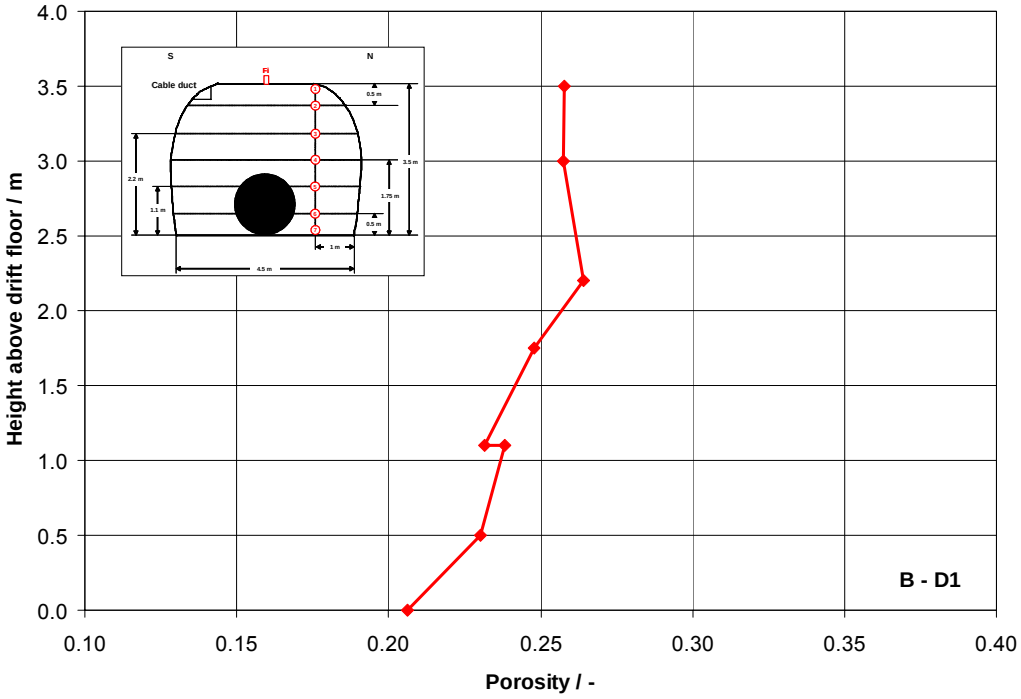

Fig. 4.1.11 Porosity distribution in cross section D1

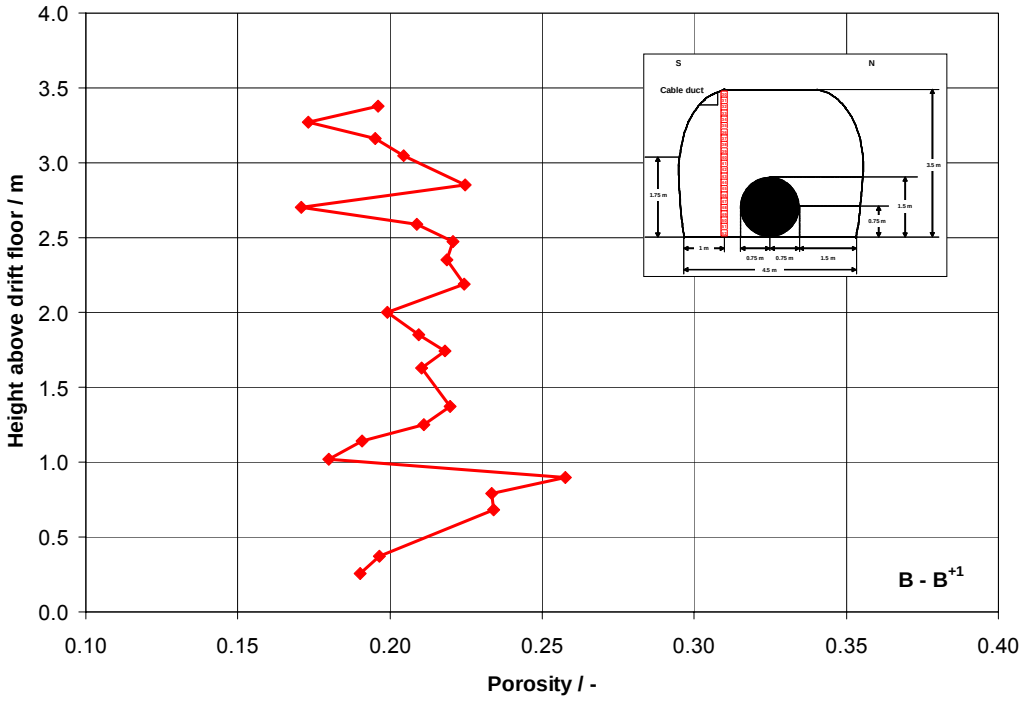

Fig. 4.1.12 Vertical porosity distribution in cross section B^{+1}

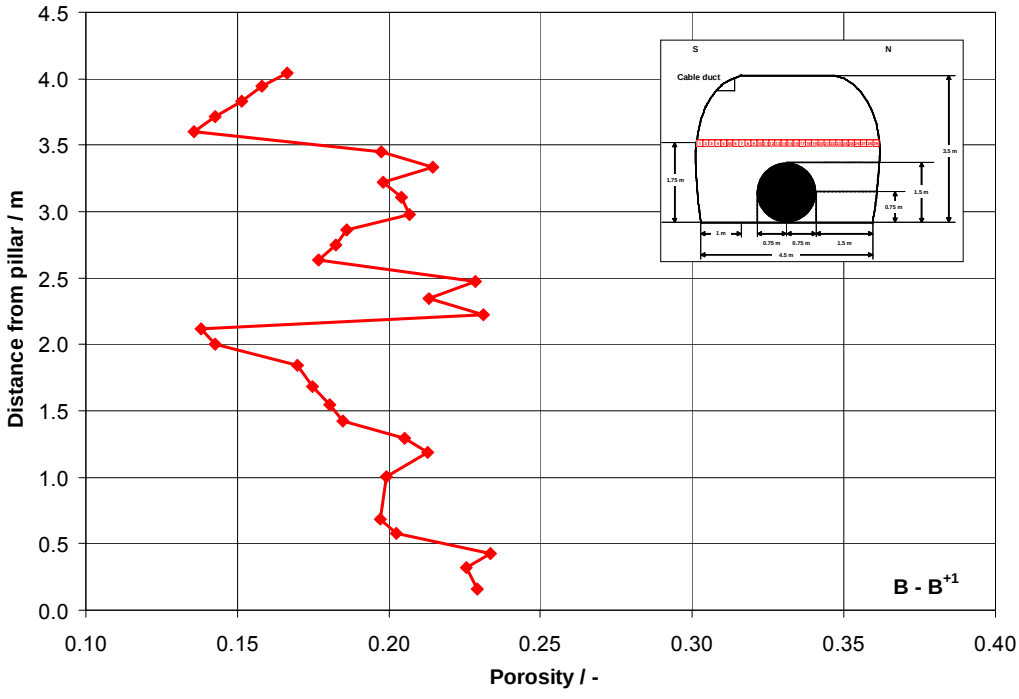

Fig. 4.1.13 Horizontal porosity distribution in cross section B^{+1}

Rock Samples from the Drift Roof

Additionally, porosity determinations were performed on rock salt samples from the roof area of the test drifts in the heated cross sections D1, G1, and B^{+1} (Fig. 4.1.3 to 4.1.5). The porosities of the samples range from 0.001 to 0.025 in cross section D1 (mean value 0.012), 0.006 to 0.053 in cross section G1 (mean value 0.021), and 0.020 to 0.046 in cross section B^{+1} (mean value 0.035).

In all cross sections, the porosities decrease with the depth of the sampling borehole. Regarding to the heaters, no influence of the sampling location on the mean porosity could be detected. However, the porosities increase with the distance from the drift entrance.

4.1.3 Permeability

The gas permeability of the cylindrical specimens was measured with nitrogen as the flow medium and evaluated by Darcy's law

$$k_g = \frac{2 \cdot q \cdot \mu \cdot l \cdot p_0}{A \cdot \left(p_1^2 - p_0^2\right)} \qquad (4.3)$$

with gas permeability k_g, flow rate q, viscosity of the gas μ, sample length l, cross section area of the sample A, injection pressure p_1, and atmospheric pressure p_0.

Backfill Samples

For the permeability measurements, the backfill specimens were sealed with silicone. The gas injection pressure was adjusted to the confining pressure. The permeability data from the post-test laboratory analyses are summarized in Figures 4.1.14 to 4.1.17.

In cored borehole K3, permeability remains rather constant at about 7E-12 m² along the borehole length from the non-heated backfill to the heated area (Fig. 4.1.14). Though a little low, this permeability value is in good agreement with the permeabilities observed at the other sampling cross sections at the same drift height of 2.89 m.

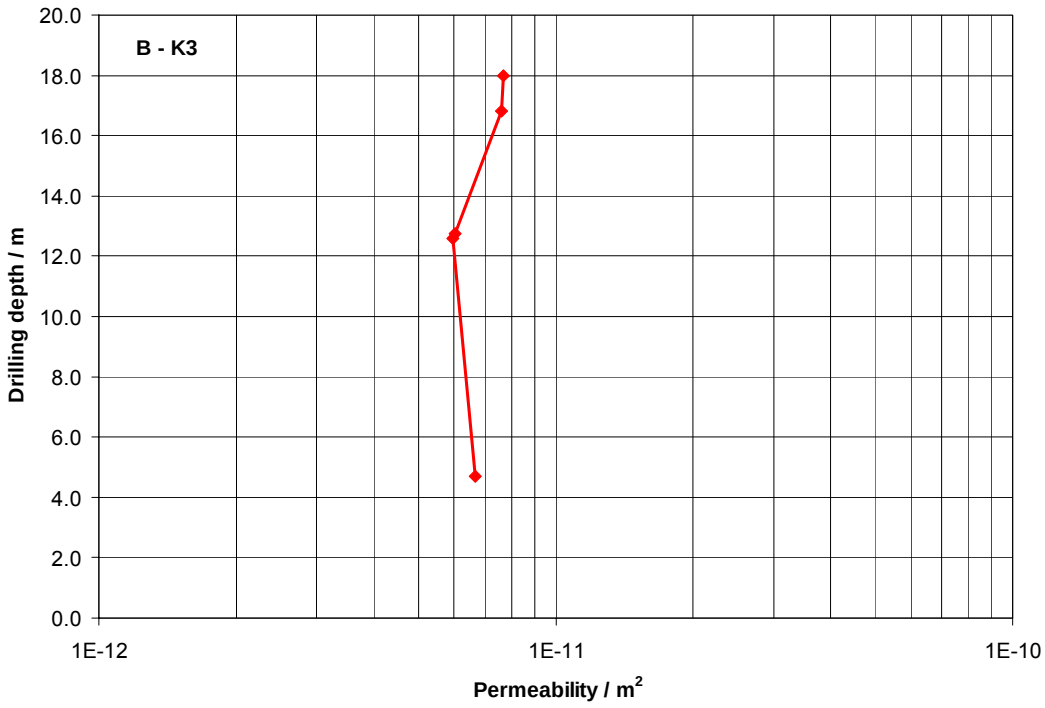

Fig. 4.1.14 Permeability distribution in cored borehole K3

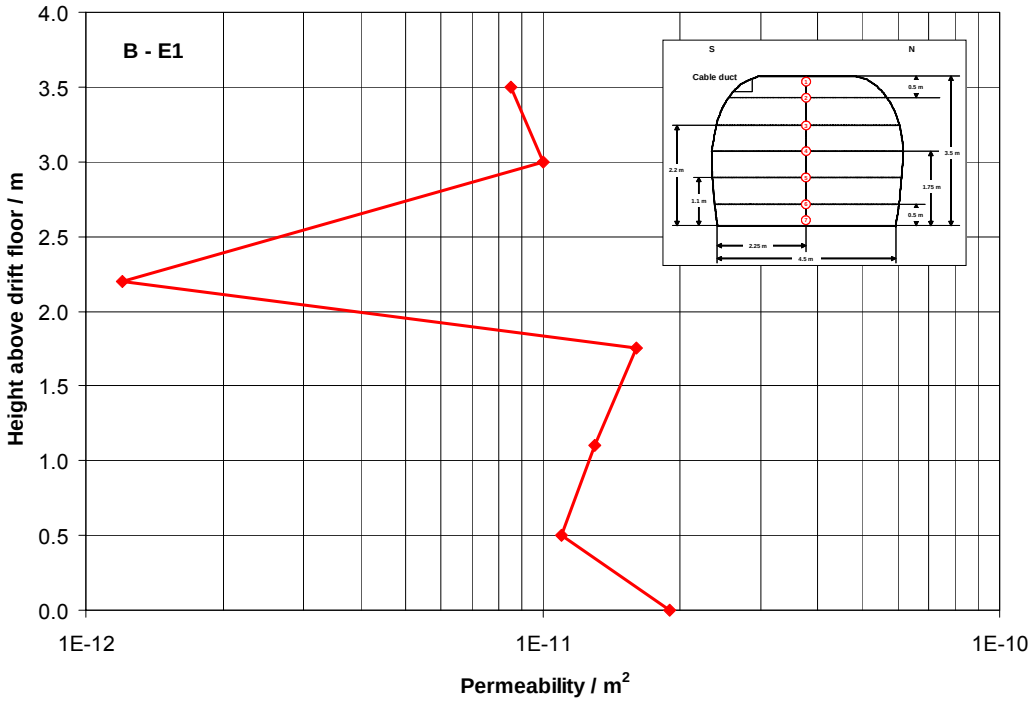

Fig. 4.1.15 Permeability distribution in cross section E1

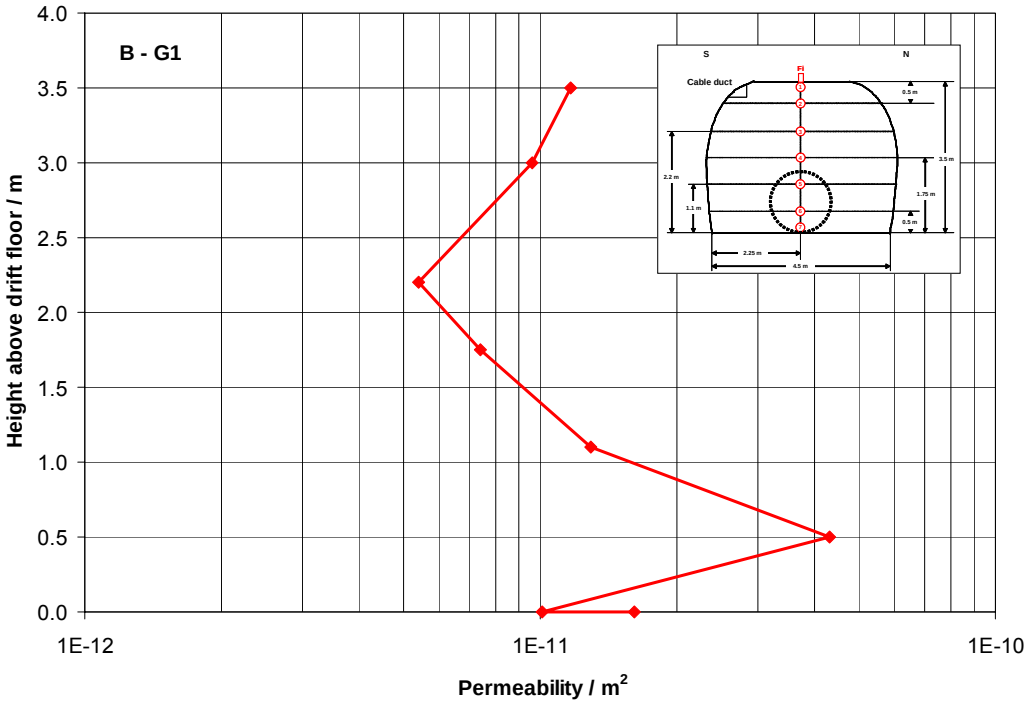

Fig. 4.1.16 Permeability distribution in cross section G1

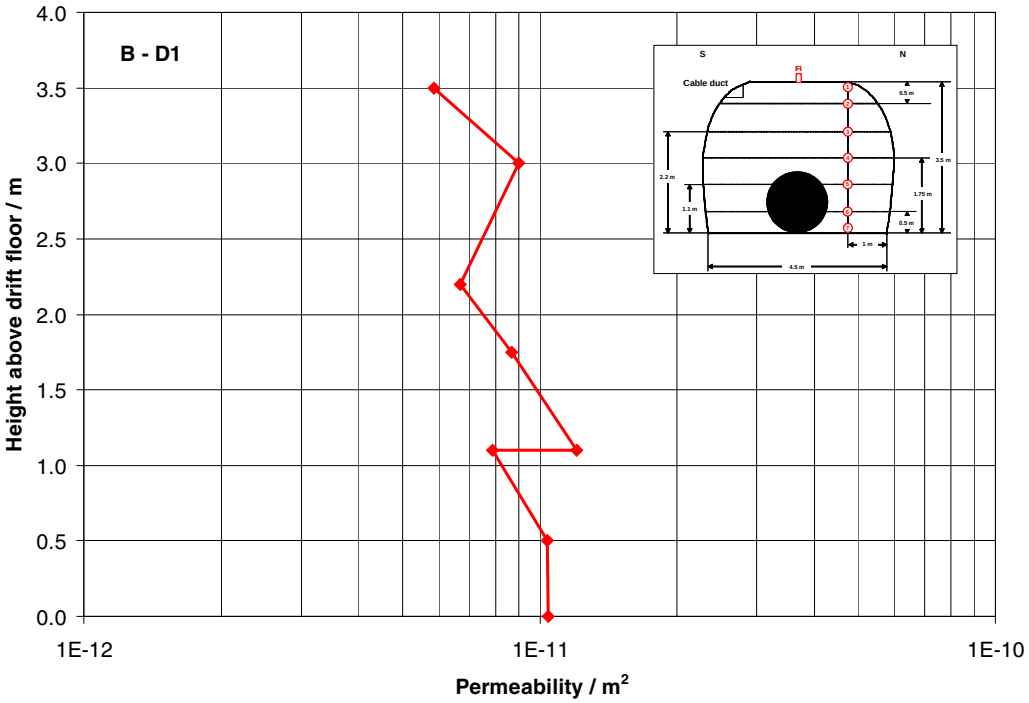

Fig. 4.1.17 Permeability distribution in cross section D1

The permeability values determined in the cross sections E1, G1, and D1 range about 1E-11 m² (Fig. 4.1.15 to 4.1.17). This permeability is equal to the value derived *in situ* during the heating period. Hence, the applied method for permeability determination, described in /DRO 01/, was confirmed.

Backfill Samples from Cored Boreholes K4, K5, and K6

During drift excavation, three large boreholes K4, K5, and K6 were cored to obtain large samples for the determination of the mechanical parameters of the backfill (cf. Section 4.2). These cored boreholes were started from cross section I1 at the front of the first heater cask with a length of 3 m each (Fig. 4.1.18). The borehole diameter was 280 mm. Coupled to the mechanical tests, additional permeability measurements were performed at different porosities that were reached by step-by-step increases of the hydrostatic load. The gas injection pressure was adjusted in the range of 0.1 to 1.0 bar.

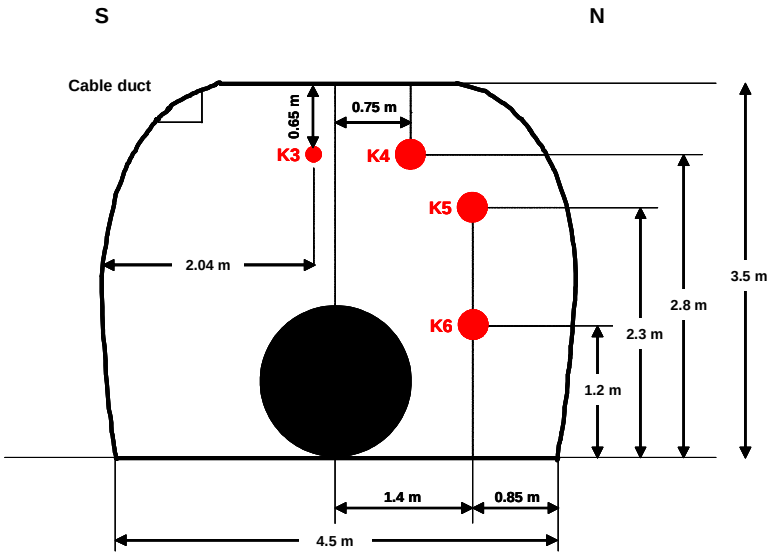

Fig. 4.1.18 Locations of large cored boreholes K4, K5, and K6 in cross section I1. The trace of cored borehole K3, which had been drilled at an early stage of drift excavation, is shown, too.

The results of the permeability tests are given as a function of porosity in the double-logarithmic plot shown in Figure 4.1.19. The permeability decreases from 1.5E-12 m² at a porosity value of 0.26 to 2E-13 m² at a porosity of 0.07. Based on the results from the tested samples, the relation between permeability and porosity was determined to be $k = 1E\text{-}11 \cdot \Phi^{1.8}$.

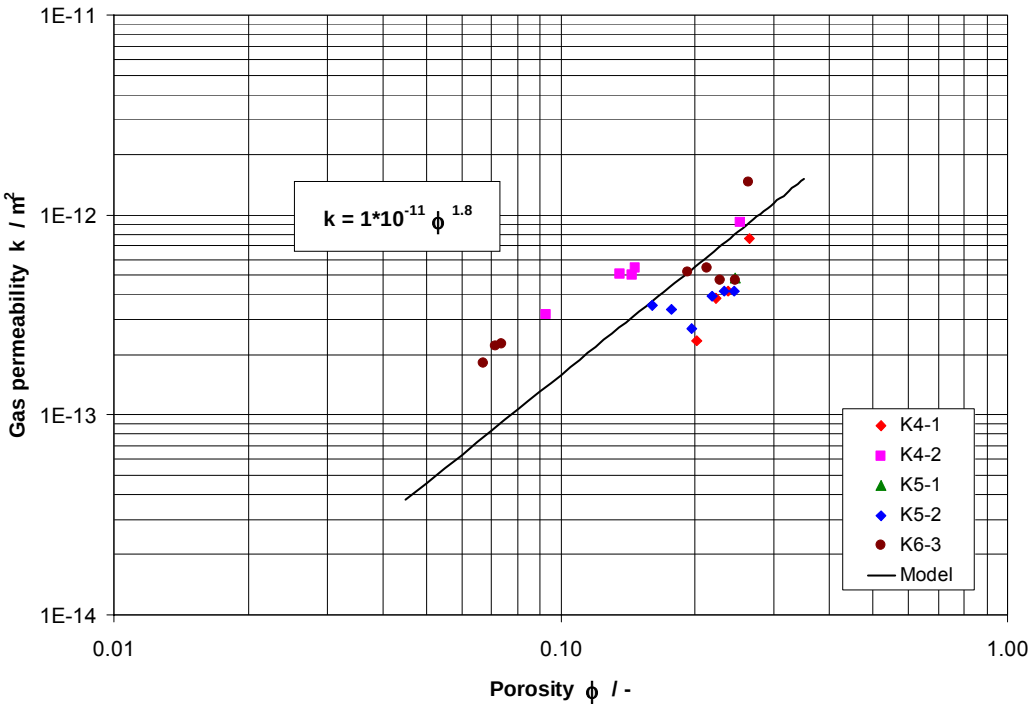

Fig. 4.1.19 Gas permeability of the *in-situ* compacted salt backfill as a function of porosity

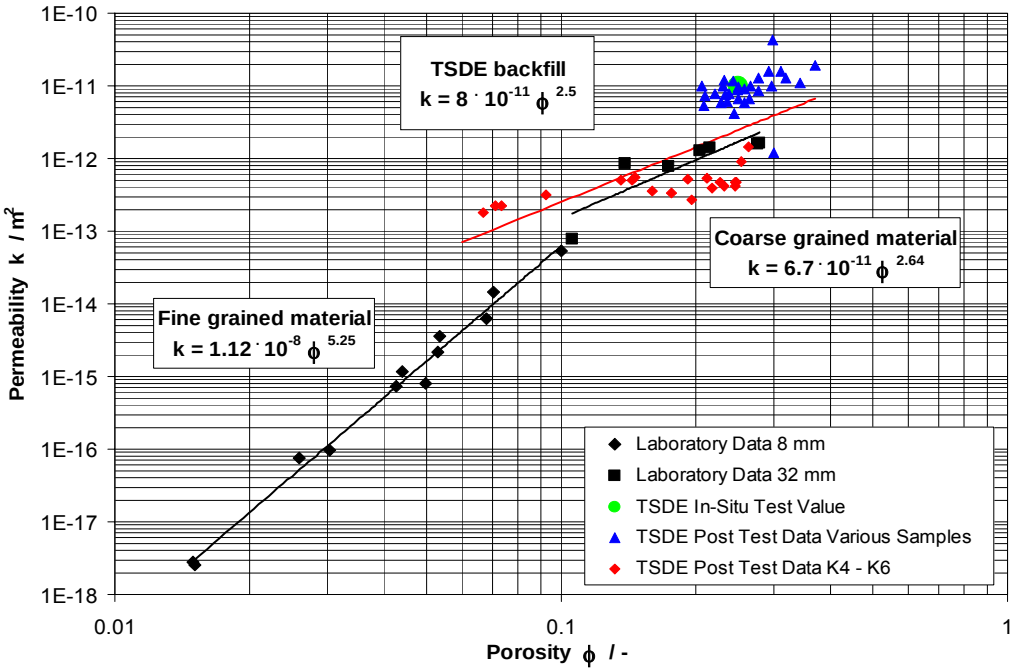

Fig. 4.1.20 Comparison of the permeability of the TSDE backfill samples with data from other investigations performed on Asse backfill

In Figure 4.1.20, these results are compared with previous tests on backfill samples and *in-situ* data /ROT 01/. It can be seen that the permeability values obtained on the large core samples K4 to K6 are 5 to 10 times lower than those determined in previous tests and *in situ* at the same porosity values. However, these permeability values are comparable with the results obtained on coarse grained crushed salt with grain sizes less than 32 mm. By fitting all data of the TSDE backfill, a permeability – porosity relation of $k = 8E\text{-}11 \cdot \Phi^{2.5}$ was determined.

Rock Samples from the Drift Roof

From the heated cross sections D1, G1, and B^{+1}, rock salt samples from the drift roof were investigated in the laboratory (Fig. 4.1.3 to 4.1.5). The permeability was measured in dependence of a confining pressure between 1 MPa and 6 MPa. In Table 4.1.1, the porosity and permeability values are summarized.

Generally, the permeability investigations showed decreasing values with increasing confining pressure. The most significant influence of the confining pressure was observed at cross section D1. Near the borehole collar, the permeability of sample D1-Fi3 decreased by about three orders of magnitude from 1.3E-18 m^2 to 5.4E-21 m^2 with increasing confining pressure (Tab. 4.1.1). At the other samples, the permeability decreased by a factor of about 2 to 5.6 with increasing confining pressure.

Depending on the borehole depth, the permeabilities ranged between 1.7E-14 m^2 to 5.4E-21 m^2 at different confining pressures. The lowest permeabilities were measured in cross section D1. In section G1, the permeabilities were insignificantly higher than in section B^{+1}. This result is corresponding to the porosity distribution.

Corresponding to the backfill pressure of approximately 4 MPa, which had been measured *in situ* at the end of the heating period /DRO 01/, the permeabilities were examined especially at 4 MPa. Apart from sample D1-Fi3, the permeabilities were relatively high at this confining pressure ranging between 8.8E-15 m^2 to 1.7E-17 m^2. This can be explained by the influence of drift opening, drilling and additionally, by sample preparation. But it has also to be taken into account that the support of the backfill was possibly not high enough for healing the excavation disturbed zone.

Tab. 4.1.1 Porosity and permeability measurements at rock samples from the drift roof

Sample No.	Depth	Porosity	Permeability		
			at 1 MPa	at 4 MPa	at 6 MPa
	cm	-	m²	m²	m²
D1-Fi1	2 - 13	0.010	n.d.	n.d.	n.d.
D1-Fi3	3 - 15	0.025	1.3E-18	4.3E-20	5.4E-21
D1-Fi4	16 - 25	< 0.001	1.4E-16	1.1E-16	8.8E-17
D1-Fi2	17 - 34.5	0.001	n.d.	n.d.	n.d.
D1-Fi5	27 - 37	< 0.001	2.6E-17	1.7E-17	1.4E-17
G1-Fi4	2 - 9	0.053	1.7E-14*	8.8E-15	7.7E-15
G1-Fi1	2 - 13	0.025	n.d.	n.d.	n.d.
G1-Fi5	12 - 24	0.014	7E-15*	3.8E-15	3.5E-15
G1-Fi2	16 - 28	0.010	n.d.	n.d.	n.d.
G1-Fi6	26 - 26	0.006	2E-15*	5.9E-16	4.3E-16
G1-Fi3	30 - 40	0.014	n.d.	n.d.	n.d.
B+1-Fi1	2 - 9	0.041	n.d.	n.d.	n.d.
B+1-Fi3	3 - 20	0.046	7.3E-15	4.6 E-15	3.7E-15
B+1-Fi4	24 - 36	0.020	2.4E-16	1.4E-16	8.8E-17
B+1-Fi2	25 - 36	0.032	n.d.	n.d.	n.d.

n.d. = not determined * at 1.15 MPa

4.2 Mechanical Properties

To examine the geomechanical properties of crushed salt backfill from the heated area which had been thermomechanically compacted, a series of large-scale laboratory experiments was performed. The test programme included the investigation of the stress – strain behaviour as well as strength and permeability under hydrostatic and deviatoric loads.

K4-1
H/D=561/280 mm
ϕ = 0.265

K4-2
H/D=712/280 mm
ϕ = 0.255

K5-4
H/D=679/280 mm
ϕ = 0.260

Before testing

K4-1
σ_a–σ_r = (18.7 – 4) MPa
shear damage

K5-1
σ_a–σ_r = (20 – 4) MPa
shear damage

K6-3
σ_a–σ_r = (58.4 – 10) MPa
no shear damage

After testing

Fig. 4.2.1 Backfill samples from the large cored boreholes K4, K5, and K6 in cross section I1 before and after testing

From the cored boreholes K4, K5, and K6 (Fig. 4.1.18, cf. Section 4.1.3), six samples were taken which had a diameter of 280 mm and a height between 510 to 710 mm (H/D = 1.82 to 2.53). The initial sample porosities of 0.255 to 0.265 agreed well with the values determined by the *in-situ* measurements. From the samples, segregation of the grains can obviously be recognized (Fig. 4.2.1).

The laboratory tests on the compacted samples were conducted using a large servo-controlled triaxial apparatus MTS (max. axial load 4600 KN, max. confining pressure 50 MPa), which allows a maximum sample size of 280 mm diameter and 700 mm height. The samples were inserted in a rubber jacket. On the bottom and top surfaces of the samples, some salt powder was put to gain parallel plane contacts to the pistons. The tests were conducted at ambient temperatures of 24 ± 1^{o}C.

Axial deformation of the samples was measured by using a LVDT-transducer (accuracy with a max. error of ± 1.0 %) installed inside of the lower piston, whereas the radial deformation was measured by using a diameter-measuring device (max. error of ± 0.5 %) installed at the mid-height of the sample. Additionally, the volume change of the samples was determined from the confining oil which was expelled from the cell to a pressure intensifier by using a LVDT-transducer (max. error of ± 1.0 %). The cell pressure was controlled by a pressure gauge (max. error of ± 1.0 %).

In order not to hinder the expected high radial sample deformations in the deviatoric loading tests, the diameter-measuring device normally placed on the sample surface in the annulus between the sample and the inner wall of the test apparatus was not used. Therefore, the radial strains of all samples were calculated from the volume changes. Axial stress was evaluated by considering changes of the sample cross section during the test.

In addition to the mechanical measurements, the gas permeability of the samples as a function of compaction was determined by measuring the steady-state flow rate of nitrogen gas under constant load conditions (cf. Section 4.1.3).

The tests were evaluated according to the following definitions:

- radial stress: σ_r oil pressure in cell
- axial stress: $\sigma_a = \frac{F - \sigma_r (A_0 - A)}{A}$ F = axial force,
  A_0 = initial sample cross section,
  A = current sample cross section
- mean stress: $\sigma_m = (\sigma_a + 2\sigma_r)/3$
- differential stress: $\Delta\sigma = (\sigma_a - \sigma_r)$

- axial strain: $\varepsilon_a = (H_0 - H)/H_0$ — H = height of the sample, H_o = initial height
- radial strain: $\varepsilon_r = (D_0 - D)/D_0$ — D = diameter of the sample, D_o = initial diameter
- volumetric strain: $\varepsilon_v = (V_0 - V)/V_0$ — V = volume of the sample, V_o = initial volume
- bulk modulus: $K = \Delta\sigma_m / \Delta\varepsilon_v$ — determined in the unloading path
- Young's modulus: $E = \Delta(\sigma_a - \sigma_r)/\Delta\varepsilon_a$ — determined in the unloading path
- Poisson's ratio: $\nu = -\varepsilon_r / \varepsilon_a$ — determined in the unloading path
- porosity ϕ (*n*): $\phi = 1 - (\rho / \rho_s)$ — ρ = bulk density, ρ_s = grain density (2.19 g/cm^3)
- gas permeability: $k = 2\mu \frac{p_a \cdot Q}{(p_{in}^2 - p_a^2)} \cdot \frac{H}{A}$ — after Darcy's law; μ = 1.74E-5 Pa·s of the dynamic viscosity of gas, p_a = atmospheric pressure, p_{in} = injection pressure, Q = flow rate of gas, H/A= sample height/cross section.

4.2.1 Hydrostatic Tests

Two hydrostatic compression tests were performed to examine the compaction behaviour and associated parameters of the thermomechanically compacted crushed salt. The samples were compacted under hydrostatic pressure $\sigma_a = \sigma_r$ using a loading rate of 1 MPa/min. A summary of the characteristic sample properties and the results of the hydrostatic tests is given in Table 4.2.1.

Tab. 4.2.1 Summary of large-scale hydrostatic tests on compacted crushed salt backfill

Sample No.	Sampling position	Initial property of sample				Results of hydrostatic tests			
		D_o	H_o	ρ_o	ϕ_o	ϕ_E	σ_r	σ_a	σ_m
		mm	mm	g/cm^3	-	-	MPa	MPa	MPa
K4-2	K4/29.4–30.4m	280	712	1.630	0.255	0.0885	25.0	25.1	25.0
K5-2	K5/28.0–29.0m	280	579	1.643	0.260	0.160	11.0	11.1	11.1

Figures 4.2.2 and 4.2.3 illustrate the stress – strain curves ($\sigma_a = \sigma_r$ - ε_a / - ε_r / - ε_v) of the tests K4-2 and K5-2. Figure 4.2.4 gives the porosity as a function of mean stress (ϕ - σ_m), also including the data of the hydrostatic compaction part of the test K6-3.

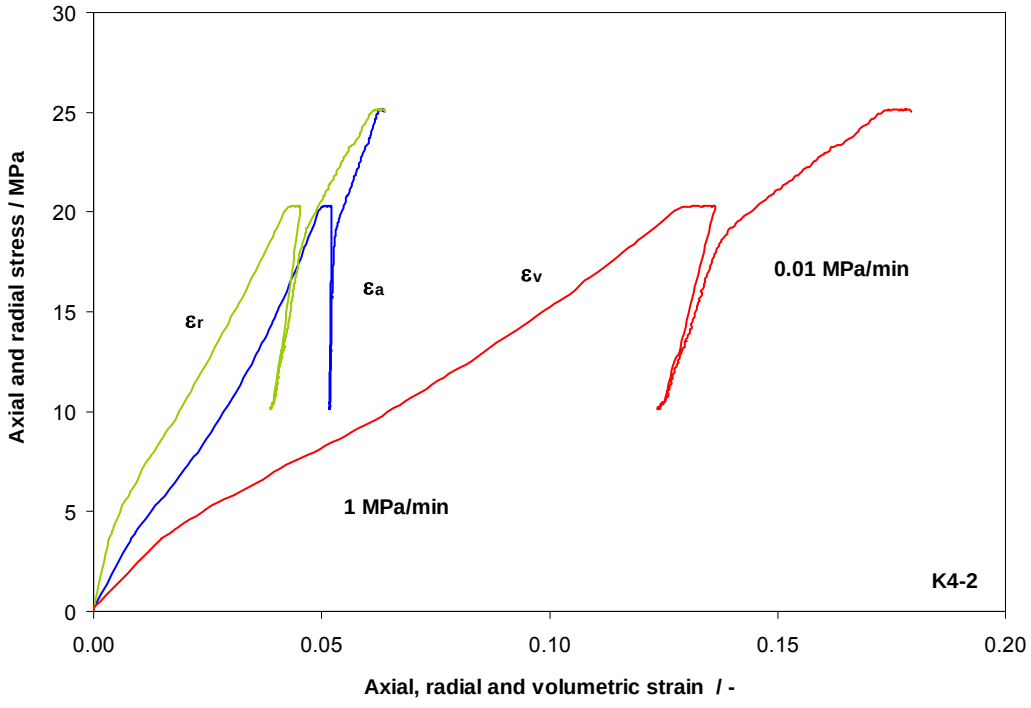

Fig. 4.2.2 Hydrostatic compaction behaviour of backfill sample K4-2

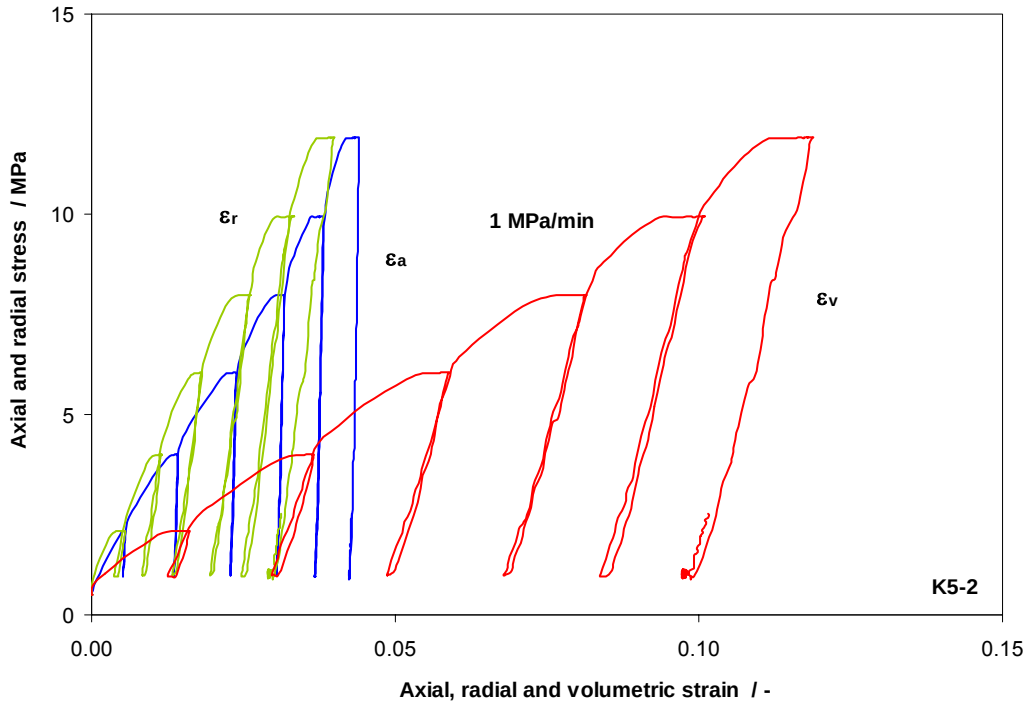

Fig. 4.2.3 Hydrostatic compaction behaviour of backfill sample K5-2

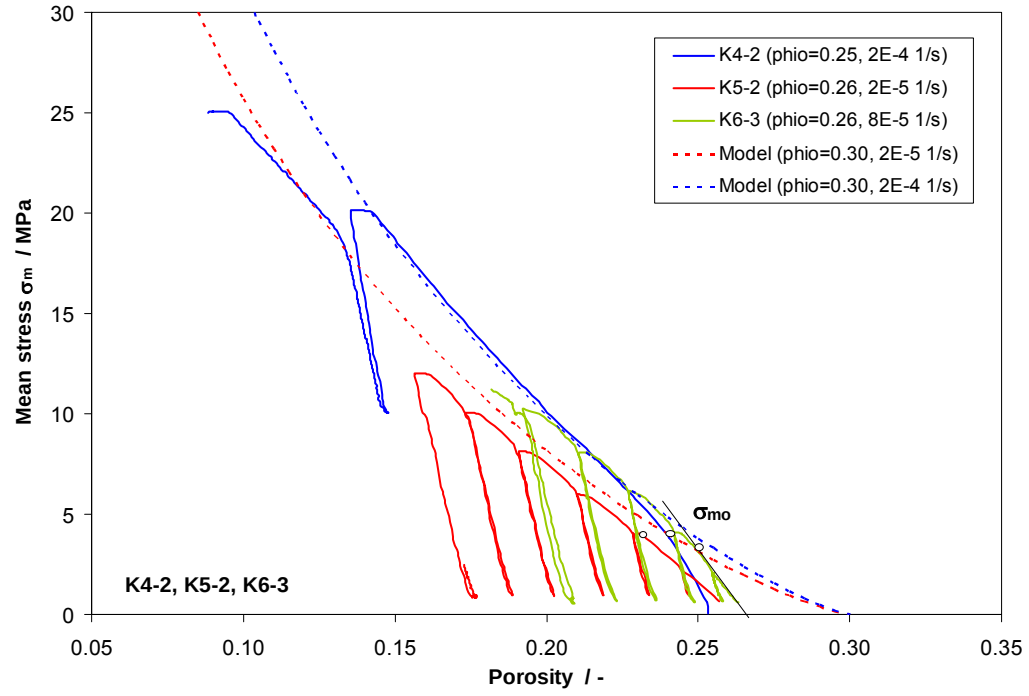

Fig. 4.2.4 Porosity as a function of mean stress during hydrostatic compaction of backfill samples K4-2, K5-2, and K6-3

In the following, the results of the hydrostatic compression tests are summarized.

- Slower loading induces more compressive deformation, comparing the two parts of the compaction curve of test K4-2 with loading rates of 1 MPa/min and 0.01 MPa/min (Fig. 4.2.2).
- Under laboratory conditions (ambient temperature and high compaction rates), an *in-situ* backfill pressure of about 4.0 to 4.5 MPa was determined as the stress at the first point where the compaction curve departed from the linear elastic portion of the curve (Fig. 4.2.4). The pressure determined using this method was higher than the backfill pressure of 2 to 4 MPa that had been observed *in situ* at higher temperatures (90 to 170 °C) and very low compaction rates (1E-11 to 1E-10 s^{-1}).
- Beyond this backfill pressure, non-linear plastic compaction appears following the normal compaction of initially loose backfill (Fig. 4.2.4).
- Bulk moduli were measured on the samples K5-2 and K6-3 in the unloading paths at different porosities (Fig. 4.2.5). The bulk modulus increases rapidly from about 300 MPa to 600 MPa in the porosity range of ϕ = 0.26 – 0.22 and then remains almost constant down to a porosity of ϕ = 0.16.

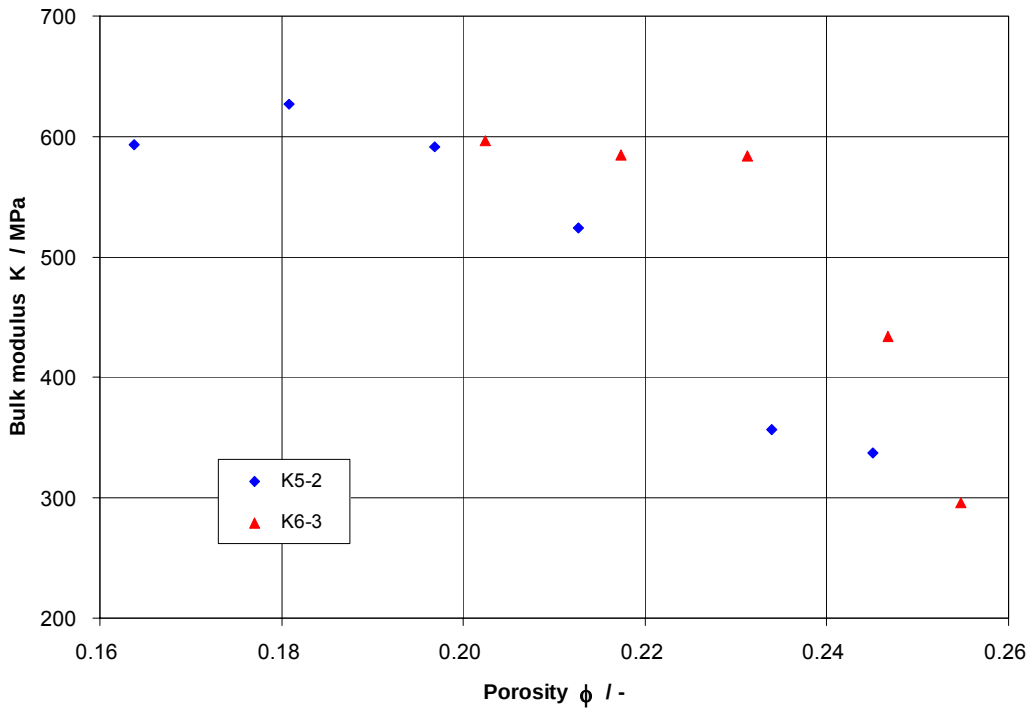

Fig. 4.2.5 Bulk moduli of backfill samples K5-2 and K6-3

Zhang's model /BEC 99/, /ZHA 01/ was chosen to describe the backfill compaction:

$$\dot{\varepsilon}_v = A \exp\left(\frac{-Q}{RT}\right)\left(\frac{\sigma}{\sigma_o}\right)^n \left[\ln\left(\frac{\phi_o(1-\phi)}{\phi(1-\phi_o)}\right)\right]^{-m} \qquad (4.4)$$

The associated compaction parameters were determined by fitting the test data: A = 6E8 s^{-1}, Q = 156 kJ/mole, n = 12, m = 15. The Q-value was chosen directly from the oedometric tests on crushed salt with grain sizes less than 32 mm /ZHA 01/. The triaxial compression tests in the laboratory benchmark programme /ZHA 01/ indicated that the values of the parameters n, m and Q are not very dependent on the test type like oedometric or hydrostatic loading test. In the model calculation, an initial porosity of 0.30 and compaction rates of 2E-5 and 2E-4 s^{-1} were used. The compaction rates correspond to the average values of the volumetric strain rates applied by the stress rate of 1 MPa/min in the tests. Figure 4.2.4 shows a good agreement between model calculation and laboratory experiments. Using the parameters and average conditions from the test field (temperature = 100 °C, compaction rates = 2E-3 a^{-1} and 5E-3 a^{-1}, initial porosity = 0.35), the average compaction behaviour of the backfill was predicted. The calculation results coincide quite well with the *in-situ* measurements (Fig. 4.2.6).

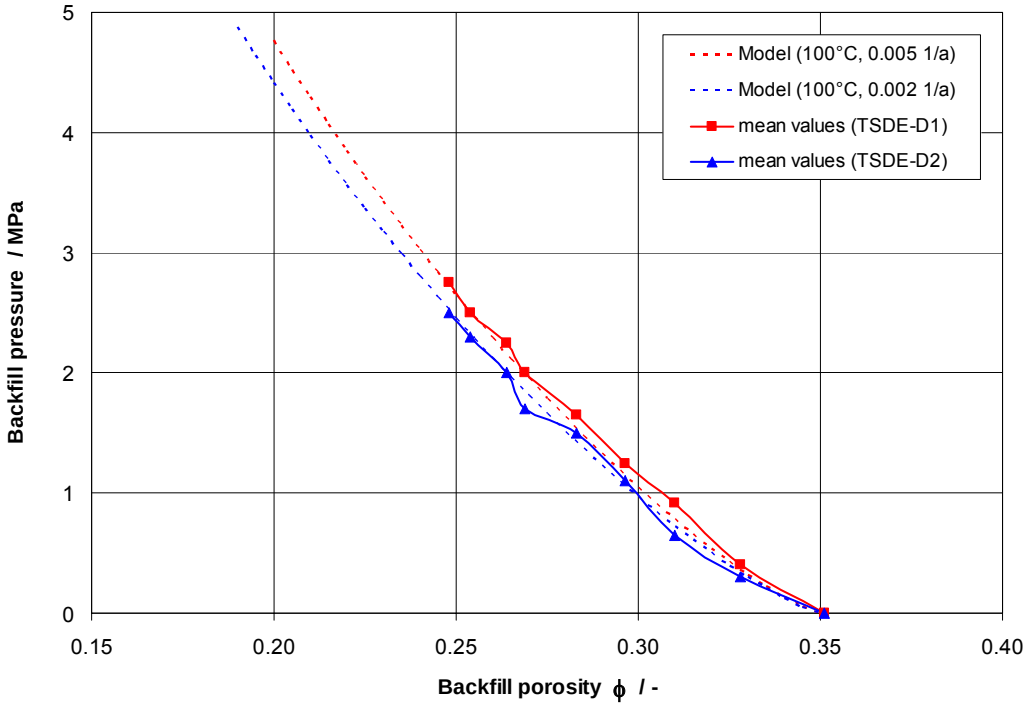

Fig. 4.2.6 Comparison between measured and calculated backfill pressure as a function of average porosity

4.2.2 Deviatoric Tests

The purpose of the deviatoric compression tests was to obtain stress – strain behaviour and strength of the backfill under deviatoric loads. At each confining pressure, a failure loading path was applied on the samples to achieve more information from a single sample using an axial deformation rate of 1 mm/min. After reaching a desired confining pressure, the axial force was increased up to axial peak strength. In the post-failure region beyond that peak, the next elevated confining pressure was applied. At this point, the next deviatoric loading started. This process was repeated until the sample surface reached the inner wall of the test apparatus.

From this test type, the failure envelope and post-failure behaviour of the material can be obtained with a single sample. The characteristic sample properties and the results of the deviatoric tests are summarized in Table 4.2.2.

Tab. 4.2.2 Summary of large-scale deviatoric tests on compacted crushed salt backfill

Sample No.	Sampling position	Initial property of sample				Results of deviatoric tests			
		D_o	H_o	ρ_o	ϕ_o	σ_r	$\sigma_{a\text{-}max}$	ε_r	ε_a
		mm	mm	g/cm^3	-	MPa	MPa	%	%
K4-1	K4/27.2–28.4m	280	561	1.609	0.256	1.1	7.0	-2.5	8.2
						2.0	10.6	-3.7	11.9
						3.0	16.2	-10.2	24.4
						4.0	18.7	-13.4	29.9
K5-1	K5/27.2–28.0m	280	509	1.611	0.264	3.0	15.4	-1.3	16.0
						4.0	19.9	-10.6	31.9
K5-4	K5/29.0–30.0m	280	679	1.557	0.289	3.0	17.4	-4.6	16.7
						4.0	20.3	-13.2	29.6
K6-3	K6/31.5–32.5m	280	585	1.525	0.260	10.1	58.4	-11.4	41.1

Figures 4.2.7 to 4.2.10 show the results of the four triaxial tests with axial stress – axial strain ($\sigma_a - \varepsilon_a$), axial stress – radial strain ($\sigma_a - \varepsilon_r$), radial stress – axial strain ($\sigma_r - \varepsilon_a$), and volumetric strain – axial strain ($\varepsilon_v - \varepsilon_a$). From the plots, the yield stress σ_y (elastic limit), the dilatancy point σ_d, the peak strength σ_{max}, and elastic parameters for each constant confining pressure can be taken (Fig. 4.2.7: Test K4-1). The following phenomena can be observed:

- The stress – strain curves indicate very large deformation without sharp rupture even after the peak strength is reached. The major component of the deformation is plastic, and the elastic parts are negligible.
- Each increase of confining pressure (after reaching peak strength at the lower continuing pressure) causes further compaction and increases both the stiffness and strength of the samples.
- Increases in the volume (or dilatancy) of the compacted backfill are not significant under the imposed test conditions. The deviatoric stresses initiating dilatancy at different confining pressures are nearly the same as the maximum strengths, i.e., $\sigma_d \approx \sigma_{\max}$.
- Based on the strength values obtained from the multi-failure points, the parameters of the Mohr-Coulomb strength criterion were determined as cohesion c = 0.3 MPa and internal friction angle $\Phi = 43^{\circ}$ (Fig. 4.2.11).
- The yield stress points are located beneath the strength envelope (Fig. 4.2.11). Because of lack of special test data, the yield locus in the stress plane could not be determined yet.
- The elastic parameters, Young's modulus and Poisson's ratio, are obtained from the unloading data (Tab. 4.2.3).

Tab. 4.2.3 Elastic parameters of the backfill determined from the unloading data of the deviatoric tests

Sample No.	Porosity ϕ	Young's modulus E	Poisson's ratio ν	Bulk modulus K
	-	MPa	-	MPa
K4-1	0.224	5,400	0.335	5,455
K6-3	0.010	14,500	0.278	10,886

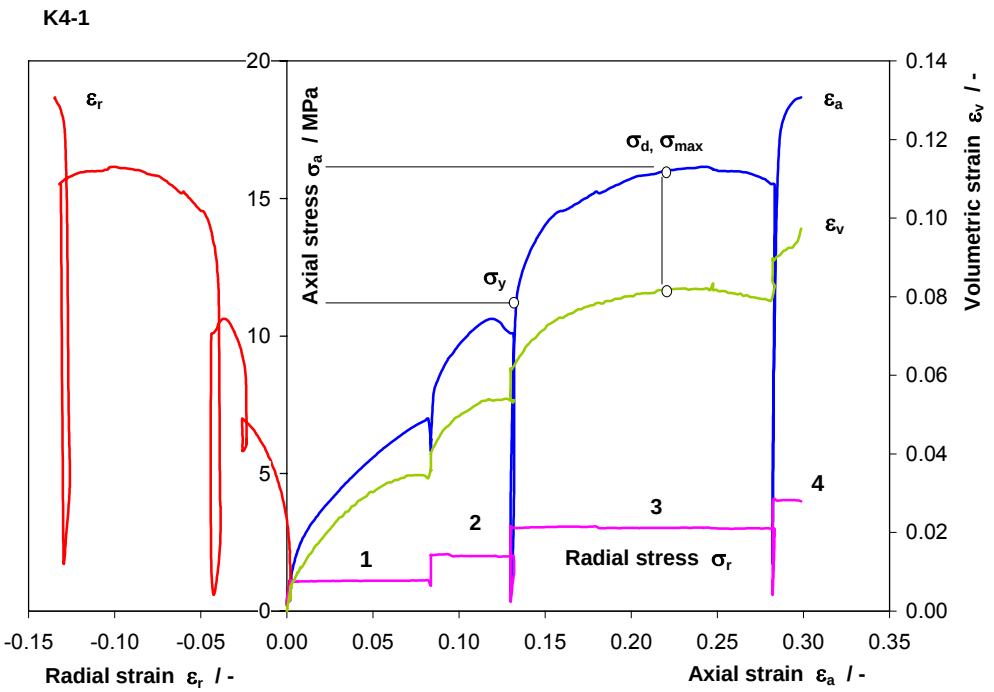

Fig. 4.2.7 Deviatoric stress - strain behaviour of backfill sample K4-1 under multi-failure compression

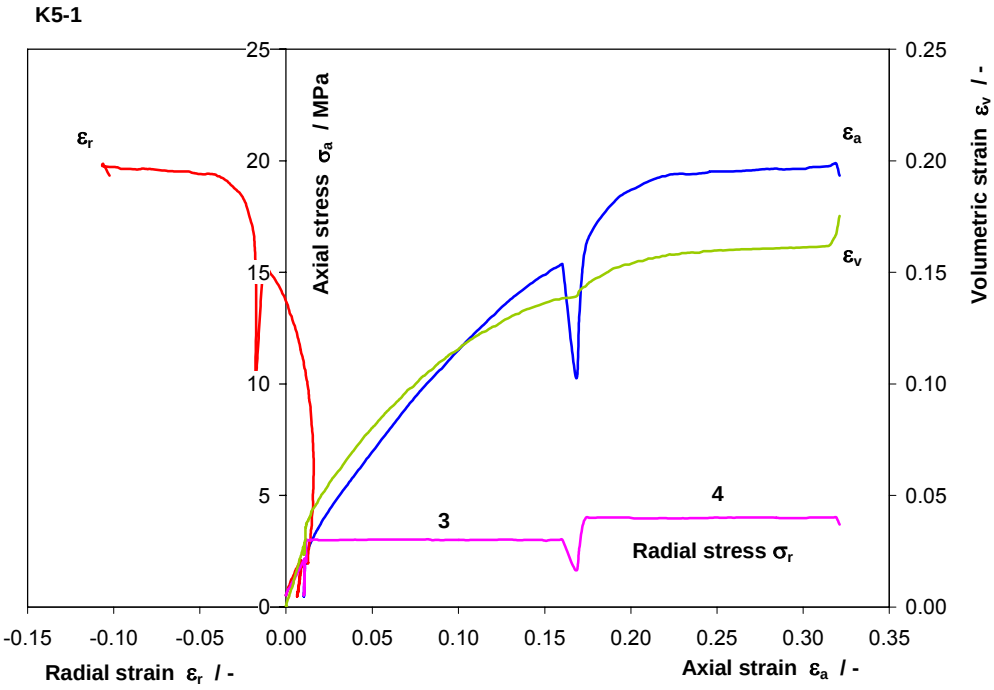

Fig. 4.2.8 Deviatoric stress - strain behaviour of backfill sample K5-1 under multi-failure compression

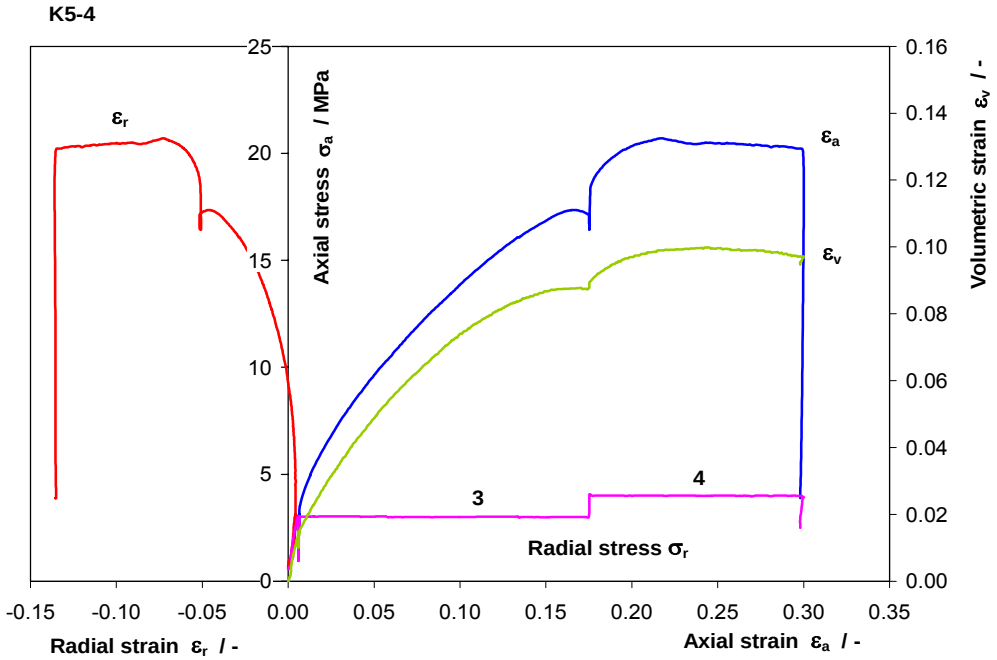

Fig. 4.2.9 Deviatoric stress - strain behaviour of backfill sample K5-4 under multi-failure compression

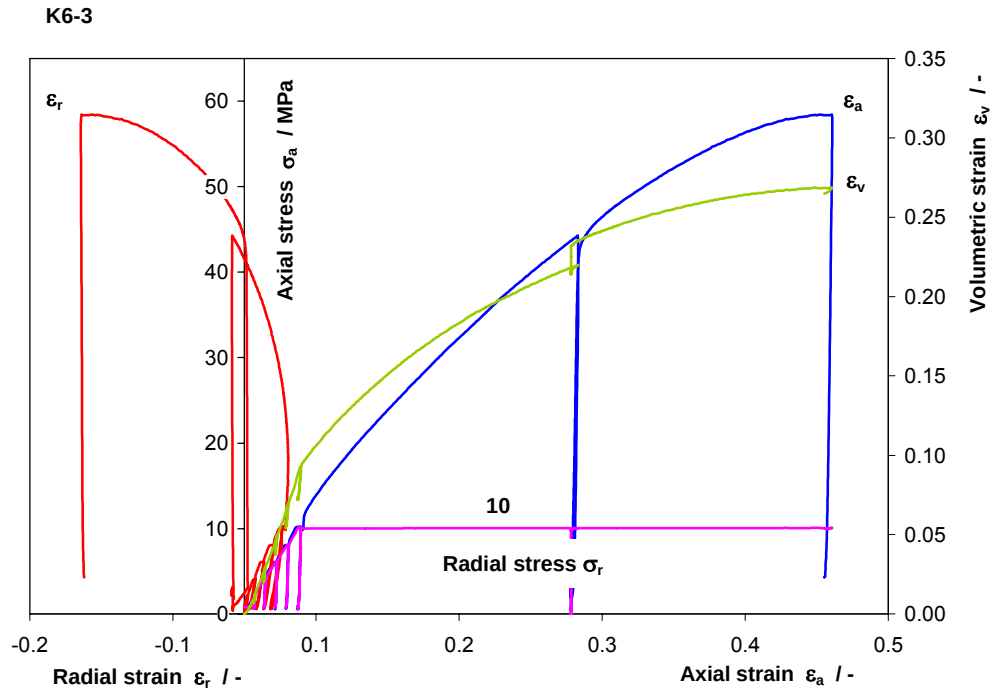

Fig. 4.2.10 Deviatoric stress - strain behaviour of backfill sample K6-3 under multi-failure compression

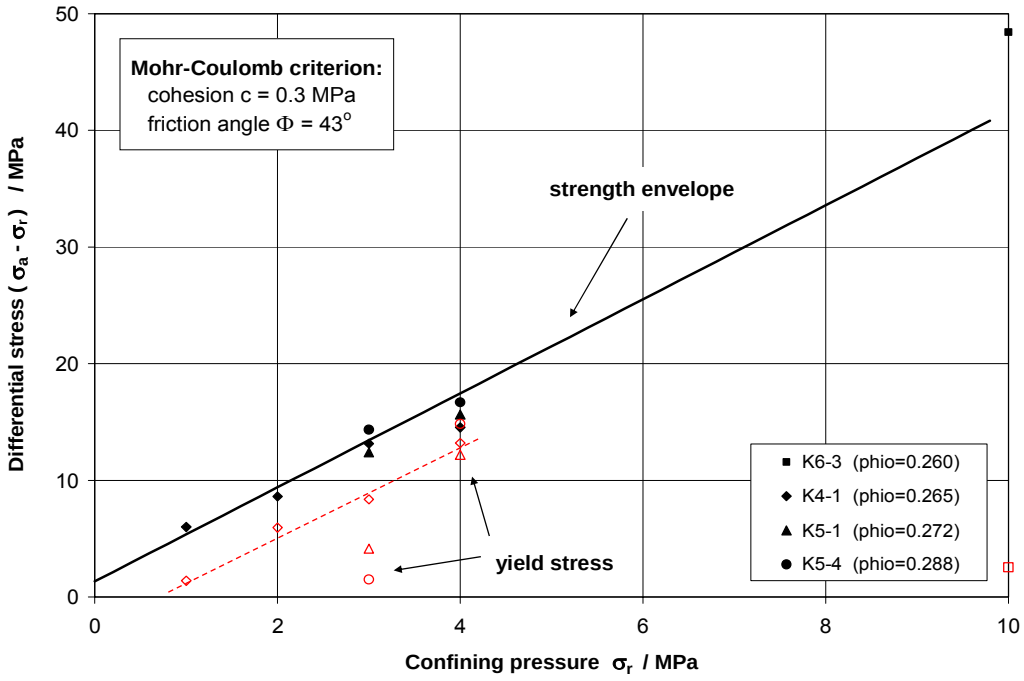

Fig. 4.2.11 Strength envelope and yield stress of backfill samples K4-1, K5-1, K5-4, and K6-3

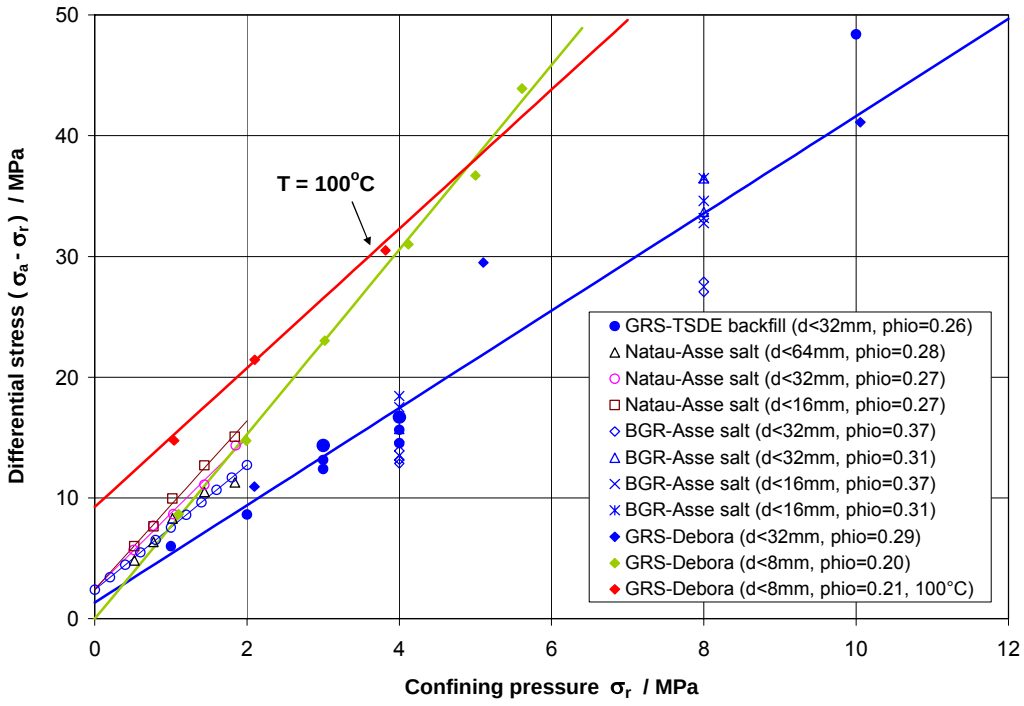

Fig. 4.2.12 Strength of the compacted TSDE backfill samples in comparison with other results obtained on Asse crushed salt

In Figure 4.2.12, the strength of the compacted TSDE backfill is compared with laboratory results of GRS /ROT 99/, BGR /DIE 89/ and /NAT 91/ obtained on Asse crushed salt which was well mixed with defined grain sizes. The strength of the compacted backfill is lower than that of the well mixed material at a similar initial porosity. The higher the initial density, the higher the strength for the same grain size. Fine grains seem to increase the strength. Obviously, increasing temperature results in an increase of the cohesion between salt grains (GRS – tests on grains less than 8 mm both at ambient temperature and at 100 °C). Generally, the cohesion of crushed salt at ambient temperature is less than 0.6 MPa, and the internal friction angle is between 43° and 53°.

4.3 Laboratory Benchmark

In the BAMBUS-I project, a first laboratory benchmark was performed in order to determine the compaction behaviour of the crushed salt backfill from the Asse salt mine, following an agreed loading history at a temperature of 25 °C. Although the participating laboratories (BGR, FZK/INE, and GRS) used comparable boundary conditions, the results showed discrepancies which were attributed to possible sources of errors including differences in sample preparation, test temperatures, and the experimental set-up.

In order to provide a more accurate data base and parameters for modelling of the backfill material, a second laboratory benchmark programme has been undertaken within the project BAMBUS II. In this exercise, measurement results generated by different laboratories were compared. The participants (BGR, FZK/INE, GRS, and IfG) agreed on a common procedure that mainly concerned the choice of the testing material, the boundary conditions for the measurements, and the experimental procedures.

The appropriate testing material to be used in the exercise was crushed salt (air dried) from the Asse salt mine which had also been used in the BAMBUS-I project. The grain density was determined to ρ_s = 2.20 g/cm^3. The grain size distribution is shown in Figure 4.3.1. Coarse grains over 2 mm were limited to a very small fraction of about 1.4 %. The experimental device used by GRS was an axisymmetric triaxial apparatus.

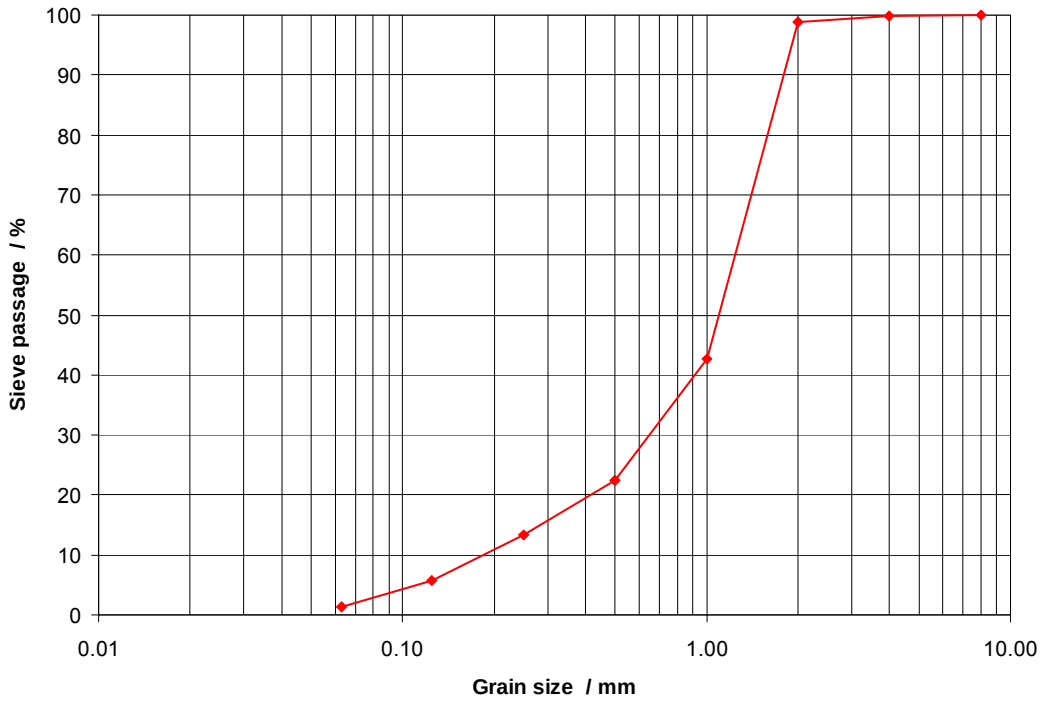

Fig. 4.3.1 Grain size distribution of the crushed salt used in the laboratory benchmark tests

4.3.1 Test Procedures

The benchmark tests were carried out on crushed salt specimens in a triaxial apparatus (Karman type) at ambient and elevated temperature up to 78 °C. The testing machine has been commonly used to determine the thermomechanical behaviour of rock and backfill material, particularly for compaction and permeability tests on crushed salt in recent years /ROT 99/, /DRO 01/. The test procedures proposed by the participating laboratories /STE 00/ were followed. An oedometer-like compression test was proposed, i.e., axial compression with no radial deformation. To maintain this condition in the triaxial test, a special regulating system was developed.

The main element of this system is a bending beam equipped with strain gauges (DMS) (Fig. 4.3.2). The bending beam directly contacts to the specimen over a length of 100 mm. One end of the beam is fixed on the bottom plate. When the specimen is radially deformed, the beam reacts to the bending load that is inferred from strain gauges glued to the beam at the specimen/plate-interface. The deformation of the strain gauges generates electronic signals that are transmitted to an electrohydraulic

regulator which controls the oil pressure in the triaxial cell. The oil pressure increases when the specimen expands in radial direction. Contrarily, when the specimen compacts in the radial direction, the oil pressure decreases. The displacement resolution of the regulating system is ±0.003 mm, giving a strain resolution of 0.003 % (for a specimen 100 mm in diameter).

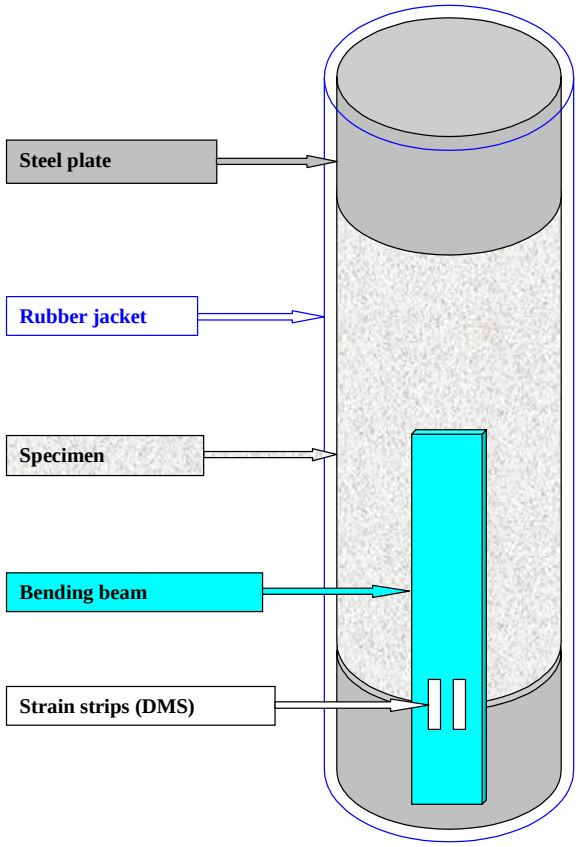

Fig. 4.3.2 Principle of preventing radial deformation of specimens in triaxial tests

Stage 1: *Preparation of Specimens*

Each specimen was prepared by placing 1,970 g of crushed salt into the rubber jacket 100 mm in diameter and about 166 mm high to achieve the specified porosity of 0.31.

Stage 2: *Installation of Specimens in the Triaxial Cell*

The prepared specimens, together with platen and jacket, were placed in the triaxial cell. The cell was then filled with oil and the oil pressure in the cell was increased to about 0.3 MPa. This installation process resulted in a change in sample diameter and

height. Therefore, the initial density of the sample was undefined at this stage of the test. Using the final geometry of the compacted sample at the end of the test and the measured deformations that occurred during the test, the initial state of the sample could be determined.

Stage 3: *Heating of Specimens*

The specimen was heated to the desired temperature under unloaded conditions. During the test, the temperature was kept constant.

Stage 4: *Axial Compression with no Radial Deformation*

The state of the specimen after the hydrostatic pre-compaction in stage 2 and 3 was defined as the initial condition. Axial compression started by imposing a constant strain rate of about 2E-5 s^{-1} (displacement rate of 0.2 mm/min). The axial load increased to about 10 MPa. During the axial compression, radial deformation of the specimen was prevented by automatically regulating the oil pressure in the cell.

Stage 5: *Creep Consolidation*

To start creep consolidation, strain-controlled loading applied in the compression phase must be changed to stress-controlled loading. This change was performed at unloaded conditions to avoid potential damage of the specimen. After changing the test control, the specimen was loaded again at an axial stress rate of 0.5 MPa/min up to the axial stress of about 10 MPa. Creep consolidation followed maintaining the condition of no-radial-deformation. The creep period duration was 3 to 7 days.

Stage 6: *Post-Test Specimen Characterization*

After the creep period, the specimen was unloaded and removed from the cell. Height, mass, and density of the specimen were measured again. Based on these measurements, an average diameter was calculated taking into account the off-circle position of the bending beam. The values obtained were used to determine the initial condition of the specimen as described above.

The following test parameters were measured or calculated:

- Axial stress $\sigma_a = F/A$ F = axial force, A = cross section of the specimen
- Radial stress $\sigma_r = p$ p = oil pressure in the cell
- Mean stress $\sigma_m = (\sigma_a + 2\ \sigma_r) / 3$
- Radial/axial stress ratio $k_r = \sigma_r / \sigma_a$
- Mean/axial stress ratio $k_m = \sigma_m / \sigma_a$
- Axial strain $\varepsilon_a = (H_o - H) / H_o$ H = height of the specimen, H_o = initial height of the specimen
- Radial strain $\varepsilon_r = (D_o - D) / D_o$ D = diameter of the specimen, D_o = initial diameter of the specimen
- Volumetric strain $\varepsilon_v = (V_o - V) / V_o$ V = volume of the specimen, V_o = initial volume of the specimen
- Porosity * $\phi = 1 - (\rho / \rho_s)$ ρ = bulk density of the specimen, ρ_s = grain density of the specimen
- Volumetric strain rate (consolidation rate) $\dot{\varepsilon}_v = d\varepsilon_v / dt$ t = time

* in figures n = ϕ = porosity

4.3.2 Experimental Results

An overview of the laboratory benchmark experiments is given in Table 4.3.1. All specimens were subjected to an axial stress of up to about 10 MPa with a strain rate of 2E-5 s^{-1} at constant temperatures of 21 to 78 °C. After axial compression, three specimens (BEN-4/5/7) were consolidated further in creep for 3 to 7 days under the constant axial stress levels and temperatures.

During installation of the specimens, some changes in their initial conditions occurred. Therefore, the specified porosity of ϕ_o = 0.31 could not be exactly maintained. The determined values ranged from ϕ_o = 0.26 to ϕ_o = 0.32.

In the first experiments (Ben-1 to 4), special attention was paid to testing and calibration of the regulating system to prevent radial deformation so that the oedometer condition was not fully held during these tests (Fig. 4.3.3 and 4.3.4). In the other tests (BEN-5 to 8), the regulating system was exactly adjusted (Fig. 4.3.3 and 4.3.4).

Tab. 4.3.1 Overview of laboratory benchmark tests on crushed salt

			Initial conditions				Loading			
Specimen No.	Com-paction	Creep	D_o	H_o	ρ_o	ϕ_o	ε_a-rate	σ_a-creep	creep time	T
			mm	mm	g/cm^3	–	s^{-1}	MPa	h	°C
Ben-1	yes	no	101.2	160.9	1.523	0.31	2E-5			23
Ben-2	yes	no	98.3	159.5	1.626	0.26	2E-5			21
Ben-3	yes	no	99.6	156.0	1.621	0.27	2E-5			77
Ben-4	yes	yes	100.0	158.0	1.588	0.28	2E-5	9.17	120	75
Ben-5	yes	yes	99.8	163.4	1.542	0.30	2E-5	10.18	70	25
Ben-6	yes	no	100.0	165.0	1.52	0.31	2E-5			78
Ben-7	yes	yes	102.0	161.6	1.492	0.32	2E-5	9.87	168	75
Ben-8	yes	no	100.7	165.1	1.500	0.32	2E-5			70

			Final results							
Specimen No.	Com-paction	Creep	D_E	H_E	ρ_E	ϕ_E	σ_{aE}	σ_{rE}	σ_{mE}	$k_r=\sigma_{rE}/\sigma_{aE}$
			mm	mm	g/cm^3	–	MPa	MPa	MPa	-
Ben-1	yes	no	101.6	138.8	1.700	0.23	9.72	2.44	4.87	0.25
Ben-2	yes	no	98.6	142.4	1.810	0.18	10.94	2.31	5.19	0.21
Ben-3	yes	no	100.1	140.2	1.786	0.19	10.41	2.38	5.06	0.23
Ben-4	yes	yes	101.0	135.6	1.812	0.18	9.17	3.68	5.51	0.40
Ben-5	yes	yes	99.8	143.5	1.755	0.21	10.18	3.41	5.67	0.34
Ben-6	yes	no	100.0	142.7	1.756	0.20	9.93	2.87	5.22	0.29
Ben-7	yes	yes	102.0	132.1	1.814	0.18	9.87	3.61	5.70	0.37
Ben-8	yes	no	100.7	144.5	1.714	0.22	9.98	3.47	5.64	0.35

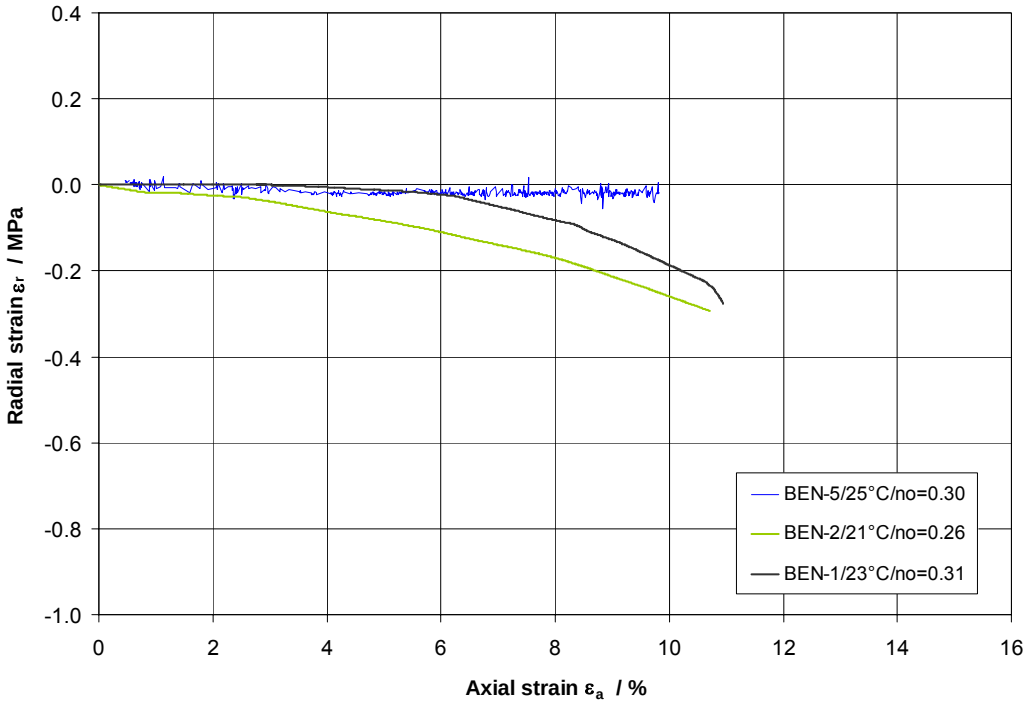

Fig. 4.3.3 Radial strain/axial strain-curves at room temperature

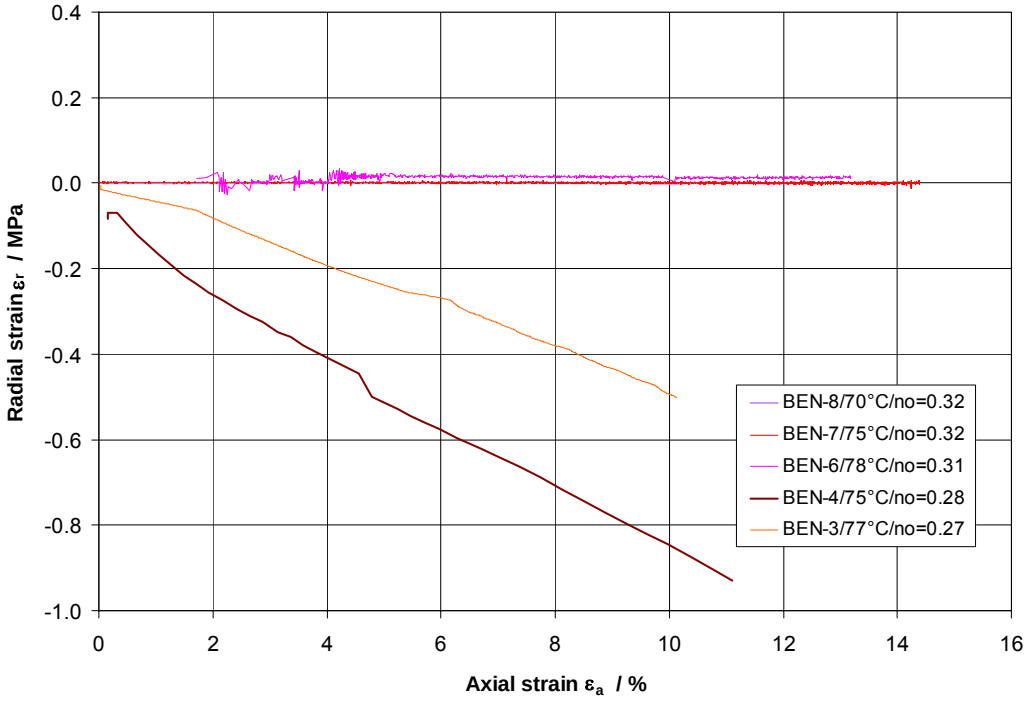

Fig. 4.3.4 Radial strain/axial strain-curves at temperatures of 70 – 78 °C

Axial Compression

In Figures 4.3.3 to 4.3.8, the compression curves (radial strain, axial stress, and radial stress against axial strain) of all tests are summarized.

From Figures 4.3.5 and 4.3.6 it can be seen that an increase in axial strain leads to a non-linear increase in axial stress. The axial stress/axial strain-curves are quite similar. The resulting axial stress by increasing axial strain is dependent upon initial porosity, temperature, and radial deformation. Generally it can be stated that the axial stress is as lower as higher are initial porosity, temperature, and radial dilatation (negative strain).

As it is shown in Figures 4.3.7 and 4.3.8, the resulting radial stress increases with increasing axial strain. In the tests with no radial deformation, higher radial stresses were achieved than in those tests with some radial dilatation (Fig. 4.3.3 and 4.3.7: BEN-5 and BEN-1 which were performed under similar initial and boundary conditions).

The ratio of radial stress to axial stress obtained under oedometer conditions was evaluated. The comparison of Figures 4.3.5 to 4.3.7 and 4.3.6 to 4.3.8 reveals that the resulting radial stress is always lower than the axial stress in the oedometer-like compression. For the specimens BEN-1 to 4 with some radial dilatation, the radial/axial stress ratio was lower than for the specimens in full oedometer condition.

In Figure 4.3.9, the radial/axial stress ratio is given as a function of porosity both in the compression and the creep phase. The radial/axial stress ratio increases linearly with decreasing porosity. Basing on these data, a linear extrapolation was made indicating that the stress ratio tends towards unity at full compaction with $\phi = 0$ (Fig. 4.3.10). The stress ratio which was obtained during the tests ranges from about 0.1 to 0.38 in a porosity range of 0.30 to 0.18. In the studied temperature range of 25 to 78 °C, no significant effect of temperature on the stress ratio was observed. The measured data are lower than the experimental data of G.3S and FZK/INE /BEC 99/. With grains less than 2 mm, G.3S true oedometer tests (50 mm diameter) on Asse crushed salt obtained $k_r = 0.35 – 0.40$ for $\phi = 0.15 – 0.35$ by measuring lateral pressure. FZK/INE true triaxial creep tests (250 mm side length) on Asse crushed salt with grains < 31 mm observed $k_r = 0.36 – 0.38$ for $\phi = 0.27 – 0.21$ in oedometer condition. For low porosity values, however, the extrapolation of GRS data is comparable with the results of FZK/INE (Fig. 4.3.10).

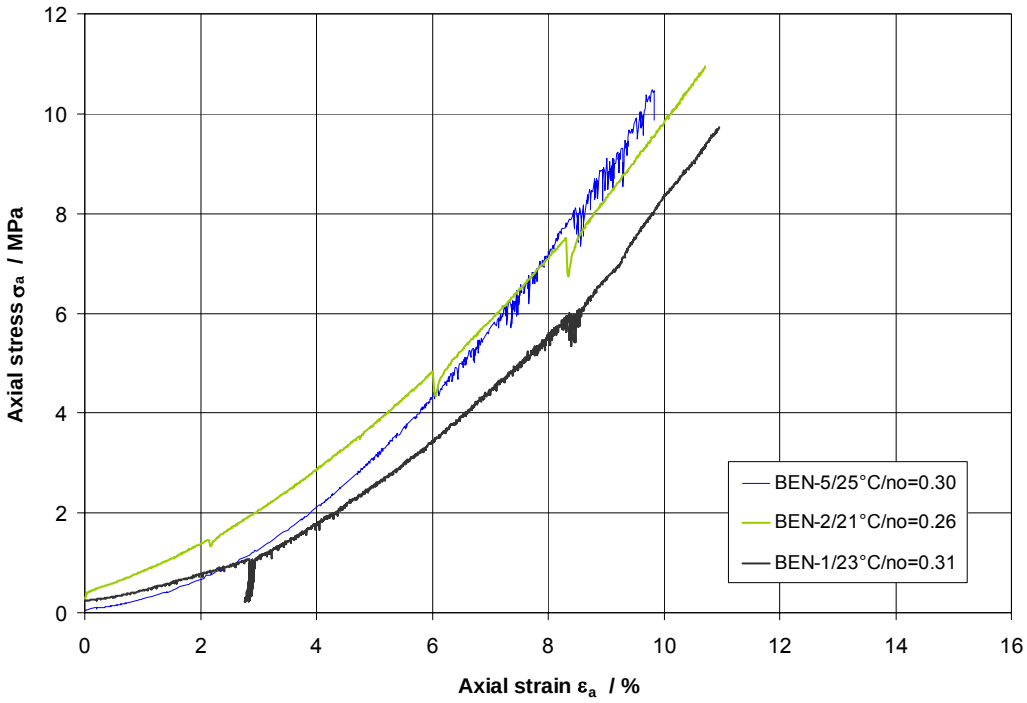

Fig. 4.3.5 Axial stress/axial strain-curves at room temperature

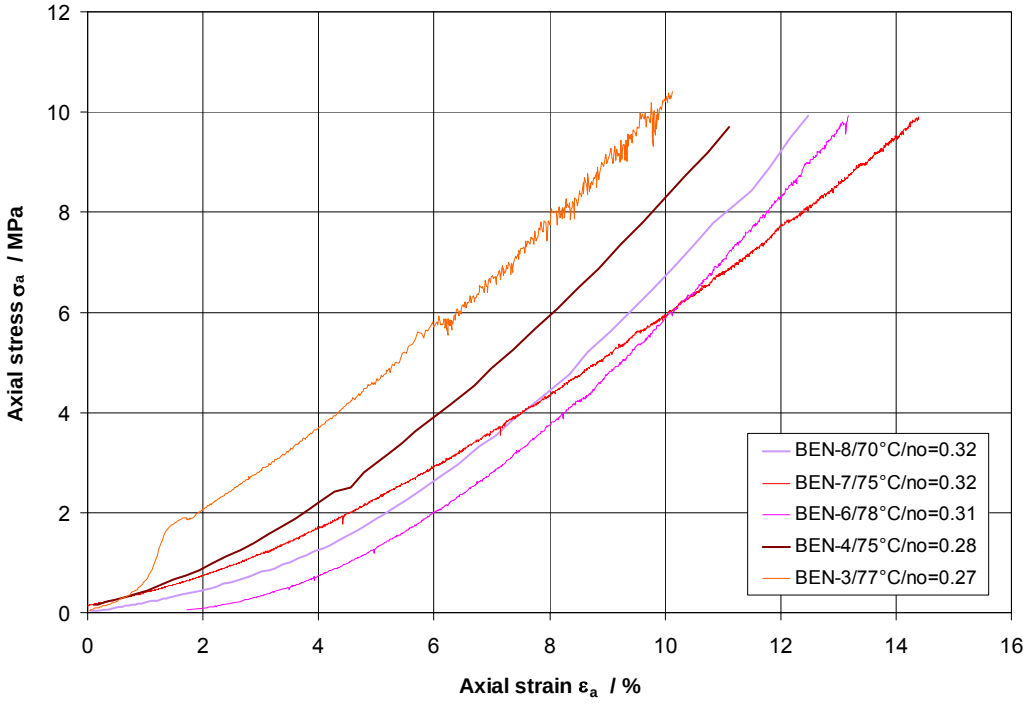

Fig. 4.3.6 Axial stress/axial strain-curves at temperatures of 70 – 78 °C

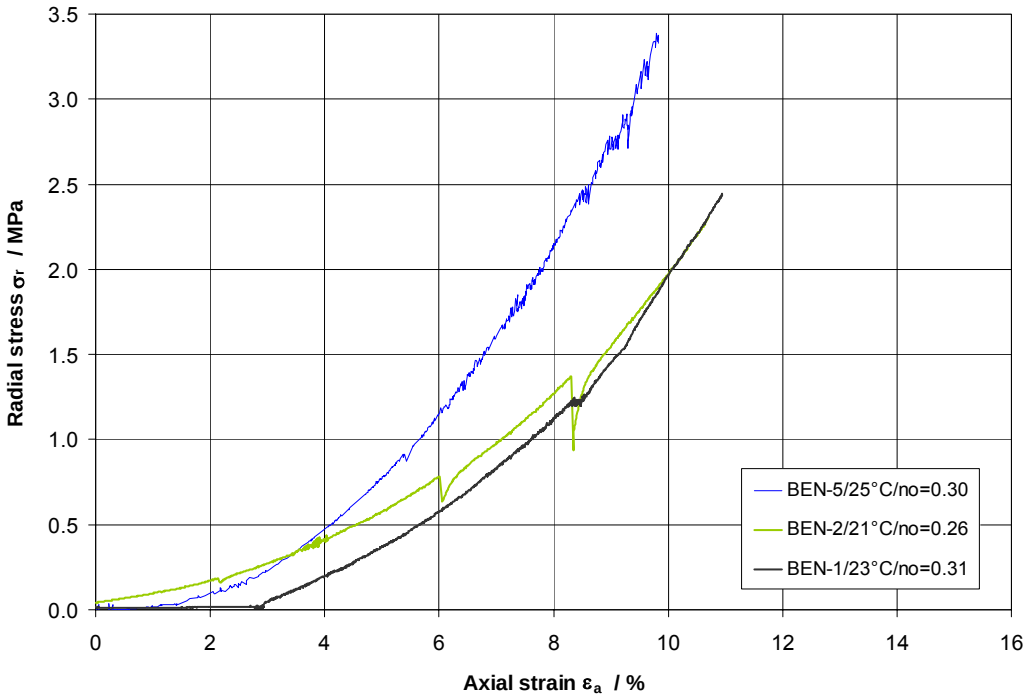

Fig. 4.3.7 Radial stress/axial strain-curves at room temperature

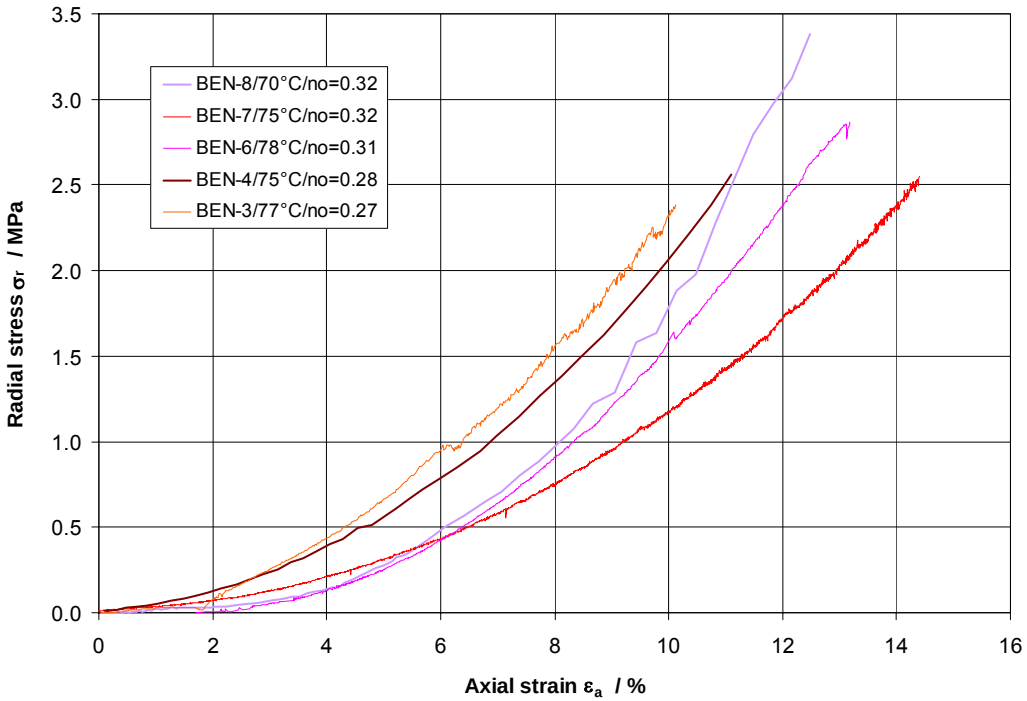

Fig. 4.3.8 Radial stress/axial strain-curves at temperatures of 70 – 78 °C

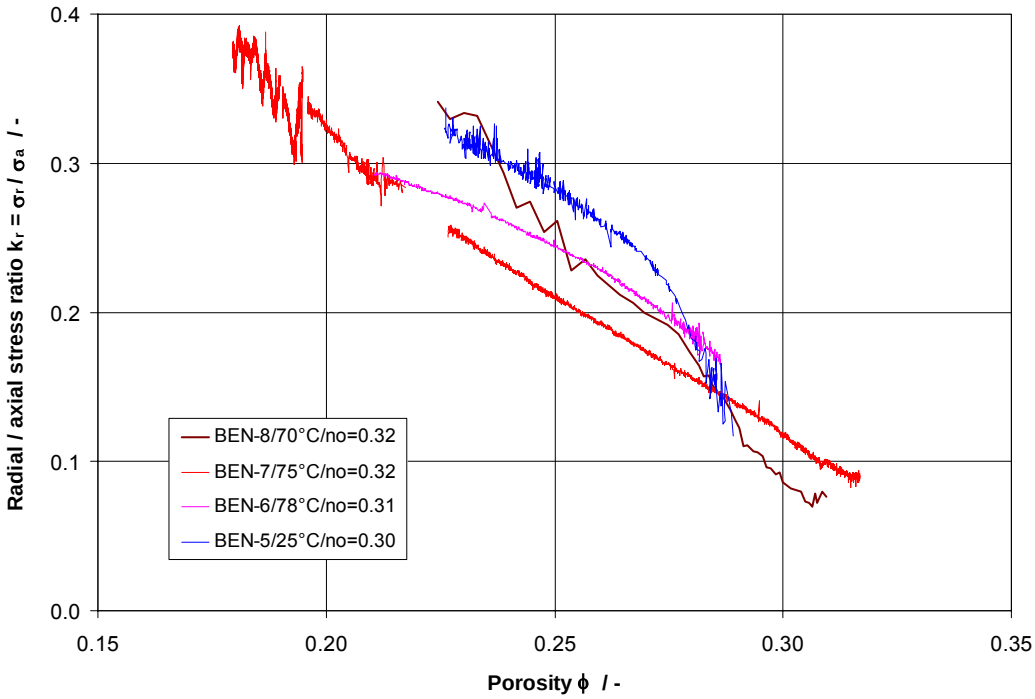

Fig. 4.3.9 Ratio of radial stress/axial stress as function of porosity

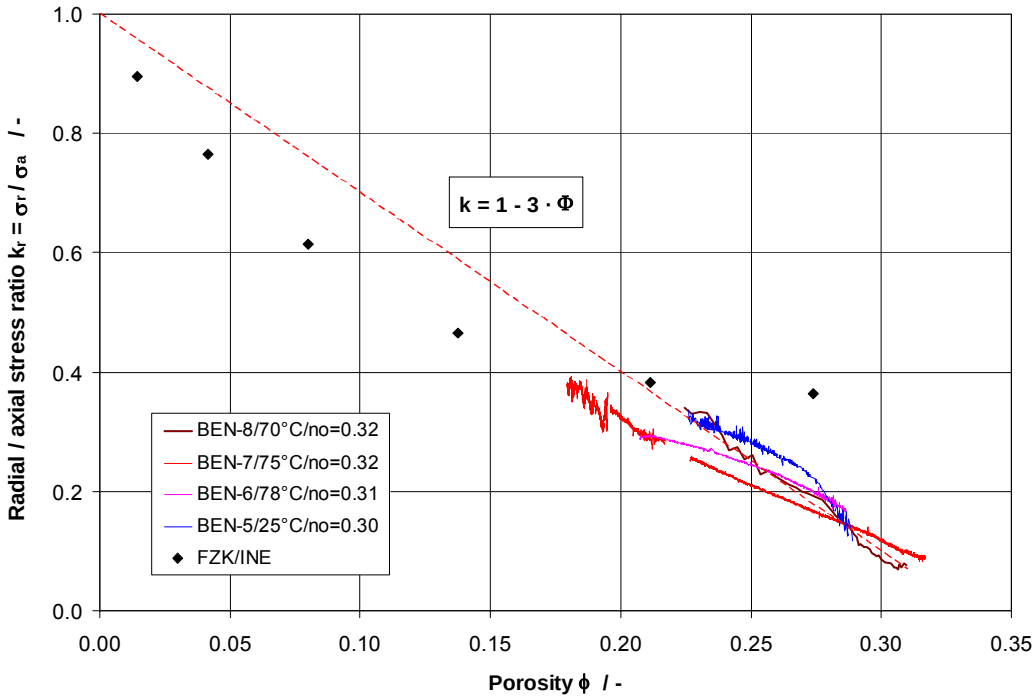

Fig. 4.3.10 Extrapolation of radial stress/axial stress ratio as function of porosity

In common evaluations of oedometer tests, the stress state of the specimens is usually assumed to be hydrostatic, i.e., axial stress is equal to radial stress. To examine the effects of this assumption on the compaction behaviour of crushed salt, the values of mean stress and axial stress, which were obtained in the oedometer-like tests, are compared as a function of porosity (Fig. 4.3.11). Obviously, the mean stress is still lower than the axial stress due to the lower radial stress during compaction. However, the ratio of mean stress to axial stress increases linearly with decreasing porosity ranging from $k_m \approx 0.4$ for $\phi = 0.3$ to $k_m \approx 0.55$ for $\phi = 0.23$ and towards $k_m = 1$ at $\phi = 0$ (Fig. 4.3.12). This result indicates that the assumption of axial stress being equal to radial stress made in common evaluations of oedometer tests can lead to a large uncertainty of the stress state.

Creep Consolidation

Figures 4.3.13 to 4.3.16 show the evolution of stresses, strains, porosity, and volumetric strain rate obtained from three triaxial creep tests on specimens BEN-4/5/7 at 25 °C and 75 °C. In each test, the axial stress level was kept constant during creep consolidation except the short-term overstress of about 0.3 MPa in test BEN-7 (Fig. 4.3.13). Radial stress and hence mean stress, however, increased slightly with increasing consolidation. In test BEN-7, for example, the radial stress increased from about 3.4 MPa to about 3.8 MPa during 7 days of creep consolidation from $\phi = 0.20$ to 0.18. Fluctuations of the radial stress were recorded within a range of about 0.15 MPa, mainly due to changes in temperature ($\Delta T = \pm 0.5$ °C at 75 °C and $\Delta T = \pm 1.0$ °C at 25 °C).

Figure 4.3.14 shows an excellent maintaining of the condition of no radial deformation during the creep in the tests. Only in the beginning of the compression phase of test BEN-4, the specimen was dilated in radial direction up to about 0.1 %, but was then held constant in the further creep phase.

As it is shown in Figure 4.3.15, the time dependent consolidation rates obtained at 75 °C exhibit a remarkable conformity. The temperature effect on the consolidation rate can be clearly recognized in another plot of volumetric strain rate versus porosity (Fig. 4.3.16). The increase in temperature accelerates the consolidation of the material.

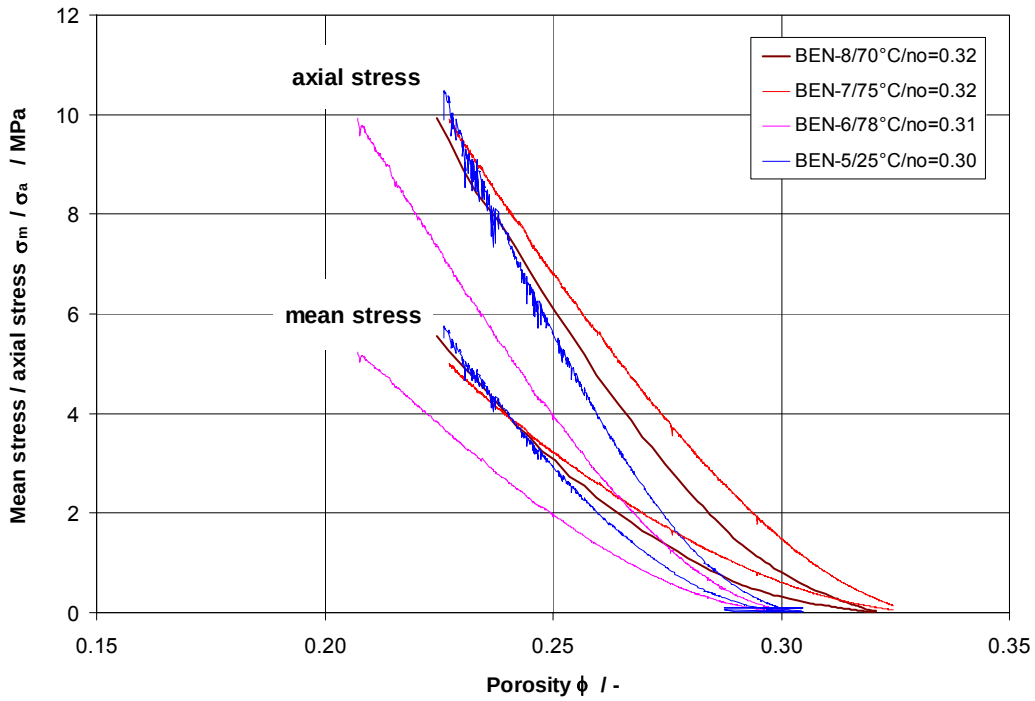

Fig. 4.3.11 Comparison between mean stress/porosity-curves and axial stress/ porosity-curves in oedometer condition

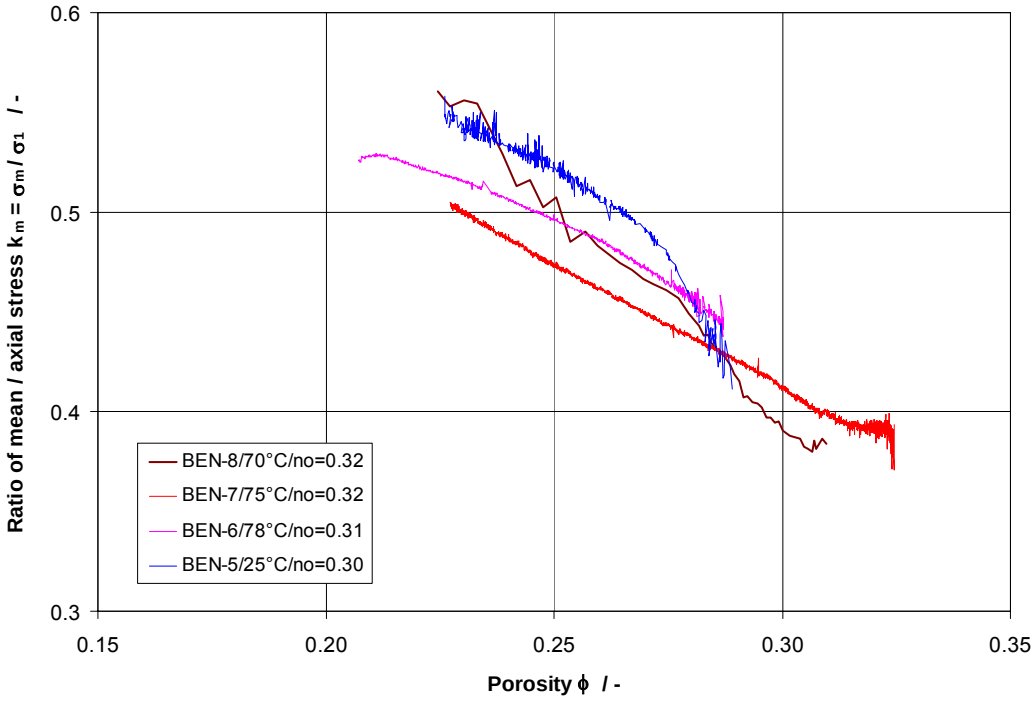

Fig. 4.3.12 Ratio of mean stress/axial stress as function of porosity

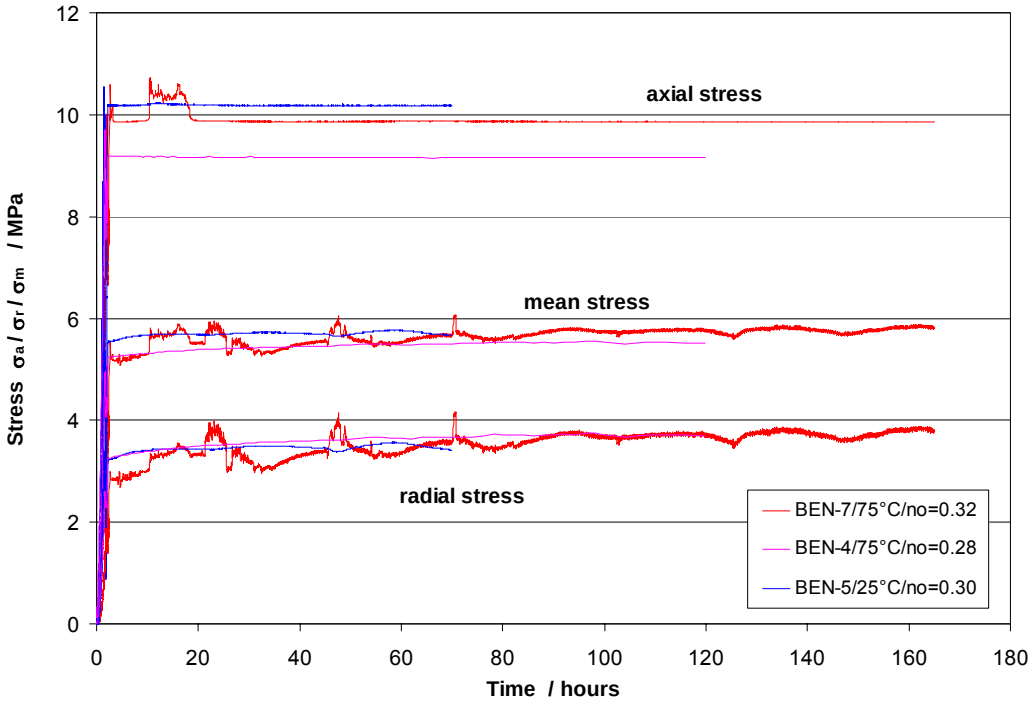

Fig. 4.3.13 Evolution of axial/radial/mean stress in triaxial creep tests

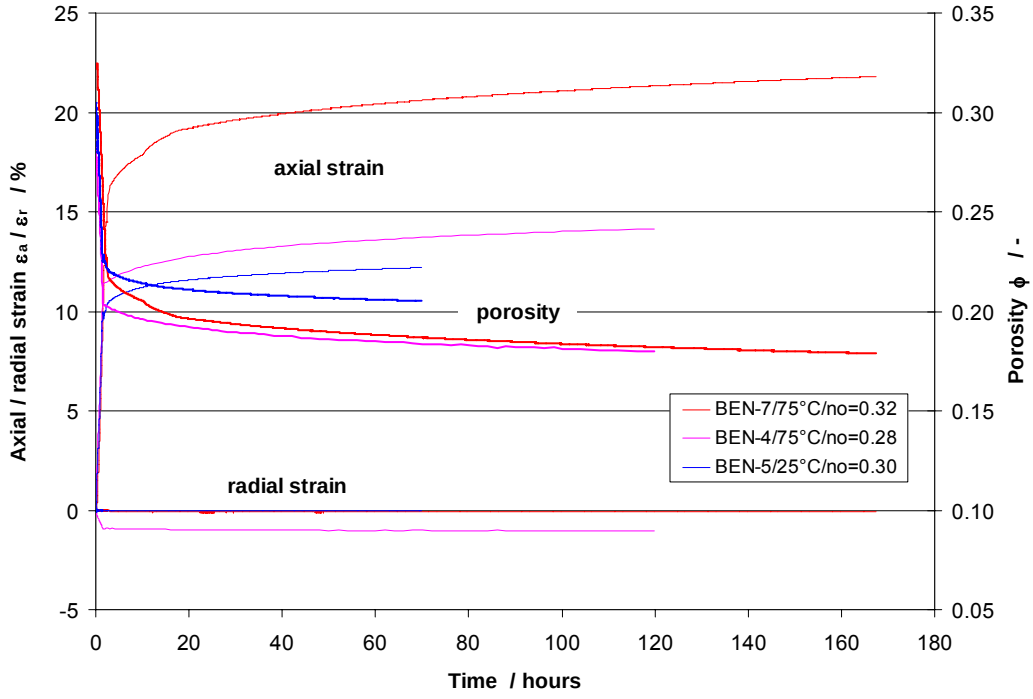

Fig. 4.3.14 Evolution of axial/radial strain and porosity in triaxial creep tests

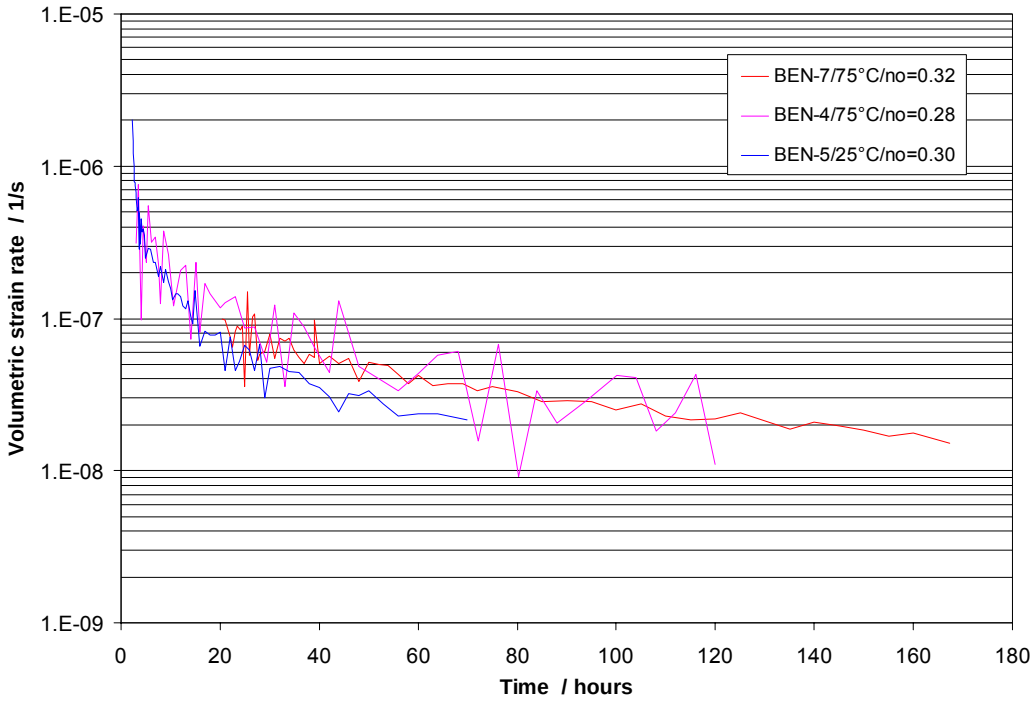

Fig. 4.3.15 Evolution of volumetric strain rate in triaxial creep tests

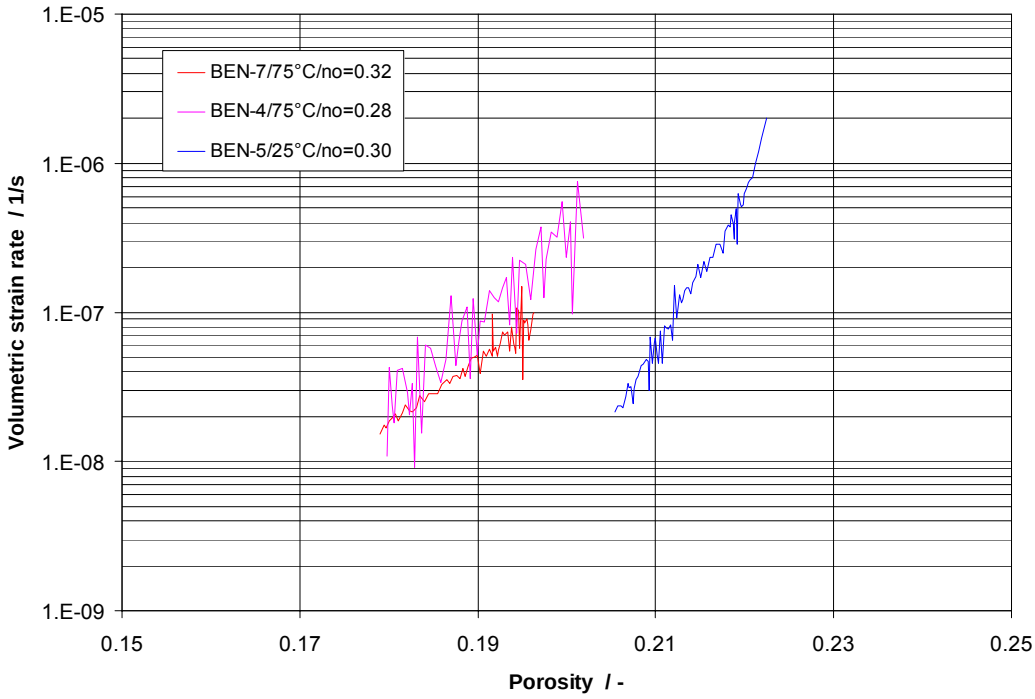

Fig. 4.3.16 Volumetric strain rate as function of porosity

4.3.3 Consolidation parameters

In oedometer tests, the assumption of axial stress as hydrostatic stress of specimens can lead to a high uncertainty in the consolidation of crushed salt. But it is also of importance to examine the effects which this assumption will have on the consolidation parameters or on the stress-, porosity-, and temperature-dependence of the volumetric strain rate of crushed salt. For this purpose, the hydrostatic consolidation model of Zhang was chosen /ZHA 93/:

$$\dot{\varepsilon}_v = A \exp\left(\frac{-Q}{RT}\right)\left(\frac{\sigma}{\sigma_o}\right)^n \left[\ln\left(\frac{\phi_o(1-\phi)}{\phi(1-\phi_o)}\right)\right]^{-m} \qquad (4.5)$$

where

- $\dot{\varepsilon}_v$ = volumetric strain rate (s^{-1})
- T = absolute temperature (K)
- Q = activation energy (kJ/mole)
- R = universal gas constant (8.3143E-3 kJ/(mole K))
- σ = hydrostatic stress (MPa)
- σ_o = reference stress (1 MPa)
- ϕ = porosity (-)
- ϕ_o = initial porosity (-)
- A, n, and m = parameters.

At first, the parameter values were determined only basing on the consolidation rate/porosity-curves obtained in the creep phase using average values of mean stress as shown in Figure 4.3.17 and Table 4.3.2. Using the preliminary values of the parameters, the mean stress/porosity-curves obtained in the axial compression phase were predicted for all tests (Fig. 4.3.18 and 4.3.19). Reasonable agreements were found between calculated and measured consolidation curves for both phases, the axial compression and the creep consolidation. Some differences could be caused by uncontrolled pre-compaction in the installation stage.

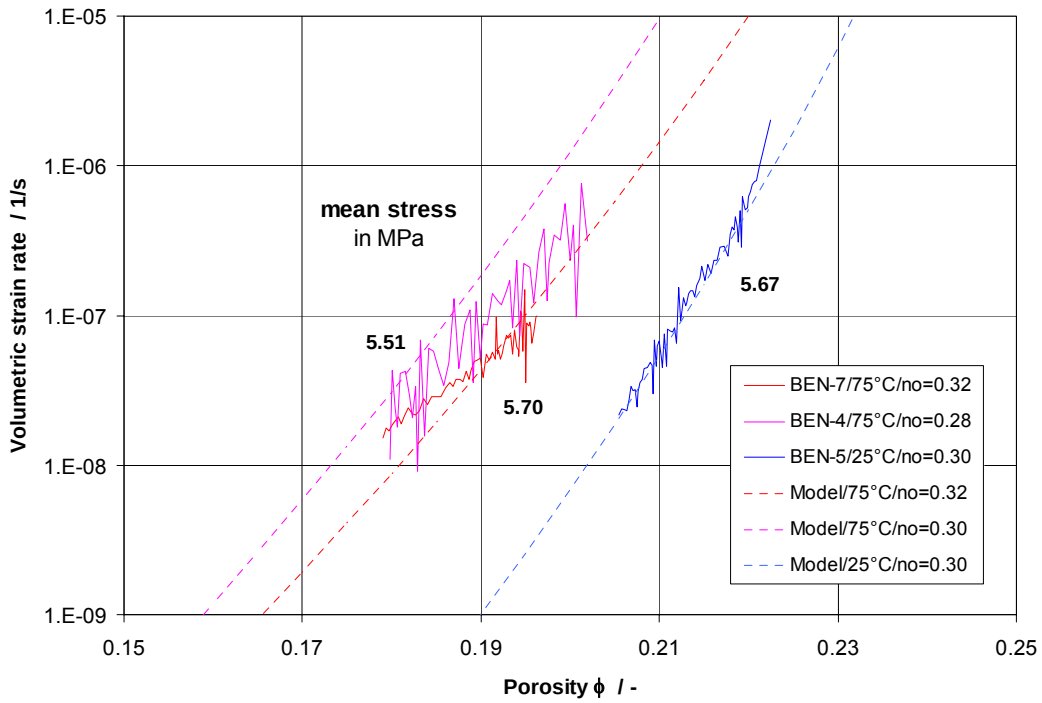

Fig. 4.3.17 Volumetric strain rate as function of porosity at constant mean stresses and temperatures

Tab. 4.3.2 Parameters of Zhang's model for Asse crushed salt with different grain sizes obtained from GRS triaxial tests and BGR oedometer tests

Test type	GRS triaxial test	GRS triaxial test	BGR oedometer test	BGR oedometer test
Grain size d	< 2 mm	< 8 mm	< 31 mm	< 0.125 mm
ϕ_o	0.26 – 0.32	0.32 – 0.37	0.31	0.48
A (s^{-1})	2E-6	2E-5	1.4	3.3E-5
Q (kJ/mole)	96	96	156	133
n	13	13	14.3	15
m	17	17	17	21.7

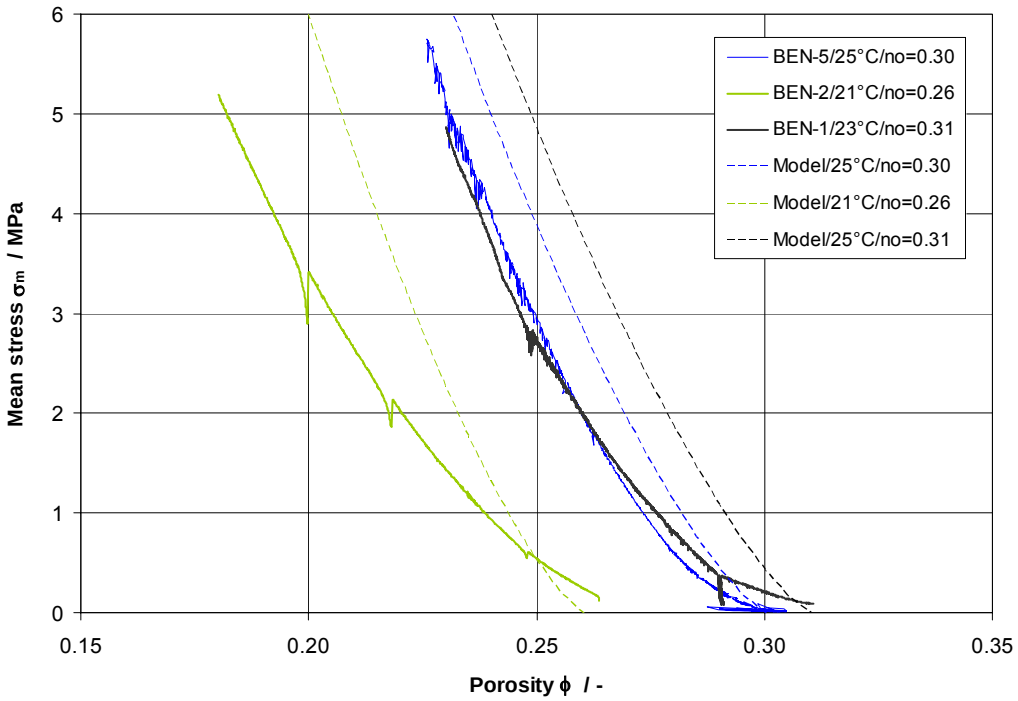

Fig. 4.3.18 Comparison between measured and calculated mean stress as function of porosity at room temperature

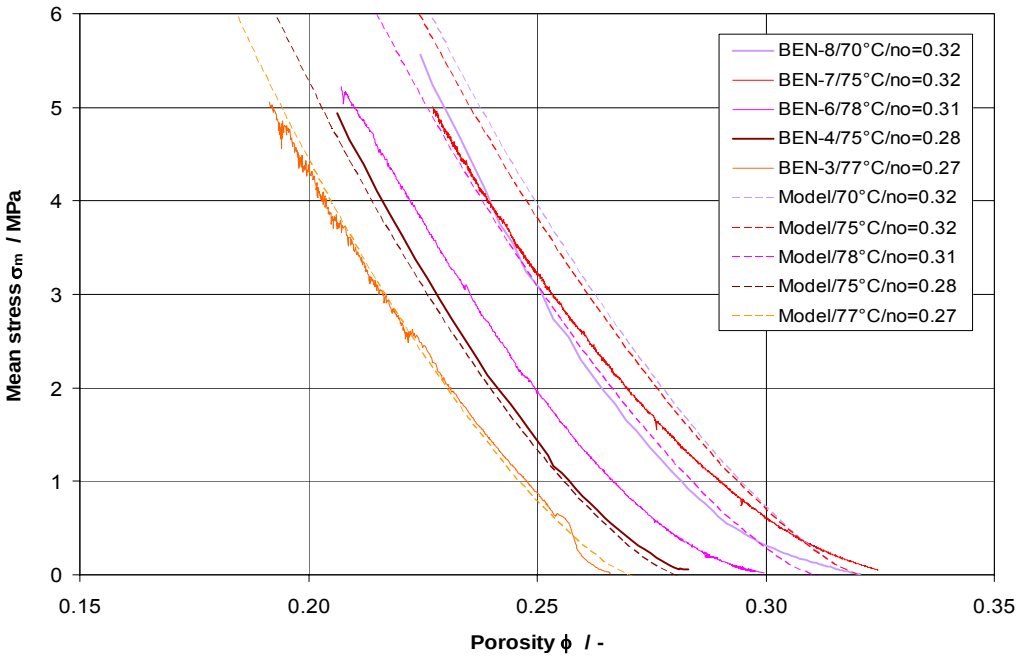

Fig. 4.3.19 Comparison between measured and calculated mean stress as function of porosity at elevated temperature

Taking axial stress instead of mean stress according to $\sigma_m = k_m \cdot \sigma_a$ in Zhang's equation gives $\dot{\varepsilon}_v(\sigma_a) = (k_m)^n \dot{\varepsilon}_v(\sigma_m)$. Accordingly, using axial stress as hydrostatic stress to evaluate the compaction behaviour of a material in oedometer condition can lead to a change in consolidation rate by a factor of $(k_m)^n$. The factor observed in the oedometer-like testing conditions varies in a very large range of $0.4^{13} \sim 0.55^{13}$ = 6.7E-6 ~ 4.2E-4 or 4 to 6 orders of magnitude.

For modelling the axial stress/porosity-curves obtained in the triaxial tests, only one parameter A = 1E-9 s^{-1} was renewed and the other parameters (n, m, and Q) remained unchanged. Figures 4.3.20 to 4.3.22 show reasonable agreements between calculated and measured curves of axial stress versus porosity. This leads to the important conclusion that stress-, porosity-, and temperature-dependence of the consolidation rate obtained both by using mean stress and by using axial stress as hydrostatic stress in oedometer condition result in the same values of the parameters n, m, and Q in both evaluation cases. But the assumption of axial stress being equal to radial stress can lead to a high uncertainty of the parameter A.

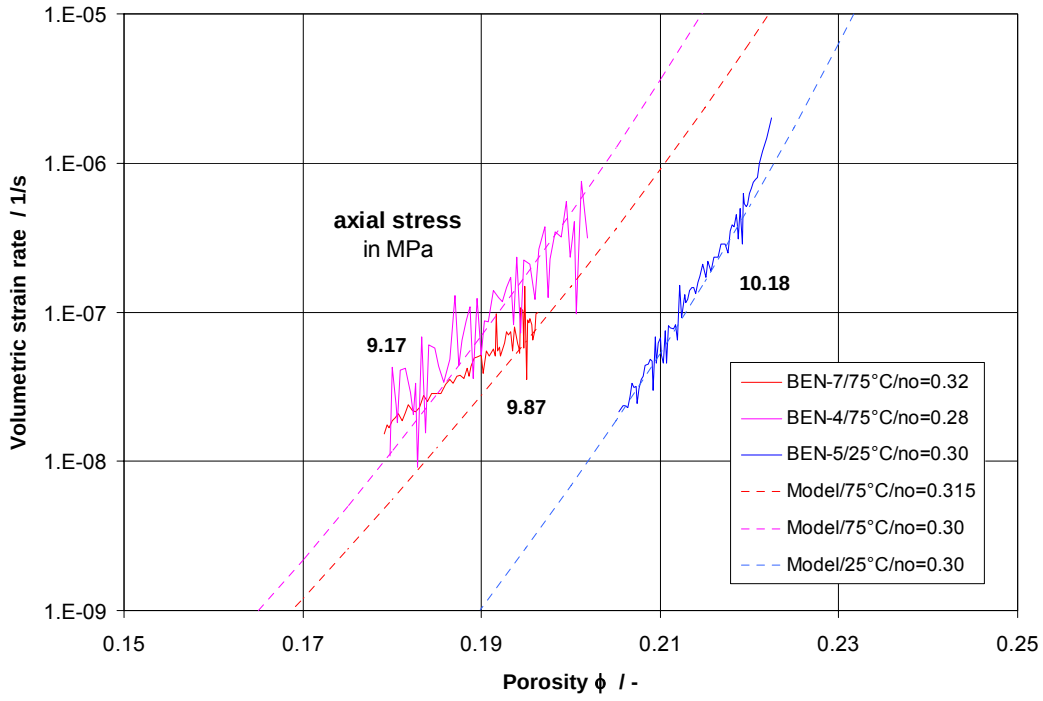

Fig. 4.3.20 Volumetric strain rate as function of porosity at constant axial stresses and temperatures

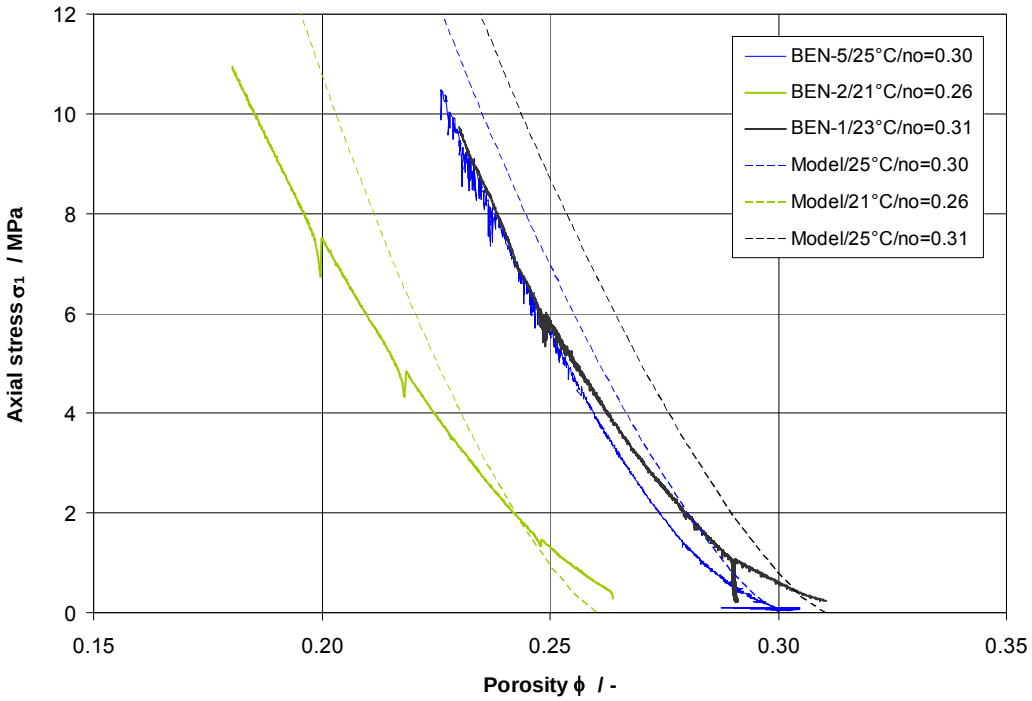

Fig. 4.3.21 Comparison between measured and calculated axial stress as function of porosity at room temperature

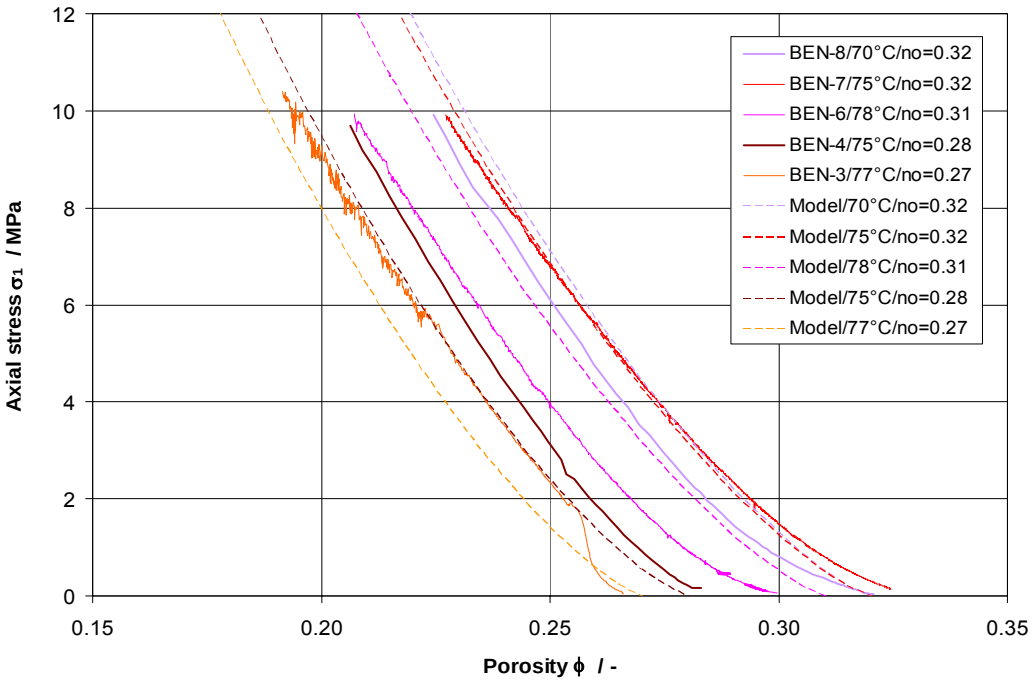

Fig. 4.3.22 Comparison between measured and calculated axial stress as function of porosity at elevated temperature

In the frame of the DEBORA-project /ROT 99/, a series of triaxial compaction tests on Asse crushed salt were conducted with grains less than 8 mm (Fig. 4.3.23). The results of the hydrostatic compaction experiments with a compaction rate of 2.3E-5 s^{-1} at 25 °C were predicted using Zhang's model with the same parameter-values (n, m, and Q) determined for the grain sizes < 2 mm, but with a different parameter A = 2E-5 s^{-1}. Figure 4.3.24 shows a good agreement between the measured data and the predictions.

Table 4.3.2 gives a comparison of the parameters obtained from GRS triaxial tests on fine-grained salt with two grain size distributions and from BGR oedometer tests on both coarse-grained salt (reference material) and salt powder /STU 95/. It can be seen that

- a high stress exponent of n = 13 observed from GRS triaxial tests on fine-grained salt is very close to the values n = 14.3 to 15 obtained from BGR oedometer tests on coarse-grained salt and powder salt;
- the parameter m = 17 is the same for both fine-grained salts tested in GRS triaxial tests and for the reference material tested in BGR oedometer tests;
- the value of the activation energy Q = 96 kJ/mole obtained from GRS triaxial tests is lower than BGR-values of Q = 133 to 156 kJ/mole;
- the values of the parameter A are different mainly because of grain size and evaluation methods (mean stress or axial stress used as hydrostatic stress in the oedometer condition).

4.3.4 Conclusions

From the triaxial compaction experiments, the following conclusions can be drawn.

- The specially developed regulating system using a bending beam was successfully applied to prevent radial deformation of the specimen in the triaxial compression tests.

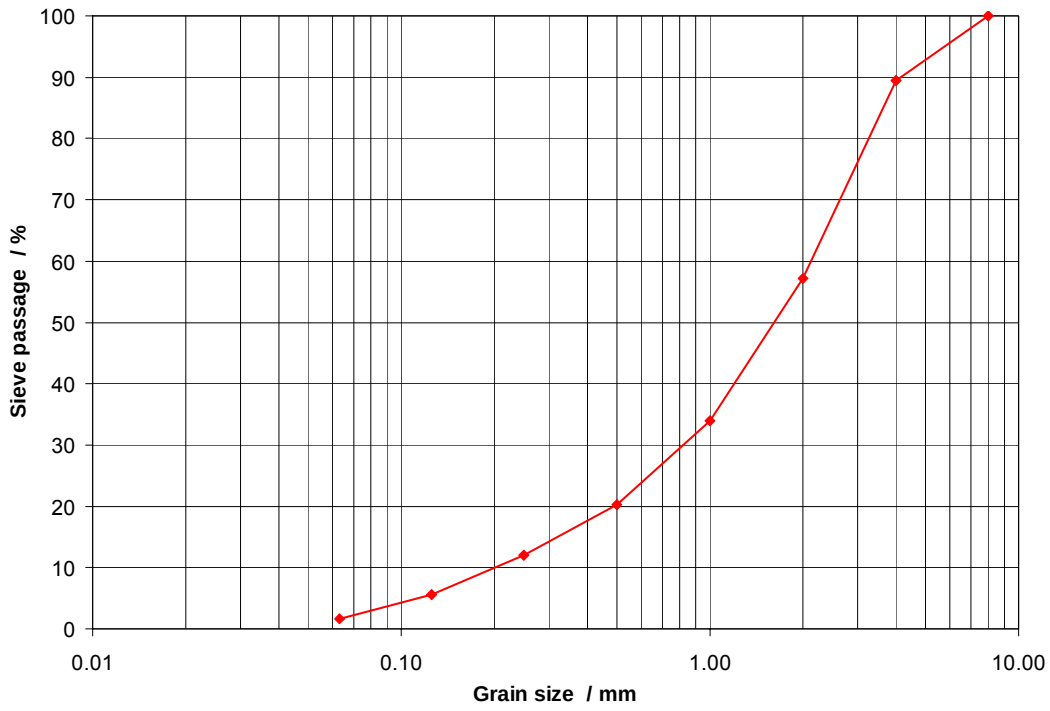

Fig. 4.3.23 Grain size distribution of the crushed salt used in the DEBORA-tests

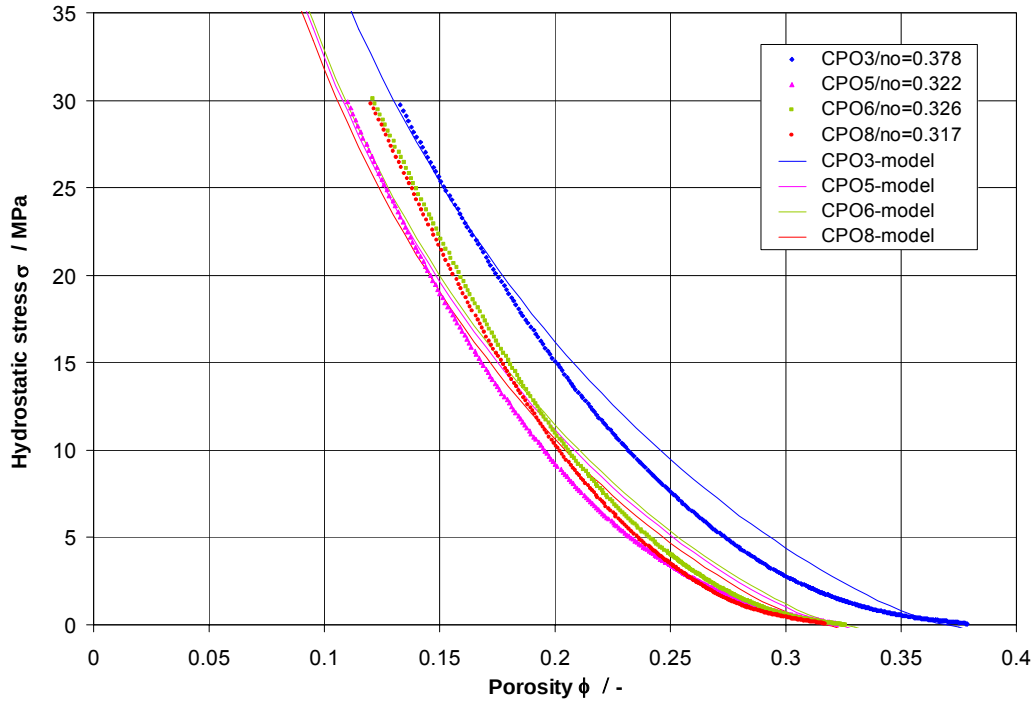

Fig. 4.3.24 Comparison between predicted and measured results from triaxial hydrostatic compaction tests on crushed salt from the DEBORA-tests

- The resulting radial stress observed in the oedometer-like condition is always lower than the axial stress. The radial/axial stress ratio increases linearly with decreasing porosity from about 0.1 for the initial porosity of 0.3 to about 0.38 for the porosity of 0.18 and furthermore towards unity at full compaction with $\phi = 0$. Thus, the resulting mean stress is also a linear function of porosity. Even in the creep consolidation phase at constant axial stress levels, slight increases in radial and mean stress were observed with decreasing porosity.
- Usually, axial stress is assumed as hydrostatic stress in the evaluation of oedometer experiments what might lead to an uncertainty in the prediction of crushed salt consolidation. Approximating hydrostatic stress either by mean stress or by axial stress, however, seems to give the same values for the consolidation parameters n, m, and Q of Zhang's model regarding the dependence of the consolidation rate on stress, porosity, and temperature. By using mean stress as hydrostatic stress in the evaluation, only the parameter A of the model must be determined in triaxial compaction tests.

4.4 Chemical and Mineralogical Properties

4.4.1 Mineralogical Alterations

For the investigation of mineralogical alterations due to heating and compaction, samples were taken from cross sections D1 and A in the heated area (Fig. 4.1.1, cf. Section 4.1). In both sections, three samples (1 to 3) were taken from the heated backfill and two samples (4 to 5) from the rock salt near the drift wall (Fig. 4.4.1). In cross section A, three additional samples (6 to 8) were taken directly from the cask/backfill-interface.

To verify whether a detailed analysis of all samples is justified, preliminary investigations were performed on sample 8 (Fig. 4.4.1) taken from the cask/backfill-interface, a location where the most significant deformation and recrystallization were expected to have occurred. As shown in Figure 4.4.2, specimens were prepared from sample cross sections orientated parallel and perpendicular to the cask surface to examine whether compaction of the crushed salt might have led to changes of the fabric and thus to changes of physical properties, e.g., thermal conductivity or elastic wave velocities.

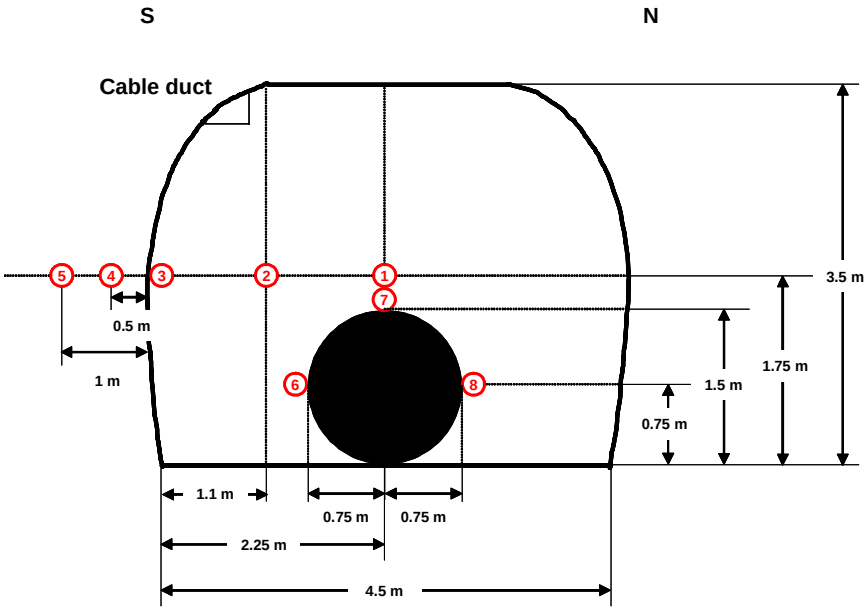

Fig. 4.4.1 Backfill and rock salt sampling locations for chemical and mineralogical analyses in cross sections D1 (samples 1 to 5) and A (samples 1 to 8)

The investigations were performed by the University of Göttingen /LEI 03/ and included microstructural analyses by optical microscopy, Scanning Electron microscopy (SEM), Optical Cathodoluminescence microscopy, and neutron texture analysis on compacted crushed salt cubes (Fig. 4.4.2). Samples and thin sections were prepared in the GRS laboratory.

		VVS-A-NT1	Heater
VVS-A-NT5	VVS-A-NT4	VVS-A-NT2	
		VVS-A-NT3	

Fig. 4.4.2 Sample VVS-A-MI8. a: Identification of specimens. b: Prepared cubes for neutron texture analysis and slices for thin sections

4.4.1.1 Microstructure

Optical microscopy

First, each thin section was digitized with a slide scanner. Then, 70 to 80 single photos were taken under an optical microscope from each thin section. These photos were superimposed to produce one picture (e.g., Fig. 4.4.3). Subsequently, the grain boundaries were recorded digitally (Fig. 4.4.4). Based on these grain boundary maps, important parameters, such as number of grains, grain size distribution, grain shape and porosity, were determined.

Fig. 4.4.3 Microstructure of thin section VVS-A-MI8/NT2

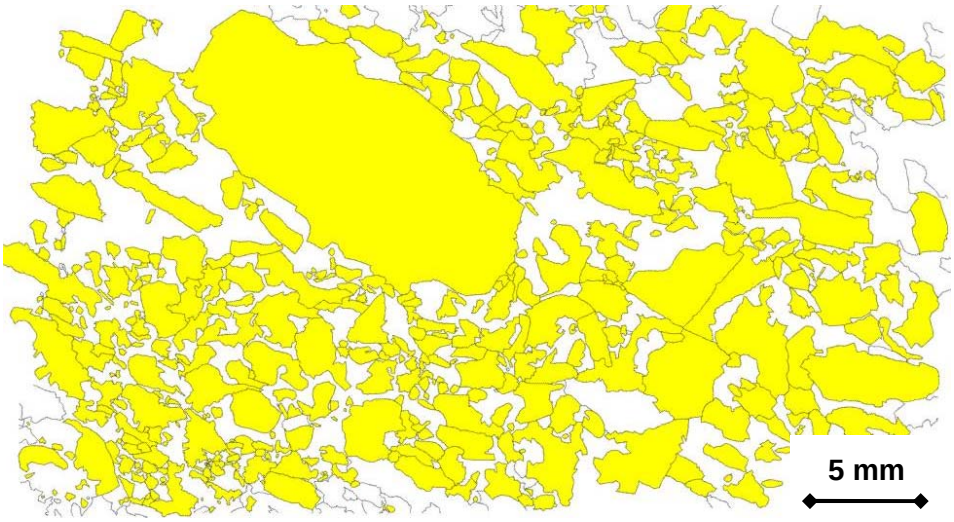

Fig. 4.4.4 Digitized grain boundaries of thin section VVS-A-MI8/NT2

Generally, all samples show a heterogeneous grain size distribution. Coarse crystal (< 5 mm) domains with little white "salt powder" in the space between the grains can be observed. In addition to the coarse grain size domains, domains of moderate and fine grain sizes (about 2 to 5 mm and 1 to 2 mm) can also be observed and often have different portions of white "salt powder" between the grains. In the moderate and coarse grain domains, a single grain orientation appears pervasive. The fabric is dominated by grains between 1 and 5 mm. Occasionally, grains up to 20 mm are found.

The large volume portion of the embedding medium indicates a very high porosity. Plastic deformation or recrystallization of grains is not detectable. Systematic differences between the samples from the profiles parallel and perpendicular to the heater could not be found by using optical microscopy. Therefore, questions remain concerning whether the observed grain size domains originate from the material emplacement process used during backfilling or if they are caused by the compaction process during the heating period. The determination of the porosity from thin sections can be unreliable if preparation procedures disturb the sample.

Scanning electron microscopy (SEM)

Two thin section samples were subjected to scanning electron microscopy (SEM) (1) to increase resolution of the fine-grained areas, (2) to analyse the surface structure of the thin sections for improving the polishing and etching treatments, and (3) to analyse secondary grain boundaries better for determination of grain boundary migration (e.g., /URA 87/) or sintering/compaction processes.

All SEM-photos show a significant difference of embedding material (dark) and salt fabric (bright) (Fig. 4.4.5). In all photos, surface scratches are observed and are attributed to mechanical polishing performing during preparation of the thin sections (Fig. 4.4.6). This phenomenon is the main reason for the reduced sharpness of the salt fabric in optical microscopy because of the diffuse light refraction at the scratches.

Some photos show fractured grains, and the fractures are filled with embedding material. It is not clear if these fractures are a result of mechanical damage induced during drift backfilling, thermal stresses produced during polymerisation of the embedding material, or damage created when thin sections were polished.

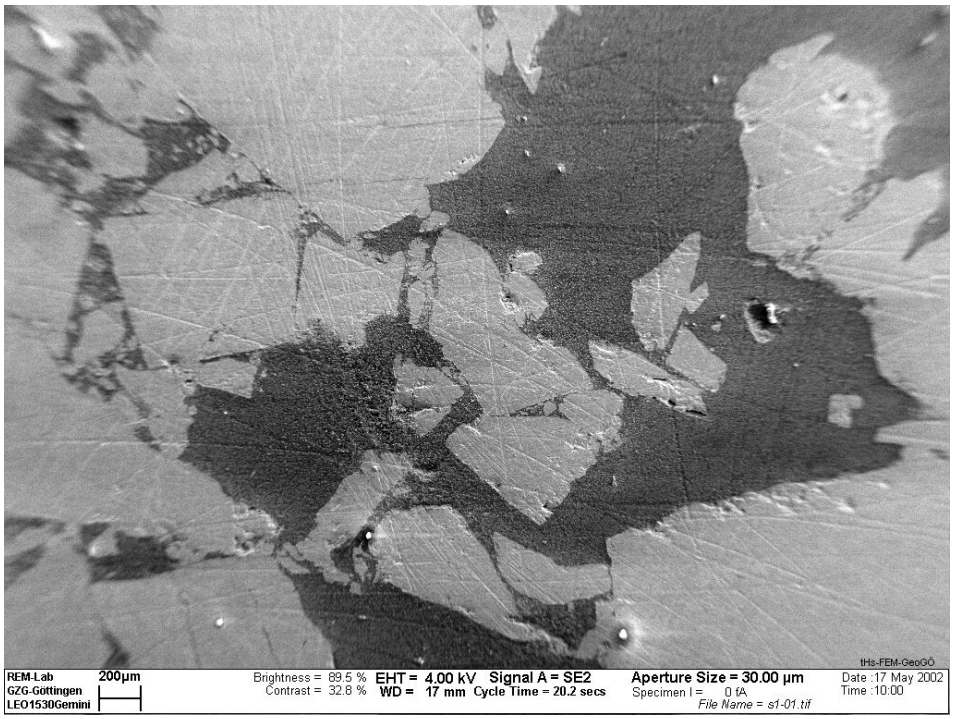

Fig. 4.4.5 Overview of salt fabrics with embedding material of sample VVS-A-MI8/NT1

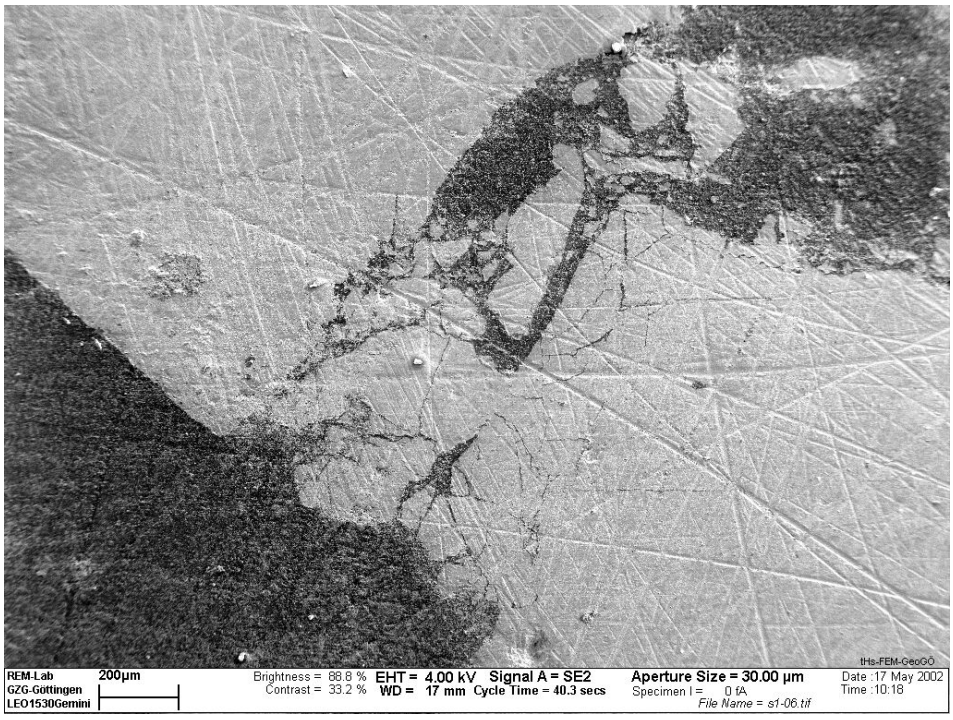

Fig. 4.4.6 Fracture fabrics in and along salt grains; the scratches at the surface are caused by mechanical polishing (sample VVS-A-MI8/NT1)

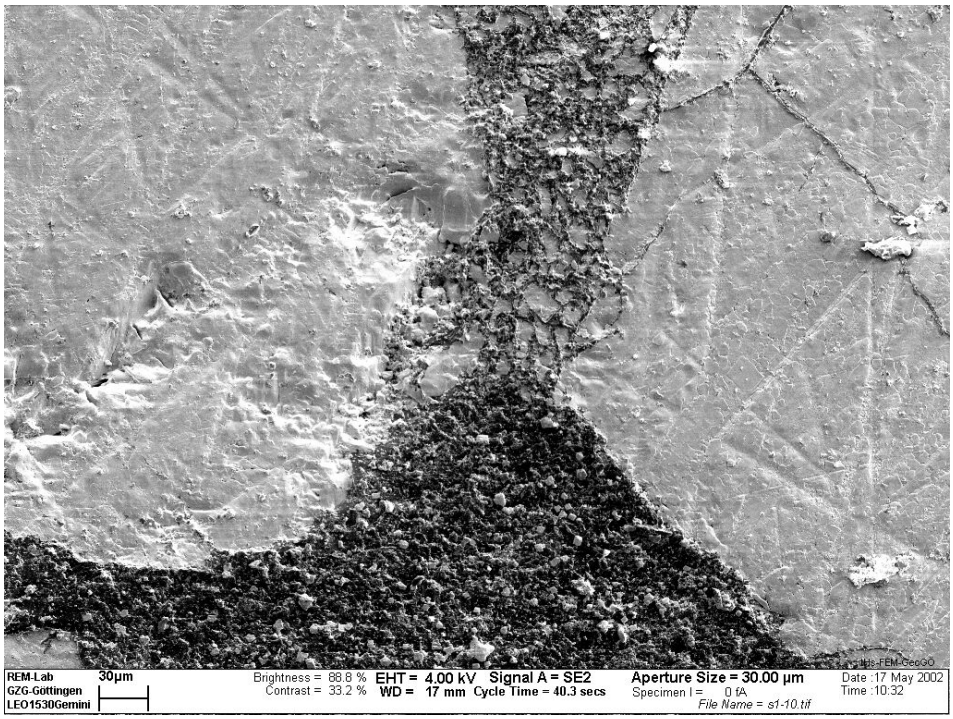

Fig. 4.4.7 Broken salt pieces floating in embedding material (sample VVS-A-MI8/NT1)

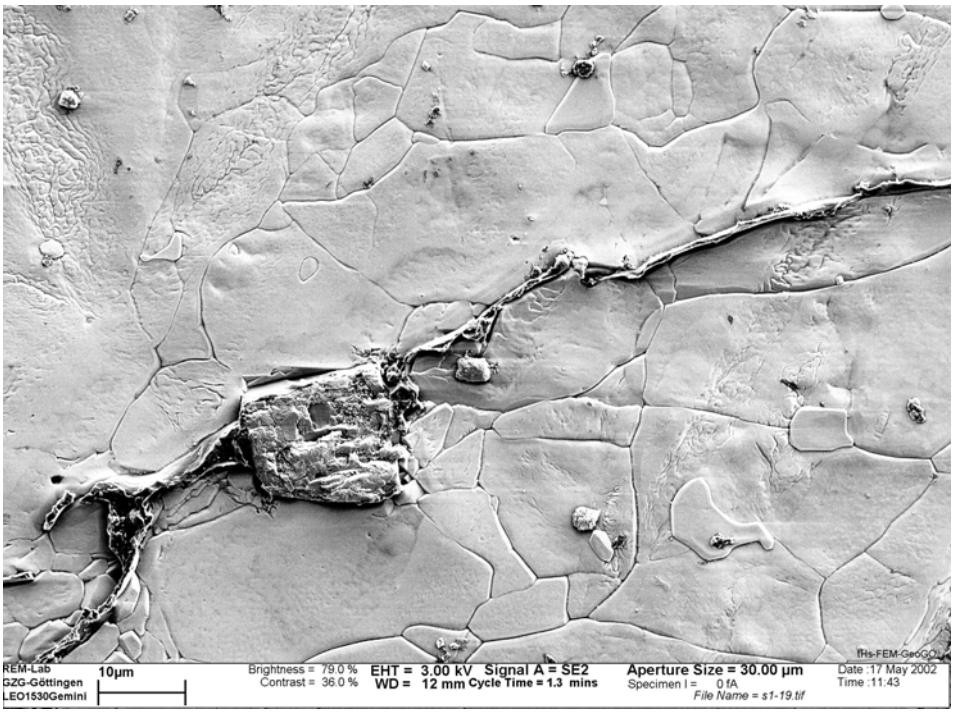

Fig. 4.4.8 Secondary grain boundary sealed with embedding material (sample VVS-A-MI8/NT1)

In some thin sections, broken salt pieces can be seen floating in the embedding material (Fig. 4.4.7). This phenomenon illustrates the difficulties of optical microscopy to identify grain boundaries exactly.

The investigation of secondary grain boundaries is important for the understanding of the sintering/compaction process. Figure 4.4.8 shows distinct subgrain boundaries in two adjacent grains. Obviously, recrystallization did not take place during compaction. Otherwise, migration of grain boundaries from recrystallized grains into adjacent subgrain-rich grains would have been expected.

Even with SEM, no clear evidence of plastic deformation or recrystallization was found. To relate the observed fabrics such as fractures, secondary grain boundaries, and subgrains, which are indications for plastic deformation, to processes like backfilling, sample preparation, and thermal compaction studies would be needed to compare the investigated material with original rock and backfill material.

Optical Cathodoluminescence microscopy

Some trace elements become actively luminescent during electron bombardment. Accordingly, trace element distributions within a crystal are visible under the cathodoluminescence microscope. The cathodoluminescence method (CL) was applied in addition to SEM in order to test its applicability for the investigation of compacted crushed salt fabrics.

In Figure 4.4.9, the salt grains show very intensive bright luminescence under the CL-microscope in contrast to the embedding material which is not luminescent. Therefore, salt and the embedding material can easily be distinguished.

The embedding material changes colour depending on the irradiation duration. This colour change can be seen under the optical microscope (Fig. 4.4.10). In the embedding material and along embedding material/grain-interfaces, open fractures can be observed. Large salt crystals are characterized by dark cleavage fractures.

Generally, the CL-method seems to be a promising method for salt fabric analysis in addition to SEM.

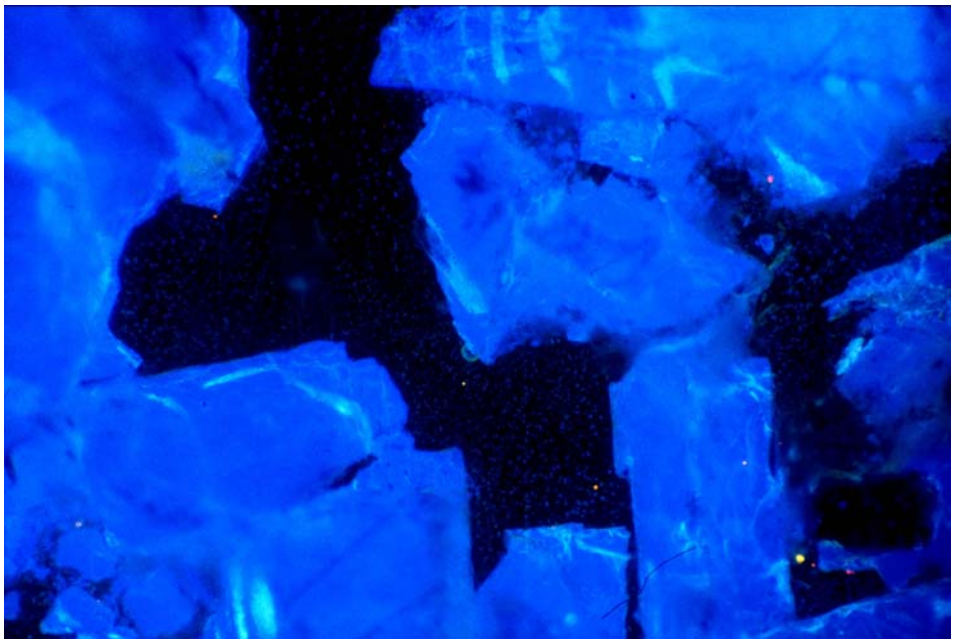

Fig. 4.4.9 Blue luminescent salt and non-luminescent embedding material under the cathodoluminescence microscope (sample VVS-A-MI8/NT1)

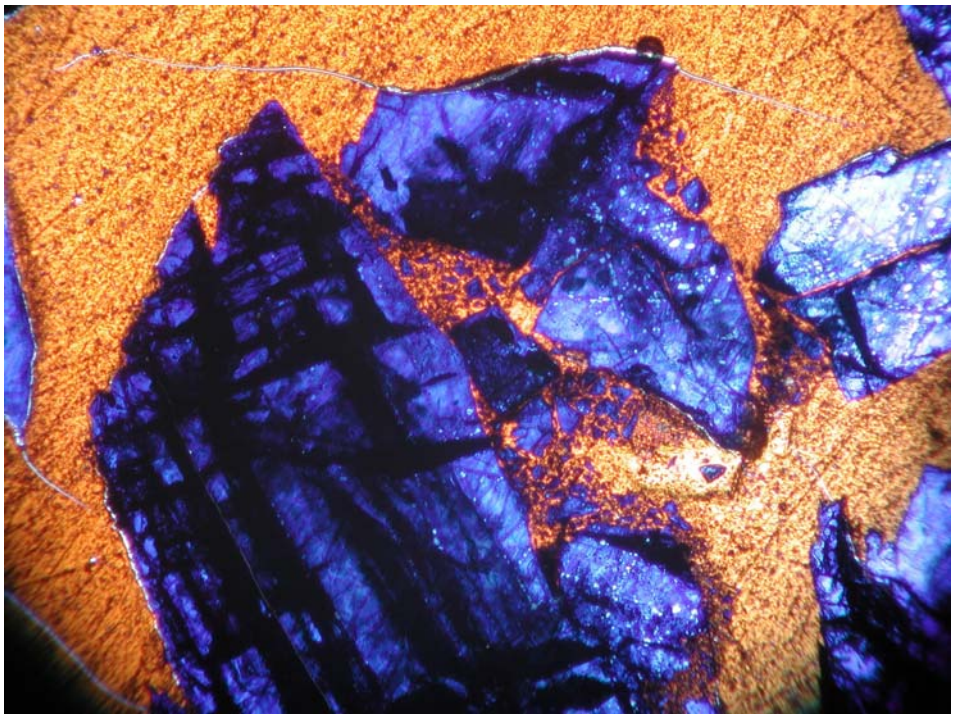

Fig. 4.4.10 Electron-irradiated fabrics under the optical microscope: brown-coloured embedding material and blue salt grains with cleavage fractures in large crystals (sample VVS-A-MI8/NT1)

4.4.1.2 Texture

Crystallographic-preferred orientations can be generated by plastic deformation and recrystallization processes. It was expected that these processes took place during the TSDE experiment and that they could be confirmed by texture analyses. Normally, textures determine the anisotropic physical properties of salt specimens, e.g., the velocities of compression and shear waves (v_p and v_s). The thermal properties, however, are isotropic. Therefore, five specimens were analyzed for crystallographic-preferred orientations. Additionally, the distribution of the compression wave velocities was calculated from the textures.

Neutron texture analysis

Neutron texture analysis was selected as an appropriate method because neutrons show much lower absorption in materials than X-rays. Low absorption is crucial to measure large sample sizes as necessary in the case of the very coarse-grained halite samples.

Respective measurements were conducted with the SKAT texture diffractometer at the research reactor of the Frank Laboratory of Neutron Physics in Dubna/Russia /ULL 98/. To meet the irradiation cross section requirements of 5 x 8.5 cm^2, cubic specimens with an edge length of 5 cm were cut from the compacted crushed salt material (Fig. 4.4.2).

The time-of-flight diagram of specimen VVS-A-MI8/NT2 (Fig. 4.4.11) illustrates the most important BRAGG-reflections of halite (Fig. 4.4.12). In the cubic crystal system, a <h00>-pole figure is normally adequate for a complete description of the texture. With regard to the complex specimen status, however, the <222>-pole figures were evaluated, too, for further verification of the results. The <400>- and <222>-reflections correspond to the cubic and octahedral planes of a halite crystal, respectively.

For all the five specimens, the pole figures in Figure 4.4.13 show intensity distributions which are dominated by single crystal reflections. Except for the smoothed <400>-pole figure of sample NT5, the spatial distributions do not show any preferred orientation. Accordingly, any textural impact on elastic wave velocity is negligible.

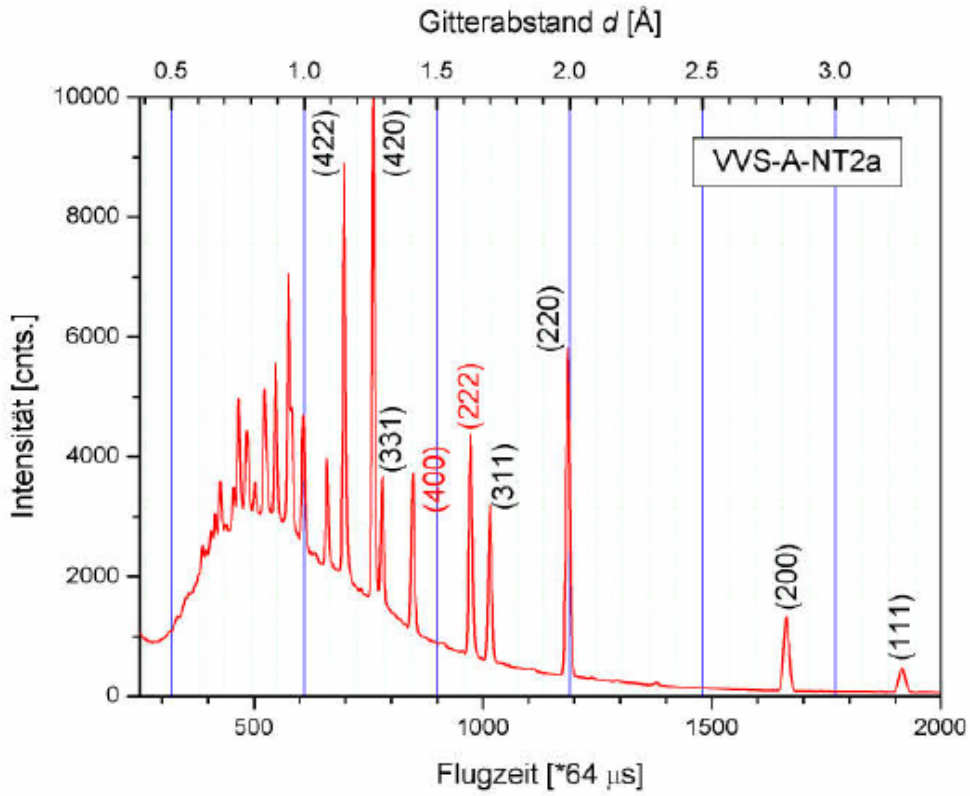

Fig. 4.4.11 Time-of-flight diagram of sample VVS-A-MI8/NT2, cutting plane a; red marked <400>- and <222>-reflections were evaluated with regard to their texture

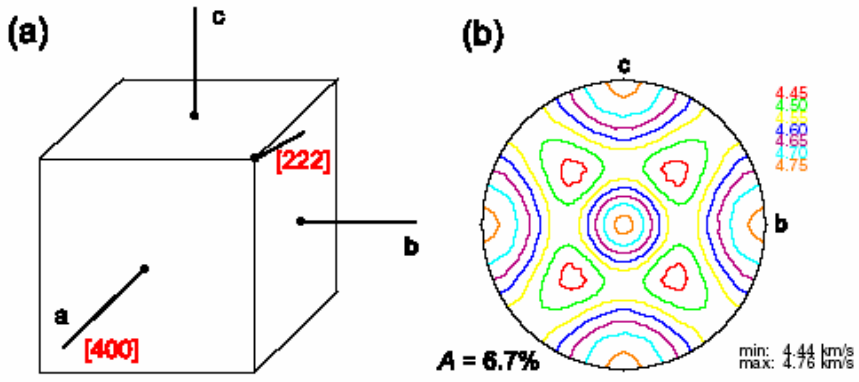

Fig. 4.4.12 a: Crystallography of halite; the evaluated orientations are marked in red. b: Direction dependence of v_p for a halite single crystal (A = Anisotropy)

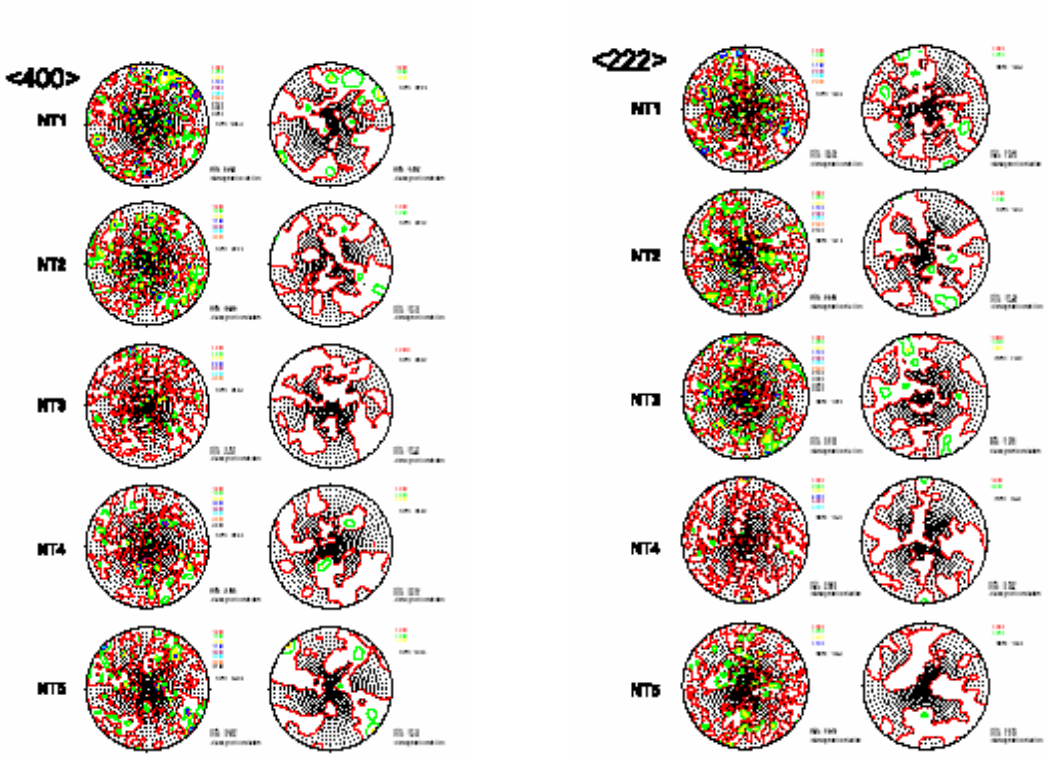

Fig. 4.4.13 Experimental and smoothed pole figures (samples VVS-A-MI8/NT1 to NT5). a: <400>-pole figures. b: <222>-pole figures

In summary, the thermal impact on the material did not lead to the development of any preferred orientation in the primarily randomly distributed lattice orientations. Obviously, the very fine-grained "salt powder" and the large pore space volume cause a strong reduction of grain-grain interfaces so that large migration processes leading to preferred orientations are not possible.

Summary and outlook

The observations and quantifications of microstructures and textures do not confirm the initial assumption of plastic deformation and/or dynamic or static recrystallization of salt grains in the TSDE crushed salt backfill material. Preferred orientations can be seen in some domains, but cannot be confirmed for the whole specimen. A grain-shape-preferred orientation based on the sedimentation process during backfilling cannot be verified.

Recrystallization, as known for solid rock salt, is not to be expected in the investigated crushed salt backfill, because grain-to-grain contacts only exist to a limited extent. Accordingly, grain boundary migration is not very likely.

Investigations must still be conducted into the processes that led to sintering/compaction of the backfill material. However, to conduct these examinations, sample preparation techniques must be improved. A question remains whether the observed grain domains were generated during the backfilling process or if there are domains in which accelerated sintering and compaction took place, i.e., if a sort of nuclei were existing. Furthermore, work is proposed to concentrate on distinct domain characterization and on identifying the time of their development.

Certainly, however, the observed compaction of the crushed salt can simply be explained by the breaking off of salt crystals as a result of the load induced by drift closure.

4.4.2 Residual Water and Gas Content

Residual water and gas contents in the backfill were determined from samples prepared from the large cored samples recovered from boreholes K4, K5, and K6 which had been drilled from cross section I1 (Fig. 4.1.18, cf. Section 4.1.3).

The residual water content of the backfill samples was between 0.03 and 0.05 wt% and exhibited little variability (Tab. 4.4.1). This water content is identical to the average water content of rock salt determined by /JOC 81/.

Tab. 4.4.1 Residual water content in backfill samples / wt%

Sample Identification	Water Content
VVS-I1-K4 feu	0.03
VVS-I1-K5 feu	0.05
VVS-I1-K6 feu	0.04

The residual gas concentrations are shown in Table 4.4.2. The gas content determined from the analyses corresponded more or less to normal mine air. The carbon dioxide content was much lower than the maximum value of almost 1 % observed during the heating phase. Obviously, both hydrogen, which had probably been generated by corrosion of the heater casks, and methane, which had been released from the rock salt during heating, had completely vanished. Both had been observed in concentrations of about 0.75 % and 0.0004 %, respectively, at the end of the heating phase.

Tab. 4.4.2 Residual gas concentration in backfill samples / %

Sample Identification	H_2	O_2	CO	CO_2	CH_4	C_2H_6	C_3H_8
VVS-I1-K4 Gas	n.d.	21.7	b.d.l.	0.0545	b.d.l.	n.d.	n.d.
VVS-I1-K5 Gas	n.d.	21.7	b.d.l.	0.0685	b.d.l.	n.d.	n.d.
VVS-I1-K6 Gas	n.d.	23.3	b.d.l.	0.0700	b.d.l.	n.d.	n.d.

n.d. = not detectable; b.d.l. = below detection limit

5 Instrument Performance and Post-Test Analysis

5.1 Introduction

An extensive instrumentation had been developed to monitor the backfill and rock salt behaviour in the TSDE experiment over time. Instruments had been installed in the backfill and in boreholes in the surrounding rock salt. Originally, the measuring equipment had been designed for a three to five years testing period, but was operated for almost ten years under repository conditions. The geotechnical *in-situ* investigation programme involved temperature, deformation, and stress measurements in the heated and the non-heated area. The different instruments, their specifications, and their performance during the experiment are summarized in Table 5.1.

About 85 % of the temperature gauges operated well until the end of the *in-situ* measurements. Most failures were caused by damaged measuring cables. Due to the large number of redundantly installed thermometers, failures of temperature gauges were negligible.

Regarding the deformation gauges, the harsh environment resulted in a significant number of failures during the heating period. Most failures were caused by damaged measuring cables. The gauge design itself, however, proved to be very robust. Failures of horizontal drift convergence measuring devices and extensometers in the heated area could only be remedied by replacement measures. Therefore, more redundant systems for these important instrument types are strongly recommended. An investigation of the damaged measuring cables revealed that failures were caused by compression of the multicore cables, which short-circuited or broke cores and allowed electrolyte intrusion into the cables. Therefore, the multicore cable design cannot be recommended for *in-situ* measurements in the heated area as a single point of damage will gradually compromise all gauges connected to the same multicore cable.

For backfill pressure measurements at the interfaces between backfill and rock, the robust Glötzl hydraulic pressure cells are very recommendable. About 30 % of the pressure gauges failed during the *in-situ* test, but most failures were caused by damaged hydraulic measuring lines. For the observation of long-term stress changes in the rock, stress monitoring probes had been installed in boreholes, which also consisted of Glötzl hydraulic pressure cells. These stress probes were considerably

affected by accelerated rock deformation after the start of heating which led to a large number of failures attributed to damages at the pressure cells. Because the several pressure cells of each stress monitoring probe had been equipped with common return lines, neither detailed investigations of failed gauges nor continuation of the measurements in case of damaged pressure lines were possible. Therefore, the common use of return lines for several gauges should be avoided. Separate return lines are strongly recommended. With the electropneumatic pressure cells of the AWID type, which had been used at the interfaces between backfill and heater cask surface, no useful results were obtained. Almost all AWID measuring systems failed soon after the beginning of heating probably due to damaged measuring lines.

From the gas sampling systems which consisted of gas sampling filters and Teflon tubes, satisfactory results were obtained from most sampling points.

During the experiment, measurements were made remotely and no inspection and maintenance of the instruments were possible. Because similar instruments will likely be used for repository monitoring, instrument accuracy and reliability are significant features in repository design. Therefore, all instruments in drift B, which had been located in the backfill and at the surface of the heater casks, were recovered during the excavation phase for post-test analyses. Instruments were retrieved from the cross sections L1, E1, $E1^{+1}$, I1, $D1^{-1}$, D1, F1, G1, H1, B, B^{+1}, A, C, and $G2^{-0.75}$ comprising temperature gauges, convergence measuring devices, backfill settling measuring devices, extensometer transducers, hydraulic pressure cells, AWID gauges and gas sampling filters. A representative number of measuring gauges was selected for further investigations and re-calibration.

The selected temperature gauges were shipped to their manufacturer Heraeus Sensor GmbH (since 2001: Rosemount Temperature GmbH) which is holding an authorized laboratory of the German Calibration Service (Deutscher Kalibrierdienst DKD). The selected sensors of the convergence measuring devices, of the backfill settling measuring devices, and of the extensometers as well as the hydraulic pressure cells, the AWID gauges and the gas sampling filters were shipped to their manufacturer Glötzl Gesellschaft für Baumeßtechnik mbH. The post-test analyses, which were carried out on the recovered measuring equipment, are summarized in Table 5.1, too.

Tab. 5.1 Instruments of *in-situ* measurements and their performance

Process/ Parameter	Instrument or Method	Location in Experiment	Operating Range	Accuracy	Datalogging	Performance
Temperature	Resistance temperature detectors of the type PT100	Lower temperature locations in rock (boreholes) and backfill	From 0°C to 80°C	±0.01°C at 0°C, ±0.07°C at 100°C Limit of tolerance (Class B-sensors): ±0.3°C at 0°C, ±0.8°C at 100°C	Local front end processor - GSSE logger	164 of 215 sensors operated well until the end of the experiment corresponding to 24 % failures. Most failures were caused by damaged measuring cables. Re-calibration of retrieved sensors revealed their high reliability. After nearly 12 years of operation, deviations were still within the limit of tolerance. At 0°C and 100°C, re-calibration results in 2002 were almost identical with original calibration in 1990. Cable protection and cable duct design have to be improved.
		Heater cask surface and high temperature locations in the backfill	From 0°C to 250°C	±0.01°C at 0°C, ±0.07°C at 100°C, ±0.15°C at 250°C Limit of tolerance (Class B-sensors): ±0.3°C at 0°C, ±0.8°C at 100°C, ±1.55°C at 250°C	Local front end processor - GSSE logger	520 of 582 sensors operated well until the end of the experiment corresponding to 10 % failures. Most failures were caused by damaged measuring cables. Re-calibration of retrieved sensors revealed their high reliability. After nearly 12 years of operation, deviations were still within the limit of tolerance. Cable protection and cable duct design have to be improved.
Drift Closure	Stationary measuring equipment of the type Glötzl SSKE 400 with displacement transducers of the type Glötzl GWD 35/400	Backfilled drifts: Measuring rods installed horizontally and vertically between opposite drift surfaces. Perimeter changes measured by Glötzl displacement transducers. Protection against mechanical impact by telescopic steel tubes.	Opening dimensions: ≤ 4.5 m. Up to 180°C. Transducer: Measuring range 400 mm, up to 125°C.	Transducer: Linearity <±0.2 % (related to the total measuring range), Resolution 0.01 mm.	Local front end processor - GSSE logger	Gauge design successful, few transducer failures. Harsh environment application with pressure and moisture impact on cables resulted in failure of 9 of 22 devices during the test. Re-calibration of retrieved transducers revealed their reliability. After nearly 12 years of operation at temperatures of up to 90°C, their linearity was largely within the limit of tolerance. Deviations from the original calibration were only observed for the gauges which had been installed directly above the heater casks. The measuring rods of these devices, however, had been bent significantly. Cable protection and cable duct design to be improved.

Continuation of Tab. 5.1

Process/ Parameter	Instrument or Method	Location in Experiment	Operating Range	Accuracy	Datalogging	Performance
Backfill Settling	Stationary measuring equipment of the type Glötzl SSME with displacement transducers of the type Glötzl GWD 35/400 and GWD 35/250	Backfilled drifts: With each measuring equipment, 3 measuring rods and 3 anchor plates installed vertically in the drifts for monitoring the distribution of backfill settling at three different levels. Distance changes measured by Glötzl displacement transducers. Protection against mechanical impact by telescopic steel tubes.	Dimensions: ≤ 3.5 m. Up to 180°C. Transducer: Measuring ranges 250 mm and 400 mm, up to 125°C.	Transducer: Linearity <±0.2 % (related to the total measuring range), Resolution 0.01 mm.	Local front end processor - GSSE logger	Gauge design successful and only few transducer failures. Harsh environment application with pressure and moisture impact on cables resulted in failure of 11 of 30 devices during the test. Re-calibration of retrieved transducers revealed their reliability. After nearly 12 years of operation at temperatures of up to 90°C, their linearity was largely within the limit of tolerance. Cable protection and cable duct design have to be improved.
Rock Displace-ment	Multi-point extensometer of the type Glötzl GKSE 16 with displacement transducers of the type Glötzl GWW 50/50	Boreholes in rock: Anchors fixed by grouting, with glass fibre rods from each anchor to the instrument head at the borehole collar. Rod movement measured with Glötzl displacement transducers at the instrument head. One-dimensional axial displacement of each anchor relative to the instrument head at the borehole collar.	Borehole diameter: 131 / 180 mm. Treansducer: Measuring range ±50 mm, up to 70°C.	Extensometer: 0.02 mm up to 20 m length, 0.1 mm up to 50 m lenghth, 0.3 mm up to 100 m length. Transducer: Linearity <±0.5 % (related to the total measuring range), Resolution 0.025 mm.	Local front end processor - GSSE logger	Gauge design successful: All 18 extensometers operated well during nearly 12 years of operation. Few transducer failures could be repaired during the experiment. Re-calibration of retrieved transducers, which had been operated at a lower temperature of 33.5°C, revealed their reliability. 14 years after the original calibration, their linearity was almost identical.
	Multi-point extensometer of the type Glötzl TEX 16 with displacement transducers of the type Glötzl GWD 35/400, GWD 35/250, GWD 35/100 and GWW 100 l	Boreholes in rock: Anchors fixed by wedging, with glass fibre rods from each anchor to the instrument head in the deepest part of the borehole. Rod movement measured with Glötzl displacement transducers at the instrument head. Cables running to the borehole collar. One-dimensional axial displacement of each anchor relative to the instrument head in the deepest part of the borehole.	Borehole diameter: 180 mm. Transducer: Measuring ranges 100 mm, 250 mm, 400 mm, up to 125°C.	Extensometer: 0.02 mm up to 20 m length, 0.1 mm up to 50 m lenghth, 0.3 mm up to 100 m length. Transducer: Linearity <±0.2 % (related to the total measuring range), Resolution 0.01 mm.	Local front end processor - GSSE logger	Gauge design successful and only few transducer failures. Harsh environment application with pressure and moisture impact on the used multicore cables resulted in failure of 69 of 112 extensometers during the test. Re-calibration of recovered transducers revealed their reliability. However, sensors could only be retrieved from replaced extensometers, which had been in operation for up to 7 years at an ambient temperature of 36°C. Their linearity was almost identical with the original calibration. Cable protection and cable duct design have to be improved. Multicore cables are not recommendable.

Continuation of Tab. 5.1

Process/ Parameter	Instrument or Method	Location in Experiment	Operating Range	Accuracy	Datalogging	Performance
Rock Displace-ment	Inclinometer - mobile probe of the type Glötzl NMG 30/2	Boreholes in rock equipped with access guide tubes, measurements with a mobile probe. Two-dimensional radial displacement perpendicular to borehole axis.	Borehole diameter: ≤ 180 mm. Up to 80°C.	Probe: 0.02 mm per m measuring depth, Measuring system: 0.1 mm per m measuring depth	Mobile probe readings	Good system performance with no failure of access guide tubes, but measurements very labour intensive. Several re-calibrations of the mobile probe during the experiment.
Backfill Pressure	Hydraulic pressure cells of the type Glötzl F 20/30 QS 400 A Z4	Interfaces between backfill and rock, embedded in concrete. Hydraulic lines required to monitor the cells. Oil is pumped into a measuring line and pressure is built up against the diaphragm of the pressure cell until equilibrium with the surrounding backfill pressure is reached. At this pressure, which corresponds to the backfill pressure, the diaphragm opens and the oil turns back via the return line. Determination of long-term stress changes.	Up to 40 MPa.	±0.02 MPa Linearity <±0.5 % (related to the total measuring range)	Local front end processor - Glötzl MFA logger	Pressure cells performed well. 14 of 44 gauges failed until the end of the experiment, but most failures could be attributed to damages at the hydraulic measuring lines. Autoclave re-calibration of retrieved pressure cells revealed their reliability. For the unstressed cells, deviations from initial pressurization were low. After nearly 12 years of operation at temperatures of up to 125°C, their linearity was largely within the limit of tolerance. Measuring line protection and cable duct design have to be improved.
	Electropneumatic pressure cells of the AWID type	Interfaces between backfill and heater cask surface, embedded in saltcrete. Pneumatic lines and electric cables required to monitor the cells. Air is pumped into the pressure cell until equilibrium with the surrounding backfill pressure is reached. At this pressure, which corresponds to the backfill pressure, the cell opens and its resistance increases distinctly. The resistance is determined during the measurement by injecting a constant electric current and measuring the voltage over the cell. Determination of long-term stress changes.	Up to 60 MPa. Up to 250°C (measurements independent from temperature).	<0.3 % at 15 MPa	Local front end processor - Glötzl MFA logger	No useful results were obtained. Almost all measuring systems failed shortly after the beginning of heating due to damaged pneumatic and/or electric measuring lines. Therefore, the whole measuring unit was shut down early. Post-test investigation of retrieved AWID cells confirmed that the gauges were still tight and functioning completely. Measuring line protection and cable duct design have to be improved. Due to its intricate measuring equipment only recommendable for special application.

Continuation of Tab. 5.1

Process/ Parameter	Instrument or Method	Location in Experiment	Operating Range	Accuracy	Datalogging	Performance
In situ Rock Stress	Stress monitoring probes consisting of several hydraulic pressure cells of the type Glötzl BB 10/20 QS 400 with various orientation	Grouted into boreholes in rock: Hydraulic lines required to monitor the cells. Oil is pumped into a measuring line and pressure is built up against the diaphragm of the pressure cell until equilibrium with the surrounding rock pressure is reached. At this pressure, which corresponds to the rock stress, the diaphragm opens and the oil turns back via the return line. Hydraulic measuring lines running to the borehole collar. Determination of long-term stress changes.	Borehole diameter: 180 mm. Up to 40 MPa.	±0.02 MPa Linearity <±0.5 % (related to the total measuring range)	Local front end processor - Glötzl MFA logger	47 of 49 gauges failed during the test. 35 gauges were replaced from which 8 failed until the end of the experiment. Most failures were caused by damages at the pressure cells due to accelerated rock deformation. Only 15 % of the failures could be attributed to the hydraulic measuring lines. The use of common return lines by several gauges is not recommendable.
Gas Monitoring	Permeable filters for gas sampling for various analyses (gas chromatography, humidity)	Backfilled drifts: Glass filters at the heater cask surface as well as at the drift roof and floor. A membrane pump was used to transfer gas from the filters via Teflon tubes to the drift entrance for collection.	Filter porosity: 42.5 % Filter permeability: $2 \cdot 10^{-9}$ m² Allowing both gas and moisture sampling.	100 ml Gas required for gas chromatography	Sampling of approx. 1 l Gas in Linde gas sampling bags	Satisfactory results were obtained from most sampling points. 17 of 28 sampling points operated well until the end of the experiment. Post-test investigation of retrieved filters revealed that these filters were not plugged and still permeable. Hence, the failures of sampling points, which had to be shut down during the experiment, were caused by damages at the Teflon tubes. Tube protection and cable duct design have to be improved.

5.2 Temperature Gauges

Temperatures had been recorded by nearly 800 resistance thermometers at the surface of the heater casks, in the backfill, and in the surrounding rock salt (Fig. 5.2.1). The sensors consisted of a temperature dependent platinum resistor PT 100 with a nominal resistance of 100 Ω at a temperature of 0 °C. In order to compensate for temperature influence on cable resistance, the sensors were fabricated in four-wire technique. The sensor measuring range was from 0 °C to +80 °C in lower temperature locations within the rock and backfill, and from 0 °C to +250 °C on the heater cask surface and within high temperature locations in the backfill.

Fig. 5.2.1 Temperature gauge *in situ* with the PT 100 sensor at the drift wall and the measuring cable in the cable slot (cross section I1)

Tab. 5.2 Retrieved temperature gauges from the southern test drift (cross section L1)

MCS	Position	Gauge Identification	Original Calibration No.	Maximum Temperature in situ	Status before Retrieval	Re-Calibration No.	Re-Calibration 0°C	Re-Calibration 100°C	Re-Calibration 250°C	Evaluation
L1	wall	EL L1 AST T11 18	DKD - 86	approx. 40°C	ok.	-	-	-	-	-
		EL L1 AST T12 18	DKD - 58	approx. 40°C	ok.	DKD - 003	yes	yes	-	gauge ok.
		EL L1 AST T13 18	DKD - 83	approx. 40°C	ok.	-	-	-	-	-
		EL L1 AST T14 18	DKD - 84	approx. 40°C	ok.	DKD - 006	yes	yes	-	gauge ok.
		EL L1 AST T15 18	DKD - 85	approx. 40°C	ok.	-	-	-	-	-
		EL L1 AST T21 18	DKD - 72	approx. 40°C	ok.	-	-	-	-	-
		EL L1 AST T22 18	DKD - 73	approx. 40°C	ok.	-	-	-	-	-
		EL L1 AST T31 18	DKD - 78	approx. 40°C	ok.	DKD - 002	yes	yes	-	gauge ok.
		EL L1 AST T32 18	DKD - 80	approx. 40°C	ok.	-	-	-	-	-
		EL L1 AST T33 18	DKD - 81	approx. 40°C	ok.	-	-	-	-	-
		EL L1 AST T34 18	DKD - 79	approx. 40°C	ok.	-	-	-	-	-
		EL L1 AST T35 18	DKD - 82	approx. 40°C	ok.	-	-	-	-	-
		EL L1 AST T41 18	DKD -71	approx. 40°C	ok.	-	-	-	-	-
		EL L1 AST T42 18	DKD - 69	approx. 40°C	ok.	-	-	-	-	-
		EL L1 AST T43 18	DKD - 70	approx. 40°C	ok.	-	-	-	-	-
	pillar	EL L1 AST T51 18	DKD - 55	approx. 40°C	ok.	DKD - 005	yes	yes	-	gauge ok.
		EL L1 AST T52 18	DKD - 56	approx. 40°C	ok.	-	-	-	-	-
		EL L1 AST T53 18	DKD - 57	approx. 40°C	ok.	-	-	-	-	-
		EL L1 AST T54 18	DKD - 59	approx. 40°C	ok.	-	-	-	-	-
		EL L1 AST T55 18	DKD - 60	approx. 40°C	ok.	-	-	-	-	-
		EL L1 AST T56 18	DKD - 61	approx. 40°C	ok.	-	-	-	-	-
		EL L1 AST T61 18	DKD - 62	approx. 40°C	ok.	-	-	-	-	-
		EL L1 AST T62 18	DKD - 63	approx. 40°C	ok.	-	-	-	-	-
		EL L1 AST T63 18	DKD - 64	approx. 40°C	ok.	-	-	-	-	-
		EL L1 AST T64 18	DKD - 65	approx. 40°C	ok.	DKD - 001	yes	yes	-	gauge ok.
		EL L1 AST T65 18	DKD - 66	approx. 40°C	ok.	-	-	-	-	-
		EL L1 AST T66 18	DKD - 67	approx. 40°C	ok.	-	-	-	-	-
		EL L1 AST T71 18	DKD - 75	approx. 40°C	ok.	DKD - 004	yes	yes	-	gauge ok.
		EL L1 AST T72 18	DKD - 76	approx. 40°C	ok.	-	-	-	-	-
		EL L1 AST T73 18	DKD - 77	approx. 40°C	ok.	-	-	-	-	-

Prior to heating, a representative number of 60 temperature sensors had been calibrated by an authorized laboratory of the German Calibration Service (Deutscher Kalibrierdienst DKD) at the manufacturer (Heraeus) in February 1990. But all these calibrated gauges had been installed in the southern test drift. Only a number of 30 gauges was accessible near the drift entrance in cross section L1. These gauges were retrieved from the backfill (Tab. 5.2).

Tab. 5.3 Retrieved temperature gauges from the northern test drift

MCS	Position	Gauge Identification	Original Calibration No.	Maximum Temperature in situ	Status before Retrieval	Re-Calibration No.	Re-Calibration 0°C	Re-Calibration 100°C	Re-Calibration 250°C	Evaluation
$E1^{+1}$	1.10 m (middle)	EL E1 194 T1 011	-	49.3°C	ok.	-	-	-	-	-
	2.20 m (middle)	EL E1 194 T2 022	-	48.6°C	ok.	-	-	-	-	-
	3.50 m (middle)	EL E1 194 T3 035	-	48.8°C	ok.	-	-	-	-	-
I1	cask surface (right)	EL I1 BBH T1 008	-	191.5°C	ok.	-	-	-	-	-
	cask surface (top)	EL I1 BBH T2 015	-	191.2°C	ok.	-	-	-	-	-
	cask surface (left)	EL I1 BBH T3 008	-	173.6°C	ok.	-	-	-	-	-
	floor (wall side)	EL I1 BST T1 000	-	87.2°C	ok.	-	-	-	-	-
	floor (pillar side)	EL I1 BST T2 000	-	89.4°C	ok.	-	-	-	-	-
	pillar	EL I1 BST T3 018	-	86.8°C	ok.	-	-	-	-	-
	roof	EL I1 BST T4 035	-	78.3°C	ok.	-	-	-	-	-
	wall	EL I1 BST T5 018	-	81.2°C	ok.	-	-	-	-	-
$D1^{-1}$	floor (pillar side)	EL D1 181 T1 000	-	121.3°C	ok.	DKD-019	-	yes	yes	gauge ok.
	1.80 m (pillar side)	EL D1 181 T2 018	-	129.3°C	ok.	DKD-017	-	yes	yes	gauge ok.
	3.50 m (pillar side)	EL D1 181 T3 035	-	84.3°C	ok.	DKD-010	yes	yes	-	gauge ok.
	horizontal 1.80 m	EL D1 099 T1 018	-	91.8°C	ok.	DKD-012	yes	yes	-	gauge ok.
D1	cask surface (left)	EL D1 BBH T1 008	-	193.6°C	ok.	-	-	-	-	-
	cask surface (top)	EL D1 BBH T2 015	-	206.4°C	ok.	-	-	-	-	-
	cask surface (right)	EL D1 BBH T3 008	-	203.4°C	ok.	-	-	-	-	-
F1	floor (wall side)	EL F1 BST T1 000	-	94.5°C	failed		-	-	-	gauge failure
G1	horizontal 1.80 m	EL G1 168 T1 018	-	93.1°C	ok.	DKD-009	yes	yes	-	gauge ok.
	vertical (wall side)	EL G1 171 T2 000	-	85.6°C	ok.	DKD-008	yes	yes	-	gauge ok.
H1	cask surface (right)	EL H1 BBH T1 008	-	199.4°C	ok.	-	-	-	-	-
	cask surface (top)	EL H1 BBH T2 015	-	198.9°C	ok.	-	-	-	-	-
	cask surface (left)	EL H1 BBH T3 008	-	197.4°C	ok.	-	-	-	-	-
	wall	EL H1 BST T5 018	-	95.1°C	ok.	-	-	-	-	-
B	wall	EL B0 BST T3 018	-	96.1°C	ok.	-	-	-	-	-
	roof	EL B0 BST T4 035	-	92.9°C	ok.	-	-	-	-	-
	pillar	EL B0 BST T5 018	-	100.7°C	ok.	-	-	-	-	-
B^{+1}	floor (pillar side)	EL B0 142 T1 000	-	128.4°C	ok.	DKD-016	-	yes	yes	gauge ok.
	1.80 m (pillar side)	EL B0 142 T2 018	-	134.0°C	ok.	DKD-018	-	yes	yes	gauge ok.
	3.50 m (pillar side)	EL B0 142 T3 035	-	96.5°C	ok.	DKD-007	yes	yes	-	gauge ok.
	horizontal 1.80 m	EL B0 176 T1 018	-	102.0°C	ok.	DKD-011	yes	yes	-	gauge ok.
A	cask surface (left)	EL A0 BBH T1 008	-	209.3°C	ok.	DKD-013	-	yes	not possible	gauge ok.
	cask surface (top)	EL A0 BBH T2 015	-	209.8°C	ok.	DKD-014	-	yes	not possible	gauge ok.
	cask surface (right)	EL A0 BBH T3 008	-	194.9°C	ok.	DKD-015	-	yes	yes	gauge ok.
	roof	EL A0 BST T4 035	-	95.8°C	ok.	-	-	-	-	-
H2	cask surface (right)	EL H2 BBH T1 008	-	190.7°C	ok.	-	-	-	-	-
	cask surface (top)	EL H2 BBH T2 015	-	192.4°C	ok.	-	-	-	-	-
	cask surface (left)	EL H2 BBH T3 008	-	158.9°C	ok.	-	-	-	-	-
	floor (wall side)	EL H2 BST T1 000	-	92.7°C	failed		-	-	-	gauge failure

During drift excavation, 40 temperature gauges were retrieved from the northern test drift (Tab. 5.3). However, none of these gauges had been calibrated prior to heating. Almost all recovered gauges had been functioning until the end of the *in-situ* measurements. Only one gauge had failed probably due to a sensor defect (cross section F1). Another failure had presumably been caused by cable damage (cross section H2). The failure reasons were checked with the post-test investigations.

From the recovered temperature gauges, representative sensors were selected for re-calibration (Tab. 5.2 and 5.3). The calibration work was carried out by the same laboratory of the German Calibration Service (DKD). Depending on their maximum temperature value *in situ*, two calibration points were chosen for each sensor. Up to a maximum *in-situ* temperature of approximately 100 °C, the calibration points were 0 °C and 100 °C. Five sensors which had measured higher temperatures were calibrated at 100 °C and 250 °C. Actually, the two sensors DKD-13 and DKD-14 should be calibrated at 250 °C, too, but their remaining cable length was too short to fit into the calibration oven.

For each calibration point, the deviation from the DIN EN 60751-value was determined. The deviations are shown in Figures 5.2.2 to 5.2.4 together with their accuracy. The re-calibrations were carried out with an accuracy of ±0.05 °K at 0 °C, ±0.1 °K at 100 °C, and ±0.15 °K at 250 °C which is very adequate for industrial sensors. The original calibration accuracy at 0 °C (±0.01 °K) and at 100 °C (±0.07 °K) was higher, but only reasonable for the first calibration. After their *in-situ* utilization, this high calibration accuracy was not necessary for the recovered sensors.

The re-calibration results showed the high reliability of the temperature sensors after almost 12 years of operation as the deviations from DIN EN 60751 were still very low (Fig. 5.2.2 to 5.2.4). Almost all sensor deviations were still within the limits of tolerance. These limits of tolerance for the used class B-sensors are ±0.3 °K at 0 °C, ±0.8 °K at 100 °C, and ±1.55 °K at 250 °C. Only one sensor (DKD-8) was beyond the limit, but at the calibration temperature of 0 °C. At the calibration point 100 °C, however, which almost corresponded to its maximum *in-situ* temperature, this gauge was within the limit, too. From the comparison of the calibrations in 1990 and in 2002, a low sensor drift was derived at least for the gauges in cross section L1, as the re-calibration results at 0 °C and 100 °C were almost identical with the original calibration (Fig. 5.2.2 and 5.2.3).

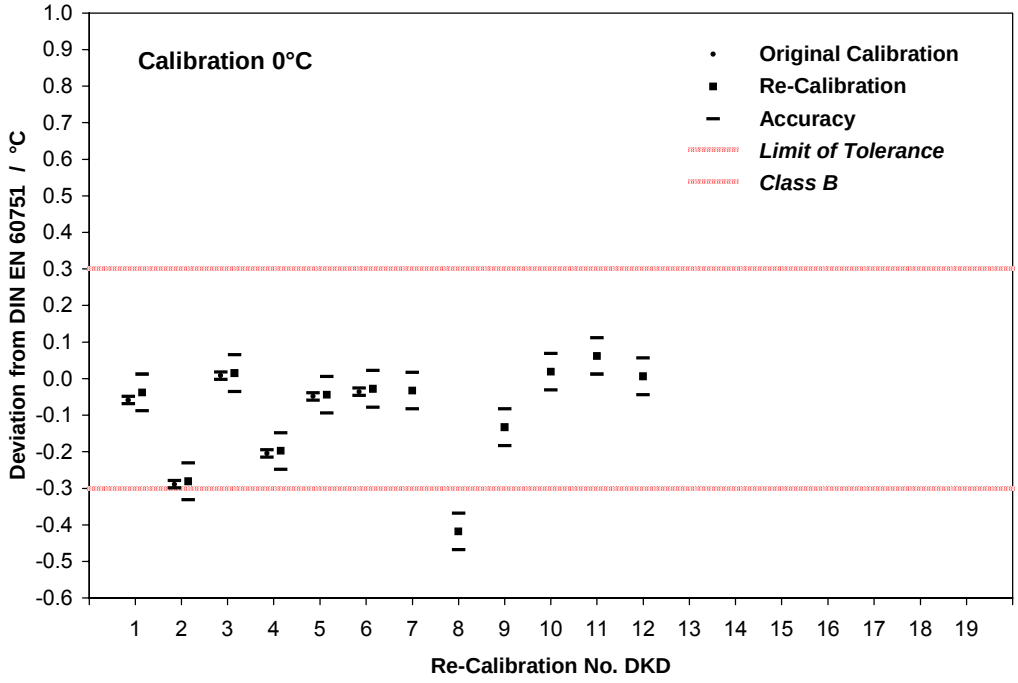

Fig. 5.2.2 Calibration of temperature gauges at 0 °C

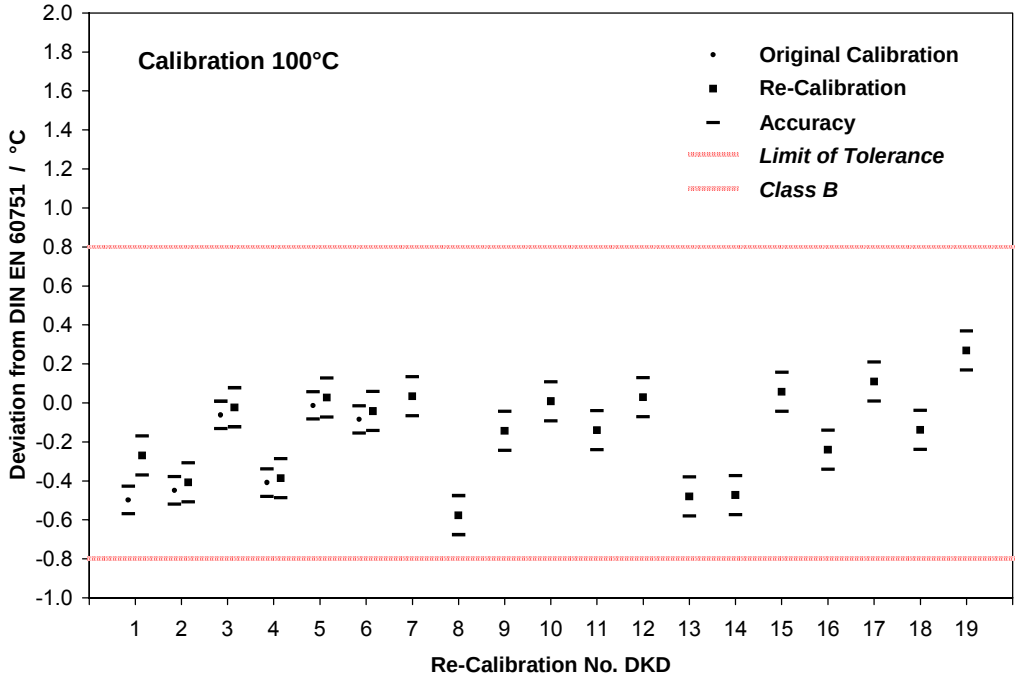

Fig. 5.2.3 Calibration of temperature gauges at 100 °C

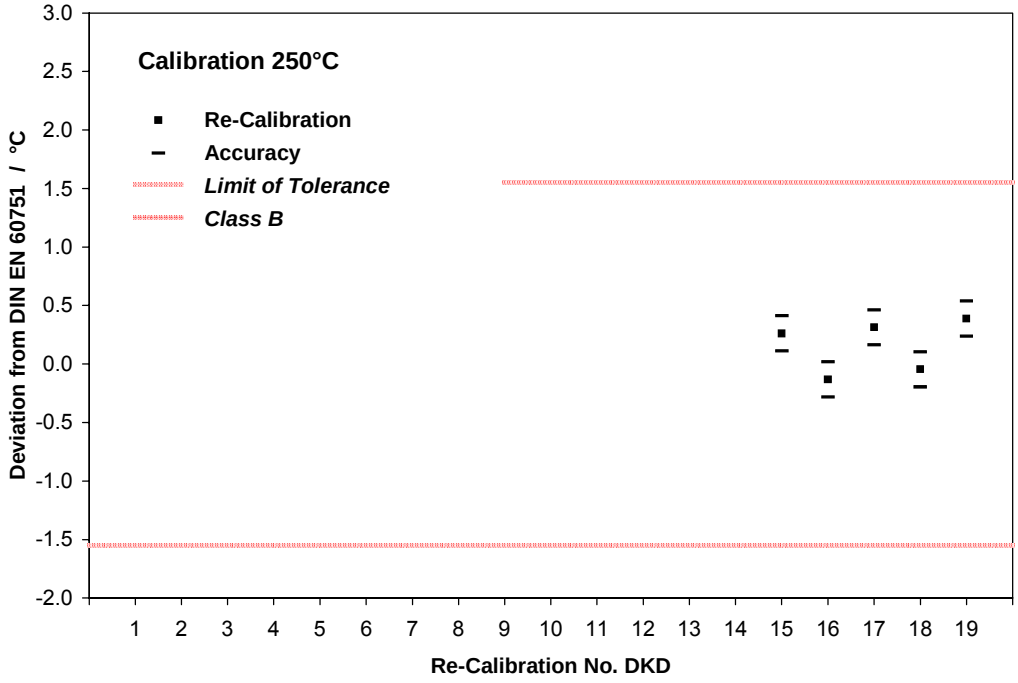

Fig. 5.2.4 Calibration of temperature gauges at 250 °C

X-ray examination of the two failed temperature gauges confirmed that the sensor from cross section F1 had failed due to a gauge defect. The sensor is shown in the Figures 5.2.5 and 5.2.6. The X-ray picture reveals that the ceramic body, which is the winding support of the resistance wire, is still intact, but the wire is broken immediately at the end of the sensor. The sensor from cross section H2 was obviously damaged during drift excavation, but its previous failure due to cable damage is still to be supposed.

Fig. 5.2.5 Damaged temperature sensor from cross section F1

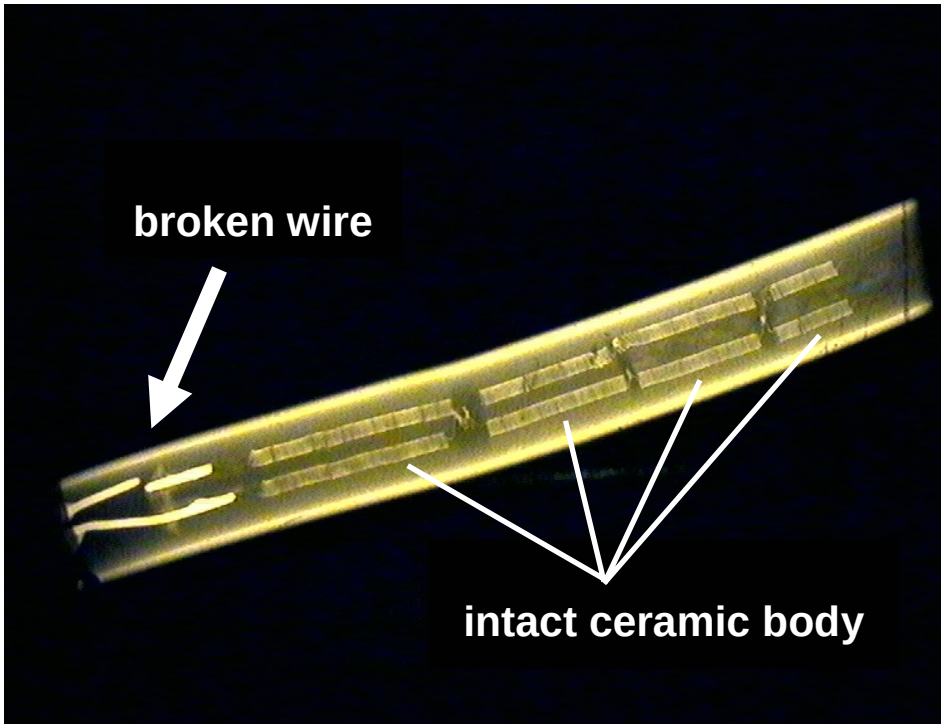

Fig. 5.2.6 X-ray picture of the damaged temperature sensor from cross section F1

5.3 Deformation Gauges

5.3.1 Convergence Measuring Devices

Glötzl SSKE 400 convergence measuring devices had been installed in different measuring cross sections for monitoring vertical and horizontal drift closure with electric Glötzl GWD 35/400 displacement transducers. During drift excavation, four convergence measuring devices were retrieved and shipped to the manufacturer Glötzl for re-calibration (Tab. 5.4).

Tab. 5.4 Retrieved convergence measuring devices

MCS	Position	Gauge Identification	Sensor Type	Sensor No.	Gauge No. Glötzl	Original Calibration	Status before Retrieval	Re-Calibration	Evaluation
$D1^{-1}$	horizontal 1.80 m	EL D1 099 K1 018	GWD 35/400	2	14 D1-1 B	13.12.89	ok. ?	15.11.01	gauge ok.
G1	horizontal 1.80 m vertical (wall side)	EL G1 168 K1 018 EL G1 170 K2 000	GWD 35/400 GWD 35/400	7 8	07 G1 B 08 G1 B	13.12.89 13.12.89	ok. cable failure	- 15.11.01	cable failure gauge ok.
B^{+1}	horizontal 1.80 m	EL B0 176 K1 018	GWD 35/400	10	12 B+1 B	13.12.89	cable failure	-	cable failure

Only the horizontal measuring device at cross section G1 (sensor 7) had been functioning until the end of the *in-situ* measurements. The horizontal convergence sensor 2 at cross section $D1^{-1}$ had revealed signal irregularities since 1993. The sensors 8 (G1 - vertical) and 10 (B^{+1} - horizontal) had failed in 1998 and 1992, respectively, obviously because of cable damages.

Before dismantling, the general condition and functioning of the measuring devices were checked. The measuring rods of both horizontal measuring devices at cross sections $D1^{-1}$ and B^{+1} were significantly bent due to distinct floor uplift in the heated area (Fig. 5.3.1 and 5.3.2). All measuring devices showed significant surface corrosion along the threaded anchor bolts, the spherical joints, and the joining outer protection tubes. Material break-through, however, was not detected. The middle part of the protection tubes was only slightly corroded (Fig. 5.3.2). The functioning of the measuring systems was not affected by corrosion. Controlled moving of the protection tubes, however, was not possible any more. Therefore, the measuring systems could not be calibrated as a whole before their dismantling.

Fig. 5.3.1 Bent horizontal convergence measuring device *in situ* (cross section B^{+1})

Fig. 5.3.2 Horizontal convergence measuring devices from cross sections B^{+1} and $D1^{-1}$ (both bent) and G1 (not bent) showing different corrosion of the protection tubes

For investigation of the electric displacement transducers, the protection tubes were removed (Fig. 5.3.3). Subsequently, the functioning of the displacement transducers was checked. The still functioning sensors were re-calibrated.

Fig. 5.3.3 Electric displacement transducer type Glötzl GWD 35/400 (sensor 8) after dismantling (spherical joint of the protection tube still mounted)

From the examined transducers, only sensor 8 was functioning completely (Tab. 5.4). As this measuring point had already failed during the *in-situ* measurements, its failure could be definitely attributed to cable damage. Sensor 2 was functioning, but the measuring pin of the displacement transducer was stuck mechanically probably due to the bending of the measuring rod in consequence of drift floor uplift. After dismantling of the displacement transducer, the measuring pin could be unstuck and the sensor was functioning again completely. The recorded signal irregularities, however, had been caused by electrical interference in the signal line and not by bending of the measuring rod.

Sensors 7 and 10 were not functioning. At sensor 7, a break in the multicore cable was detected just behind the displacement transducer. As its readings had been plausible until the end of the measuring period, the cable failure must have been occurred during the retrieval of the measuring system. The multicore cable of sensor 10 was short-circuited behind the sensor proving the assumption that this measuring point had failed during the testing period because of cable damage.

For verification of their accuracy, the two displacement transducers of the still functioning sensors 2 and 8 were re-calibrated. The re-calibration results are shown in Figures 5.3.4 and 5.3.5 together with the original calibration data from December 1989.

After almost 12 years of operation at temperatures of up to 86 °C (sensor 8) and 92 °C (sensor 2), respectively, the measuring range of both displacement transducers was nearly unchanged, but the sensors were more non-linear. For sensor 8, the linearity was still largely within the manufacturer's limit of tolerance of ±0.2 % (Fig. 5.3.4). For sensor 2, the linearity deviated from the original calibration (Fig. 5.3.5) what can easily be explained by the mechanical stressing of the displacement transducer due to the bending of the measuring rod.

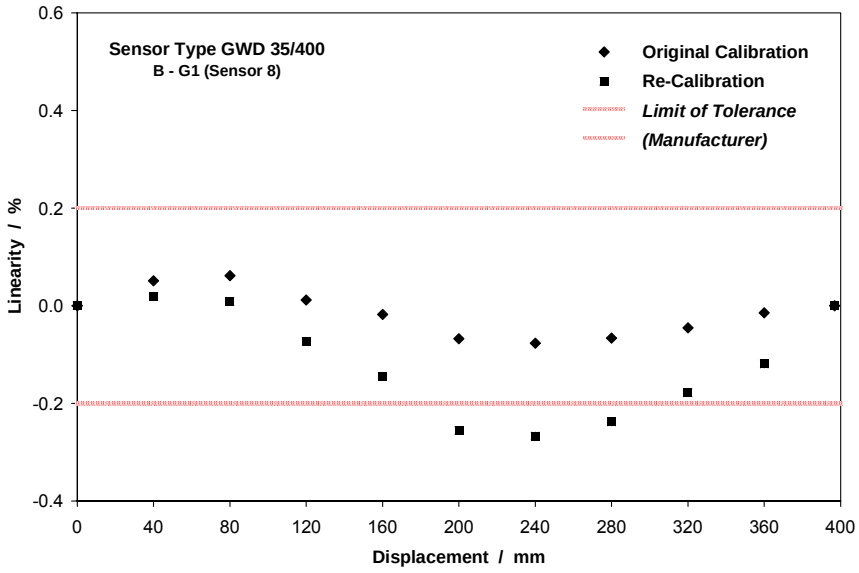

Fig. 5.3.4 Calibration of convergence measuring sensor 8 (cross section G1)

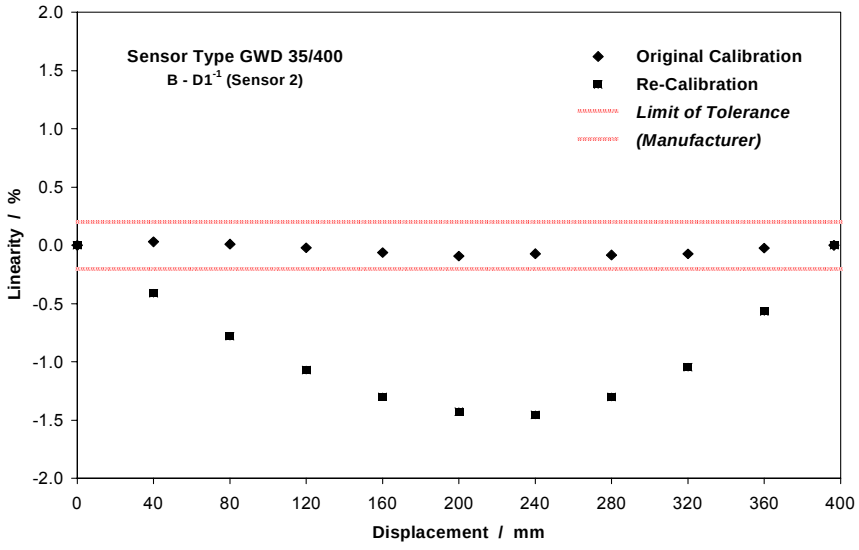

Fig. 5.3.5 Calibration of convergence measuring sensor 2 (cross section $D1^{-1}$)

5.3.2 Backfill Settling Measuring Devices

Backfill settling had been monitored in different measuring cross sections with measuring devices of the Glötzl type SSME (Fig. 5.3.6). Fabrication of the equipment had been performed by the subcontractor Interfels. With each device, the backfill settling had been recorded at three different levels with electric displacement transducers. The Interfels sensors were identical to the Glötzl transducer types GWD 35/400 and GWD 35/250, respectively.

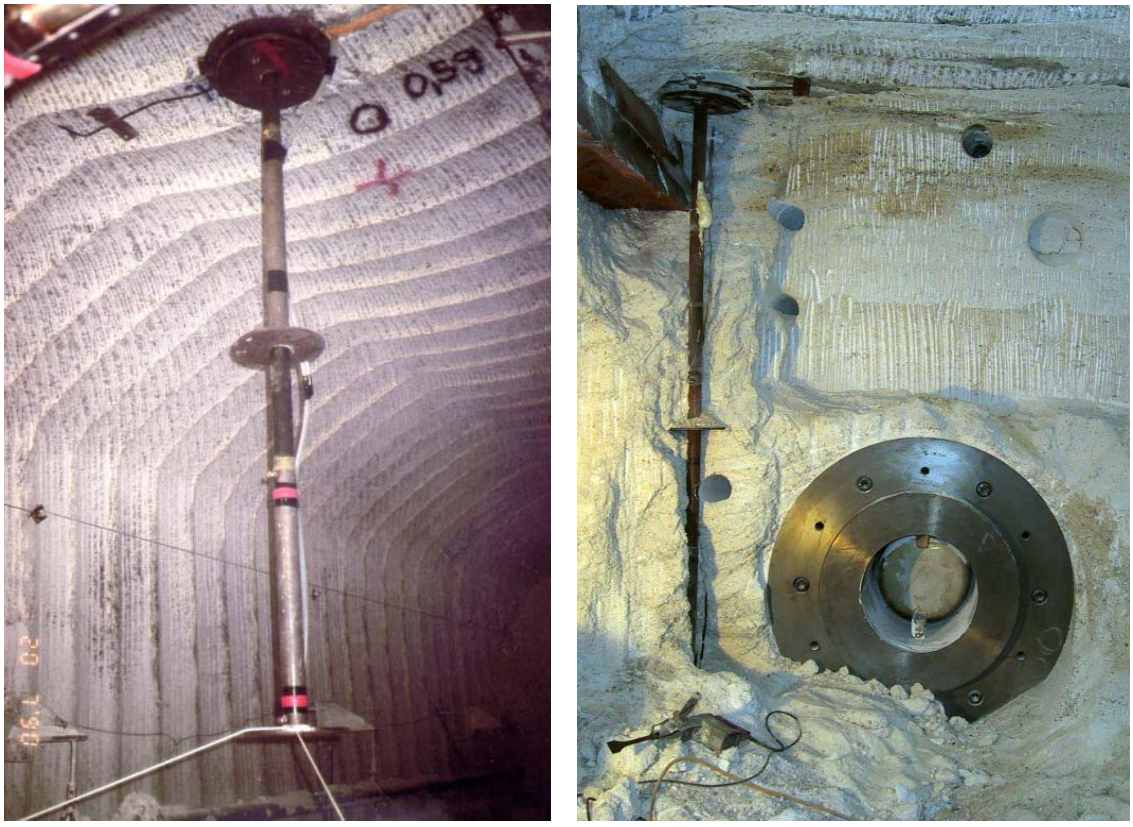

Fig. 5.3.6 Backfill settling measuring devices type Glötzl SSME *in situ* with three anchor plates for settling measurements at different levels. a: After installation. b: Before retrieval

During drift excavation, three backfill settling measuring devices were uncovered (Fig. 5.3.6 b). Since a complete retrieval was not possible, the devices were dismantled *in situ* (Fig. 5.3.7) and their displacement transducers were recovered (Fig. 5.3.8). All nine displacement transducers were shipped to Glötzl for further post-test analyses (Tab. 5.5).

Fig. 5.3.7 Backfill settling measuring device from cross section B^{+1}: Instrument head (foreground) and two anchor plates with part of the protection tube between

Fig. 5.3.8 Electric displacement transducers type Glötzl GWD 35/400 (sensors 16 and 17) and GWD 35/250 (sensor 18) after dismantling (lid of the instrument head still mounted)

Tab. 5.5 Retrieved backfill settling measuring devices

MCS	Position	Gauge Identification	Sensor Type	Sensor No.	Status before Retrieval	Re-Calibration	Evaluation
$E1^{+1}$	1.10 m (drift centre) 2.20 m (drift centre) 3.50 m (drift centre)	EL E1 194 V1 011 V2 022 V3 035	Interfels 400 mm Interfels 400 mm Interfels 250 mm	16 17 18	ok. ok. ok.	21.02.02 21.02.02 -	gauge ok. gauge ok. gauge failure
$D1^{-1}$	floor (pillar side) 1.80 m (pillar side) 3.50 m (pillar side)	EL D1 181 V1 000 V2 018 V3 035	Interfels 400 mm Interfels 400 mm Interfels 250 mm	10 11 12	ok. ok. ok.	- - -	gauge failure gauge failure gauge failure
B^{+1}	floor (pillar side) 1.80 m (pillar side) 3.50 m (pillar side)	EL B0 142 V1 000 V2 018 V3 035	Interfels 400 mm Interfels 400 mm Interfels 250 mm	4 5 6	cable failure cable failure cable failure	04.03.02 - -	gauge ok. gauge failure gauge failure

Both backfill settling measuring devices from cross sections $E1^{+1}$ (sensors 16, 17, 18) and $D1^{-1}$ (sensors 10, 11, 12) had been functioning completely until the end of the *in-situ* measurements. The sensors 4, 5, and 6 of the measuring device at cross section B^{+1} had failed between 1997 and 1998, possibly due to cable damages.

The post-test examinations revealed that the sensors 6, 11, and 12 were not functioning because the measuring pin of the displacement transducer was stuck mechanically. This was probably caused by corrosion at the outlet of the measuring pin at the end of the displacement transducer housing. Even by strong pushing or pulling, none of the measuring pins could be unstuck. Since two of the sensors had been functioning until the end of the *in-situ* measurements, the corrosion of the measuring pins must have taken place after uncovering and dismantling of the measuring devices. After retrieval from the underground and exposure to the air humidity above ground, accelerated corrosion can generally be observed at every steel equipment that had been installed in rock salt.

The electrical examination of the displacement transducers showed an unstable potentiometer resistance for the sensors 5, 6, and 18 probably due to moisture impact. The respective sensors must be considered defect. As the readings of sensor 18 had been plausible until the end of the *in-situ* measurements it is concluded that at least the failure of this sensor occurred after uncovering and dismantling.

Sensor 10, which had been functioning until the end of the *in-situ* measurements, too, recorded no measuring signal. Obviously, the displacement transducer was damaged mechanically during dismantling as its measuring pin was pushed in too much.

Sensor 4, however, was functioning completely thus confirming that its failure during the heating phase had been caused by cable damage. This is also likely for sensors 5 and 6.

All sensors which were still functioning (all identical to the Glötzl transducer type GWD 35/400) were re-calibrated. For sensor 17, a precision calibration was performed while the re-calibration of the sensors 4 and 16 was only coarse. After almost 12 years of operation at temperatures of 49 °C (sensors 16 and 17) and approximately 90 °C (sensor 4), respectively, their linearity was still largely within the manufacturer's limit of tolerance of ±0.2 %. The re-calibration result of sensor 17 is shown in Figure 5.3.9.

For the Interfels sensors, no data sheets of the original calibration were available, but only exemplary data sheets for both sensor types (400 mm and 250 mm). The exemplary calibration values for the sensor type 400 mm are also depicted in Figure 5.3.9, but cannot be directly compared with the re-calibration results of sensor 17.

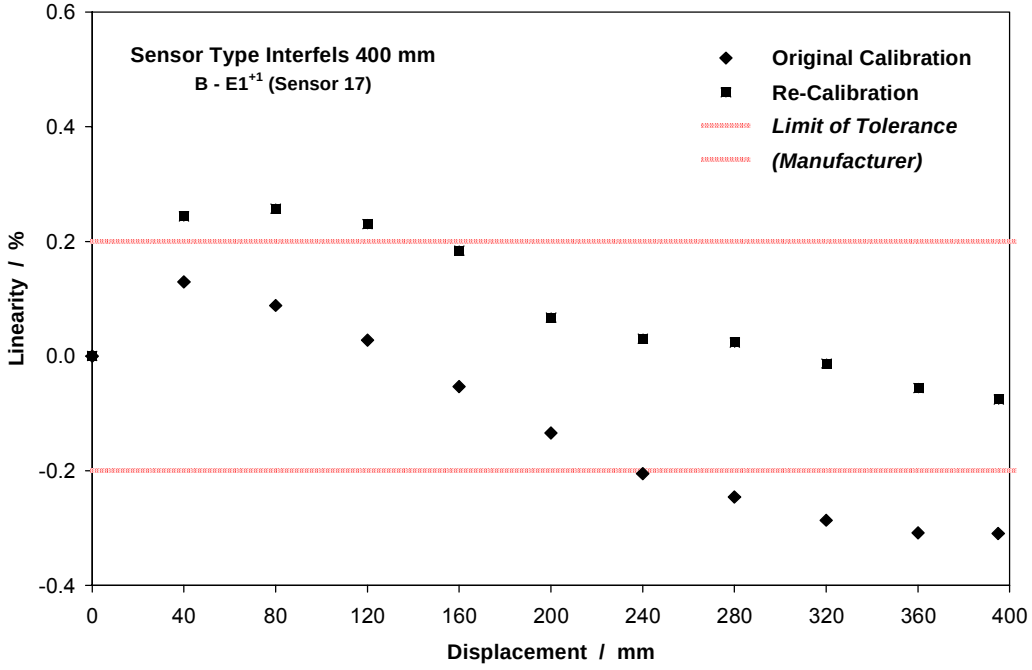

Fig. 5.3.9 Calibration of backfill settling measuring sensor 17 (cross section $E1^{+1}$)

5.3.3 Extensometer

For measuring rock deformation, extensometers had been installed in boreholes at different cross sections. From the observation drifts on the 750-m level, multiple-point glass fibre rod extensometers of the Glötzl type GKSE 16 (Fig. 5.3.10) had been installed which recorded the displacements with transducers of the Glötzl type GWW 50/50. The displacement transducers had been placed at the borehole collar on the 750-m level. The test drifts on the 800-m level had been instrumented with multiple-point glass fibre rod extensometers of the Glötzl type TEX 16 (Fig. 5.3.11). Because of the high temperatures in the test drifts, their displacement transducers of the Glötzl types GWD 35/400, GWD 35/250, and GWD 35/100 had not been mounted at the borehole collar, but in a tight instrument head in the deepest part of the borehole (Fig. 5.3.12).

Fig. 5.3.10 Glass fibre rod extensometer type Glötzl GKSE 16 (installed from the observation drifts on the 750-m level)

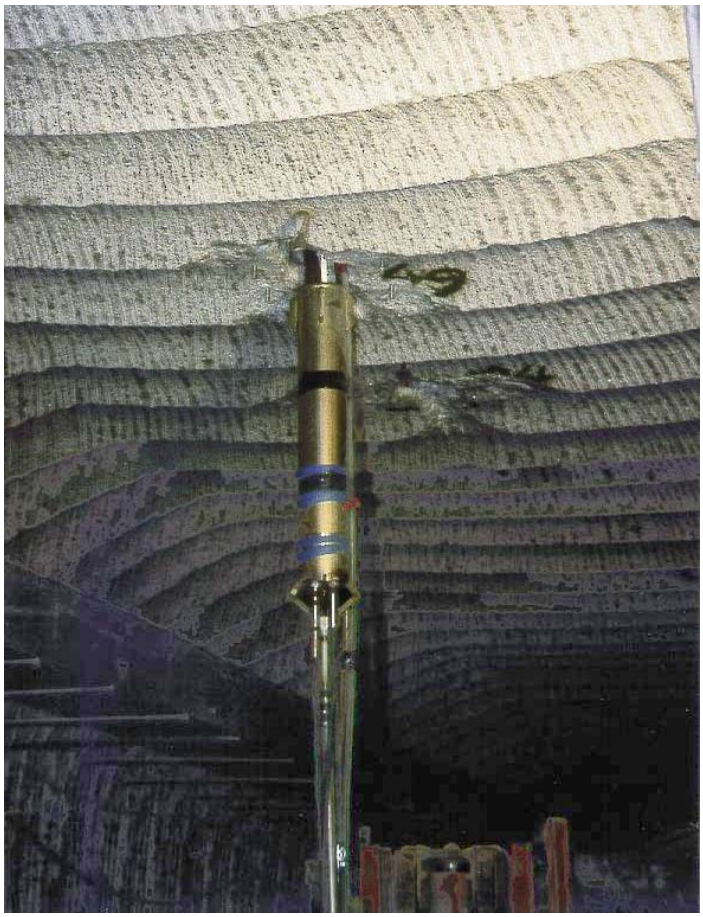

Fig. 5.3.11 Glass fibre rod extensometer type Glötzl TEX 16 with instrument head during installation in the test drift roof on the 800-m level

Fig. 5.3.12 Open instrument head of extensometer type Glötzl TEX 16 holding the electric displacement transducers (left side) with already connected extensometer protection tubes holding the glass fibre rods (right side)

After installation of the extensometers, all boreholes had been filled with a supporting cementation. Thus, neither the extensometers nor those displacement transducers, which had been installed in the deepest part of the boreholes, were accessible during drift excavation. The displacement transducers at the borehole collars on the 750-m level, however, could be retrieved. The attempt of recovering an additional calibration extensometer, which had been installed in a steel casing in borehole 63 at cross section $D1^{-2}$ for determining the necessary temperature correction, was cancelled because of the unreasonable retrieval effort.

Because several extensometers had failed during the heating phase, a number of extensometers had been replaced by gauges of the same type. The replacement boreholes had been drilled from the observation drifts on the 750-m level and the access drifts on the 800-m level. The displacement transducers of the Glötzl types GWD 35/400, GWD 35/250, GWD 35/100, and GWW 100 I had been mounted at the borehole collar thus being still accessible (Fig. 5.3.13).

From borehole collars on the 750-m level and on the 800-m level, a total of 43 displacement transducers was retrieved (Tab. 5.6). A representative number of different transducer types was selected for re-calibration at the manufacturer.

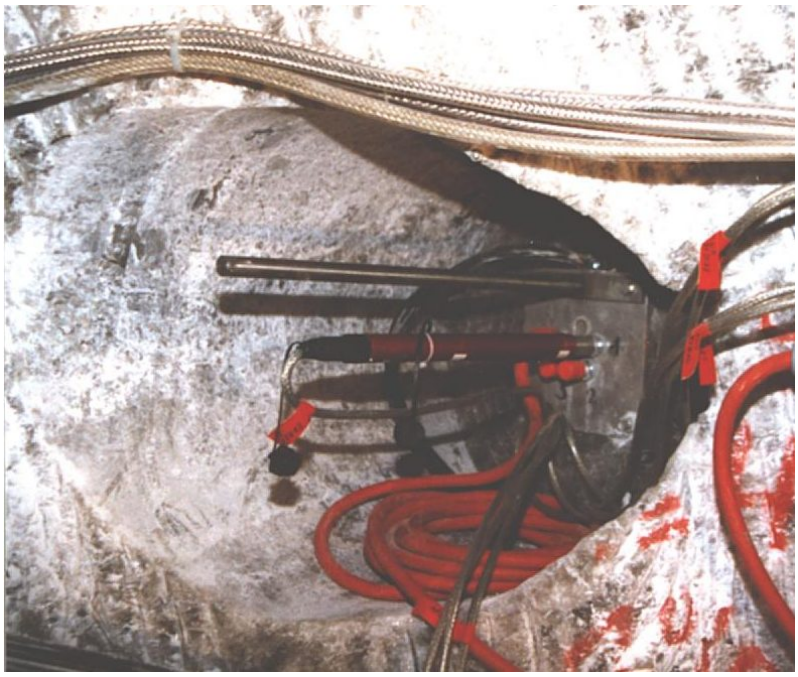

Fig. 5.3.13 Extensometer replacement borehole: Borehole collar with mounted electric displacement transducer type Glötzl GWD 35/400 (access drift on the 800-m level)

Tab. 5.6 Retrieved extensometer displacement transducers

MCS	Position	Gauge Identification	Sensor Type	Sensor No.	Gauge No. Glötzl	Original Calibration	Status before Retrieval	Re-Calibration	Evaluation
A	borehole 006	ÜF A0 006 E1 445	GWW 50/50	1	87454	27.11.87	ok.	07.11.01 - precise	gauge ok.
	borehole 006	E2 425	GWW 50/50	2	901138 (new)	08.08.90	ok.	07.11.01 - precise	gauge ok.
	borehole 006	E3 385	GWW 50/50	3	87458	27.11.87	ok.	-	-
	borehole 006	E4 305	GWW 50/50	4	87459	27.11.87	ok.	-	-
	borehole 006	E5 145	GWW 50/50	5	901139 (new)	08.08.90	ok.	-	-
A	borehole 007	ÜF A0 007 E1 445	GWW 50/50	6	87447	27.11.87	ok.	-	-
	borehole 007	E2 425	GWW 50/50	7	87451	27.11.87	ok.	-	-
	borehole 007	E3 385	GWW 50/50	8	87456	27.11.87	ok.	-	-
	borehole 007	E4 305	GWW 50/50	9	87445	27.11.87	ok.	-	-
	borehole 007	E5 145	GWW 50/50	10	87450	27.11.87	ok.	-	-
A	borehole 008	ÜF A0 008 E1 650	GWW 50/50	11	87449	27.11.87	ok.	07.11.01 - coarse	gauge ok.
	borehole 008	E2 570	GWW 50/50	12	87448	27.11.87	ok.	07.11.01 - coarse	gauge ok.
	borehole 008	E3 530	GWW 50/50	13	87453	27.11.87	ok.	-	-
	borehole 008	E4 510	GWW 50/50	14	87452	27.11.87	ok.	-	-
	borehole 008	E5 490	GWW 50/50	15	87460	27.11.87	ok.	-	-
	borehole 008	E3 470	GWW 50/50	16	87443	27.11.87	ok.	-	-
	borehole 008	E4 450	GWW 50/50	17	87444	27.11.87	ok.	-	-
	borehole 008	E5 410	GWW 50/50	18	87446	27.11.87	ok.	-	-
D1	borehole 225	EL D1 225 E1	GWD 35 / 400	33	001 - 12/89	27.06.94	ok.	08.11.01 - coarse	gauge ok.
	borehole 225	E2	GWD 35 / 400	34	003 - 12/89	27.06.94	ok.	08.11.01 - precise	gauge ok.
	borehole 225	E3	GWD 35 / 250	35	009 - 12/89	11.08.94	ok.	08.11.01 - precise	gauge ok.
	borehole 225	E4	GWD 35 / 250	36	011 - 12/89	11.08.94	ok.	08.11.01 - coarse	gauge ok.
	borehole 225	E5	GWD 35 / 100	14	016 - 12/89	28.06.94	ok.	08.11.01 - precise	gauge ok.
D1	borehole 226	EL D1 226 E1	GWW 100 I	37	941611	10.08.94	ok.	07.11.01 - precise	gauge ok.
	borehole 226	E2	GWW 100 I	38	941612	10.08.94	ok.	07.11.01 - coarse	gauge ok.
	borehole 226	E3	GWW 100 I	39	941613	10.08.94	ok.	07.11.01 - precise	gauge ok.
	borehole 226	E4	GWW 100 I	40	941614	10.08.94	ok.	07.11.01 - coarse	gauge ok.
	borehole 226	E5	GWW 100 I	15	941615	10.08.94	ok.	-	-
D1	borehole 227	EL D1 227 E1	GWD 35 / 400	45	004 - 12/89	27.06.94	ok.	-	-
	borehole 227	E2	GWD 35 / 400	46	005 - 12/89	27.06.94	ok.	-	-
	borehole 227	E3	GWD 35 / 250	47	012 - 12/89	11.08.94	ok.	-	-
	borehole 227	E4	GWD 35 / 250	48	013 - 12/89	11.08.94	ok.	-	-
	borehole 227	E5	GWD 35 / 100	18	017 - 12/89	28.06.94	ok.	-	-
D1	borehole 228	EL D1 228 E1	GWD 35 / 400	41	006 - 12/89	27.06.94	ok.	-	-
	borehole 228	E2	GWD 35 / 400	42	007 - 12/89	27.06.94	ok.	-	-
	borehole 228	E3	GWD 35 / 250	43	014 - 12/89	11.08.94	ok.	-	-
	borehole 228	E4	GWD 35 / 250	44	015 - 12/89	11.08.94	ok.	-	-
	borehole 228	E5	GWD 35 / 100	17	018 - 12/89	28.06.94	ok.	-	-
A	borehole 229	EL A0 229 E1	GWD 35 / 400	5	008 - 12/89	27.06.94	ok.	-	-
	borehole 229	E2	GWD 35 / 400	6	941596	01.07.94	ok.	-	-
	borehole 229	E3	GWD 35 / 250	7	941599	01.07.94	ok.	-	-
	borehole 229	E4	GWD 35 / 250	8	941600	01.07.94	ok.	-	-
	borehole 229	E5	GWD 35 / 100	13	019 - 12/89	28.06.94	ok.	-	-

From the displacement transducers type GWW 50/50 (Fig. 5.3.14) which had been used on the 750-m level, the sensors 1 and 2 from borehole 006 were selected for precision calibration, and the sensors 11 and 12 from borehole 008 for coarse calibration. For re-calibration of the sensor types GWD 35/400, GWD 35/250, and GWD 35/100, five transducers from replacement borehole 225 were taken (Fig. 5.3.15). Actually, these sensor types had been used for all extensometers originally installed in the test drifts. From each type GWD 35/400 and GWD 35/250, one sensor was precision calibrated and another one coarse calibrated, respectively. Sensor type GWD 35/100 was precision calibrated.

Fig. 5.3.14 Electric displacement transducers type GWW 50/50 (borehole 006: sensors 1 and 2)

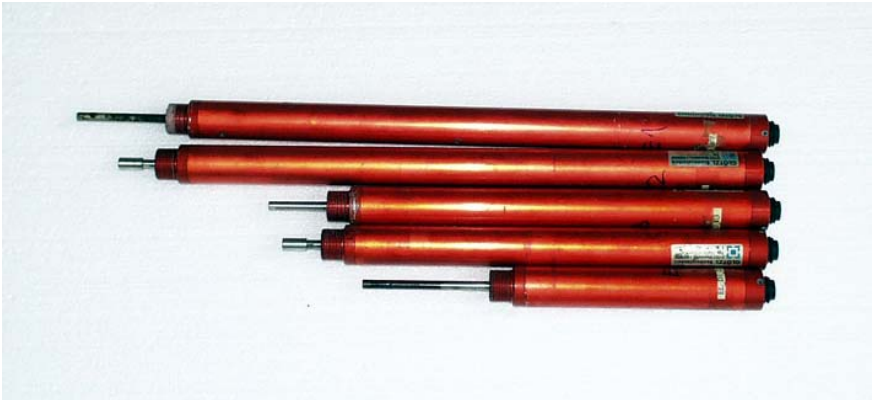

Fig. 5.3.15 Electric displacement transducers type GWD 35/400 (borehole 225: sensors 33 and 34), GWD 35/250 (borehole 225: sensors 35 and 36), and GWD 35/100 (borehole 225: sensor 14)

Fig. 5.3.16 Electric displacement transducers type GWW 100 l (borehole 226: sensors 37 to 40)

In replacement borehole 226, inductive displacement transducers of the Glötzl type GWW 100 I had been applied because of the required cable length (Fig. 5.3.16). For two of these sensors, a precision calibration was performed. Additionally, two sensors were coarse calibrated.

From the examined transducers, two sensors from borehole 225 were not functioning completely at first. At one sensor, the measuring pin had been pushed in too much probably during retrieval leading to damage at its collector ring which is picking up the resistance signal from the potentiometer. After exchange of the collector ring, the displacement transducer was functioning again. At another displacement transducer, the measuring pin was stuck mechanically. Since there was no indication of a deformation, this was probably caused by corrosion at the outlet of the measuring pin at the end of the displacement transducer housing. The measuring pin could be unstuck again and the sensor was functioning completely before re-calibration started.

The precision re-calibration results of the different sensor types are shown in Figures 5.3.17 to 5.3.23 together with the original calibration data.

The original calibration of the displacement transducers type GWW 50/50, which had been used on the 750-m level, had been performed in 1987. After their installation, the sensors had been in operation until the end of the *in-situ* measurements. The ambient temperature at the borehole collar was 33.5 °C. After 14 years, the re-calibration results showed an almost unchanged linearity (Fig. 5.3.17 and 5.3.18). Only at sensor 1, a deviation from the original calibration occurred in the lower measuring range, but its linearity is still within the manufacturer's limit of tolerance of ±0.5 %.

The selected displacement transducers types GWD 35/400, GWD 35/250, and GWD 35/100 from replacement borehole 225 had been in operation for almost 7 years at an ambient temperature of 36 °C. Their original calibration had been carried out in 1994. All sensors revealed an almost identical linearity of original calibration and re-calibration being still within the manufacturer's limit of tolerance of ±0.2 %. The precision calibration results of the three sensor types are presented in Figures 5.3.19 to 5.3.21.

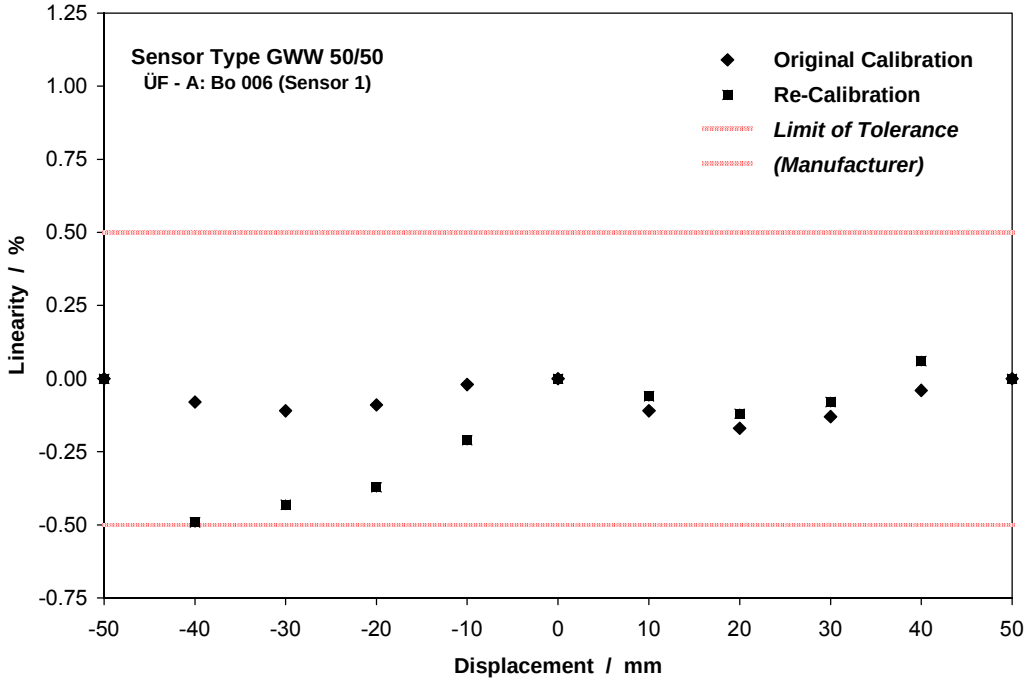

Fig. 5.3.17 Calibration of sensor 1 of borehole 006 (type GWW 50/50)

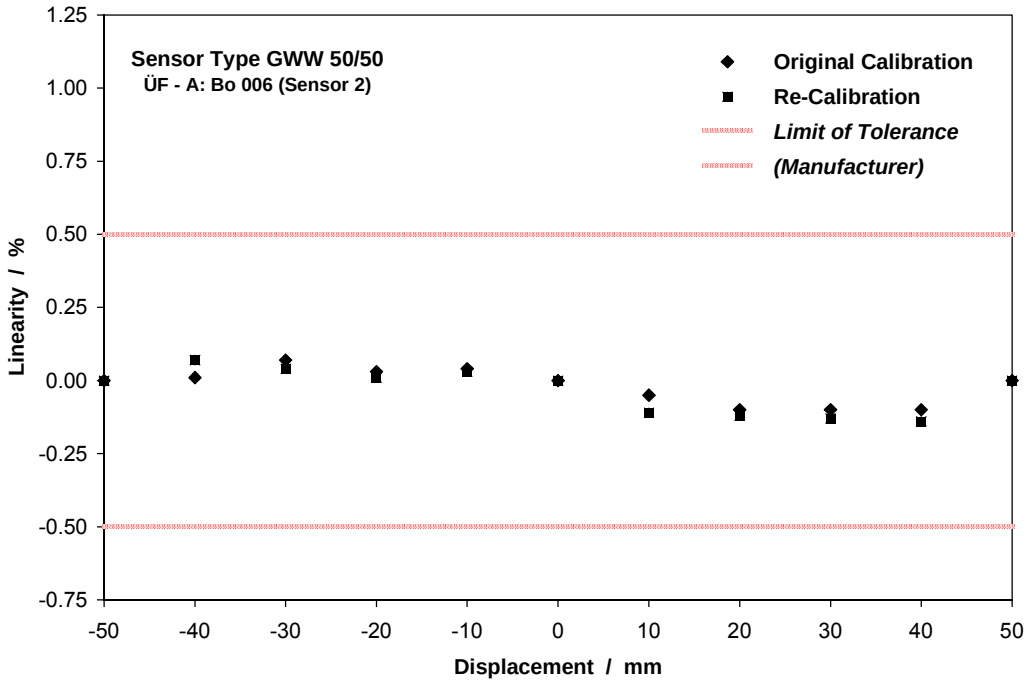

Fig. 5.3.18 Calibration of sensor 2 of borehole 006 (type GWW 50/50)

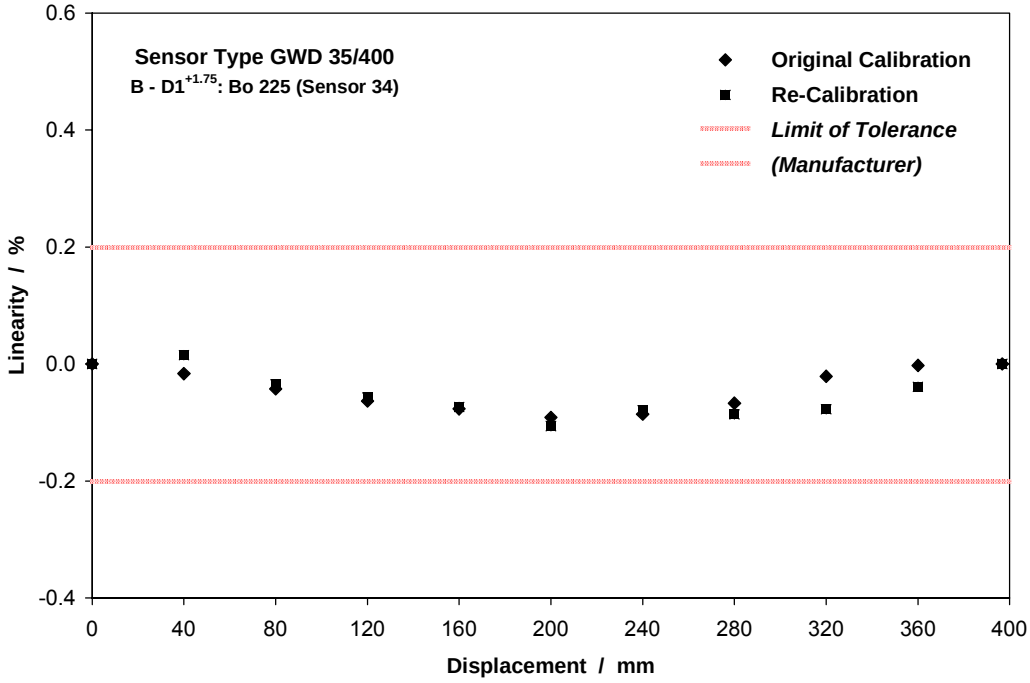

Fig. 5.3.19 Calibration of sensor 34 of borehole 225 (type GWD 35/400)

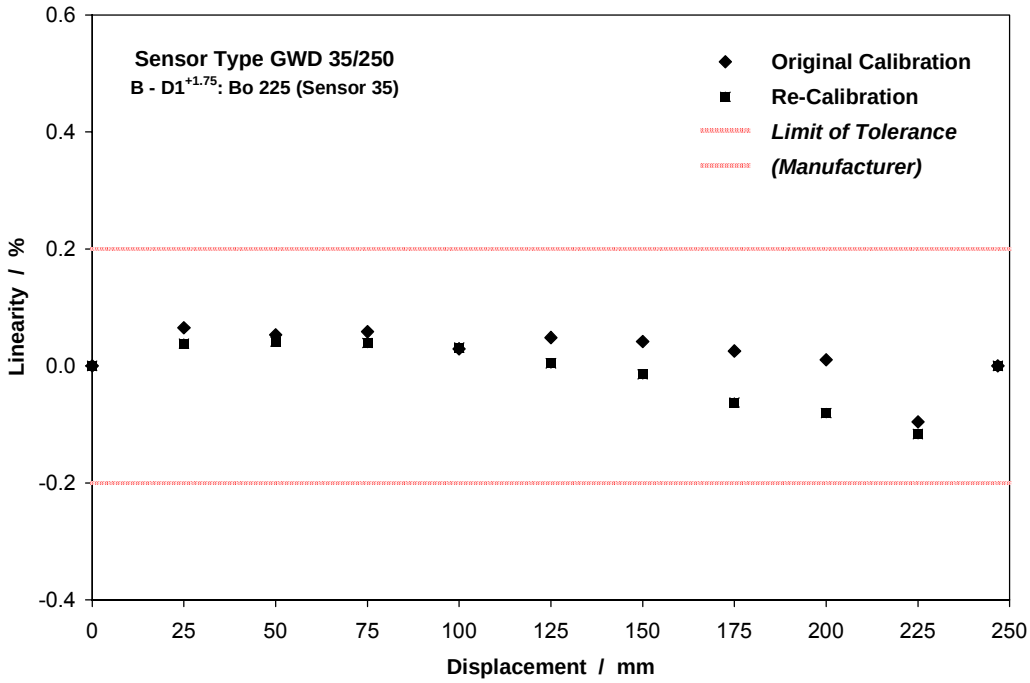

Fig. 5.3.20 Calibration of sensor 35 of borehole 225 (type GWD 35/250)

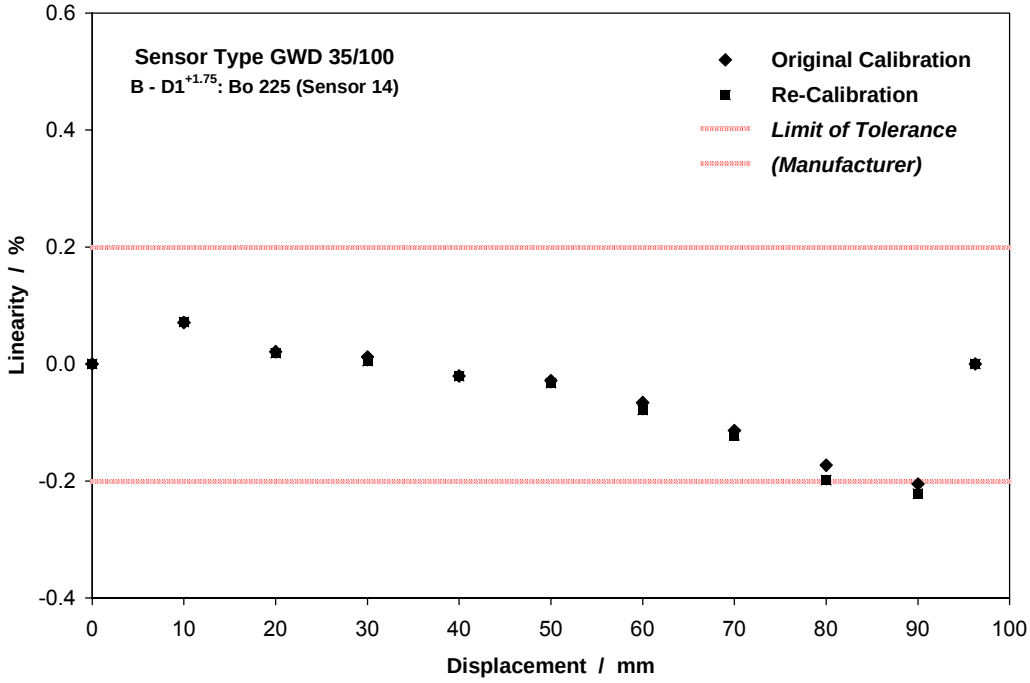

Fig. 5.3.21 Calibration of sensor 14 of borehole 225 (type GWD 35/100)

Contrarily to the identical displacement transducers of the convergence measuring devices which got slightly non-linear during operation (Fig. 5.3.4 and 5.3.5), the linearity of the extensometer sensors hardly changed. The deviation of the convergence measuring sensors can be attributed to the higher temperatures of up to 90 °C which these displacement transducers had been exposed to during the heating period. But the installation of the convergence measuring sensors had only been possible directly in the heated test drifts. The ambient conditions of the extensometer displacement transducers, however, were more favourite as they had been mounted at a long distance from the heated test drifts.

The original calibration of the displacement transducers type GWW 100 I, which had been used in replacement borehole 226, had also been performed in 1994. Equally, these sensors had been in operation for almost 7 years at an ambient temperature of 36 °C. The re-calibration revealed a decrease in linearity, but most sensors were still within the manufacturer's limit of tolerance of ±0.2 % (Fig. 5.3.22). Only at one gauge, the linearity deviated significantly from the original calibration (Fig. 5.3.23).

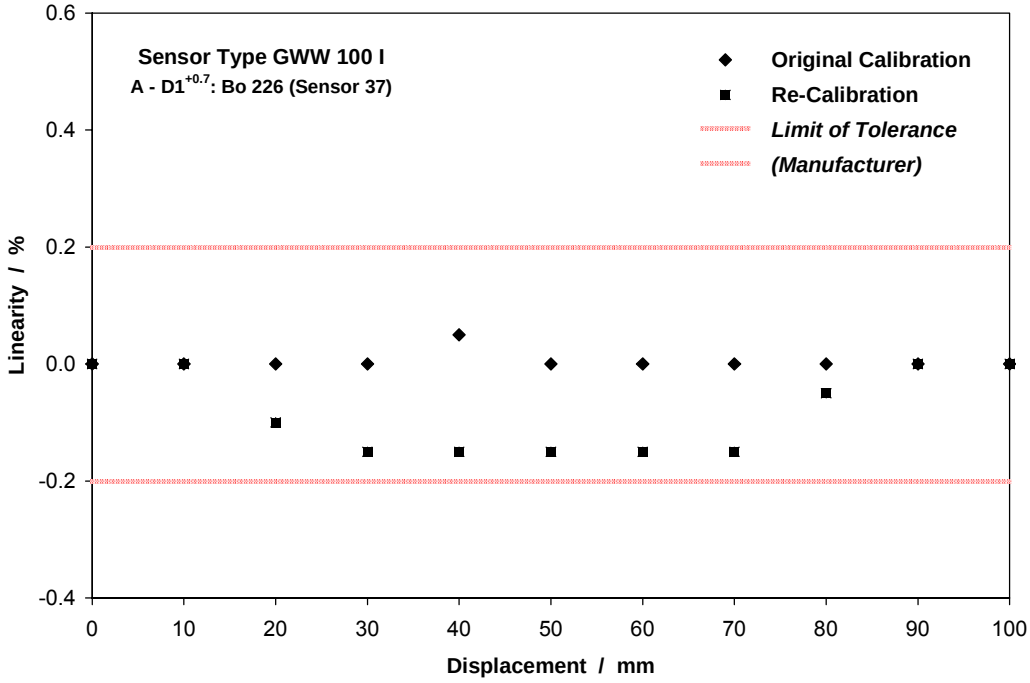

Fig. 5.3.22 Calibration of sensor 37 of borehole 226 (type GWW 100 I)

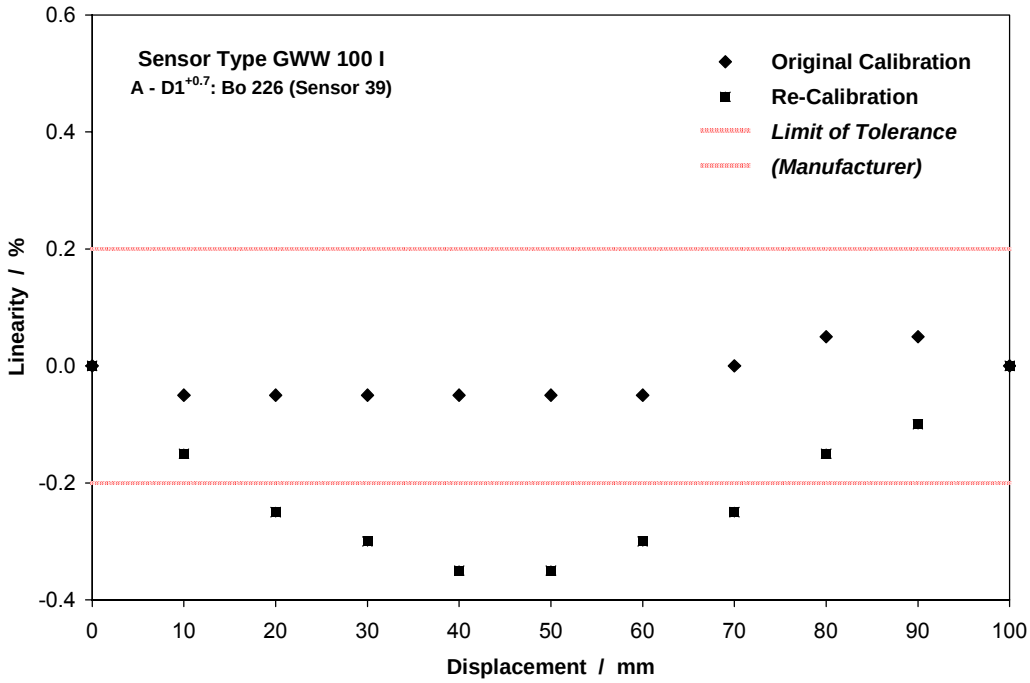

Fig. 5.3.23 Calibration of sensor 39 of borehole 226 (type GWW 100 I)

5.4 Pressure Gauges

5.4.1 Hydraulic Pressure Cells

Hydraulic pressure cells of the Glötzl type F 20/30 QS 400 A Z4 had been used to determine the pressure at the interfaces between backfill and surrounding rock. The pressure cells had been installed at the floor, at the roof, and at the walls of the test drifts (Fig. 5.4.1).

From the cross sections E1, D1, G1, and B, a number of 15 pressure gauges was retrieved and shipped to the manufacturer Glötzl for post-test analyses (Tab. 5.7). Eight gauges had been functioning until the end of the *in-situ* measurements, one gauge had revealed signal irregularities, and six measuring points had failed probably due to damaged hydraulic measuring lines (Fig. 5.4.2). Their failure reason had to be confirmed by the manufacturer.

Tab. 5.7 Retrieved backfill pressure gauges

MCS	Position	Gauge Identification	Gauge No.	Gauge No. Glötzl	Initial Zero Value	Status before Retrieval	New Zero Value	General Condition	Evaluation
E1	floor	EL E1 BST S1 000	48	61974	1,50 bar	ok.	1,46 bar		gauge ok.
	wall	S2 018	49	61975	1,44 bar	line failure	1,52 bar		gauge ok.
	pillar	S3 018	50	61976	1,52 bar	ok.	1,64 bar		gauge ok.
D1	floor (pillar side)	EL D1 BST S1 000	30	61969	1,50 bar	line failure	1,28 bar	shield bar broken	gauge ok.
	floor (wall side)	S2 000	31	61970	1,62 bar	line failure	1,31 bar	shield bar broken	gauge ok.
	wall	S3 018	32	61971	1,44 bar	line failure	0,58 - 1,0 bar	fouling of valve diaphragm	valve failure
	roof	S4 035	33	61972	1,48 bar	ok.	1,64 bar		gauge ok.
	pillar	S5 018	34	61973	1,52 bar	ok.	1,48 bar	shield bar broken	gauge ok.
G1	wall	EL G1 BST S2 018	56	61966	1,46 bar	ok.	-	damaged, filling run empty	gauge failure at retrieval
	pillar	S4 018	58	61968	1,40 bar	irregularities	1,44 - 3,8 bar	fouling of valve diaphragm	valve failure
B	floor (pillar side)	EL B0 BST S1 000	20	61960	1,50 bar	ok.	1,21 bar		gauge ok.
	floor (wall side)	S2 000	21	61961	1,46 bar	ok.	1,30 bar		gauge ok.
	wall	S3 018	22	61962	1,44 bar	line failure	0,12 bar	damaged, filling run empty	gauge failure at retrieval
	roof	S4 035	23	61963	1,54 bar	line failure	1,42 bar	slightly damaged	gauge ok.
	pillar	S5 018	24	61964	1,46 bar	ok.	1,25 bar		gauge ok.

The general condition of the pressure gauges was satisfactory. The surface of the pressure pads was mostly corroded, but the cells remained tight (Fig. 5.4.3). During dismantling, the attachment lugs of some pressure cells were damaged (Fig. 5.4.4). With these attachment lugs, the pressure pads had been fixed at the rock. From the deformation of the lugs, the whole pressure cell may be involved leading to a change in the initial pressurization of the gauge which is a key specification of every pressure cell.

Fig. 5.4.1 Pressure gauge 61975 *in situ* at the drift wall (bottom side)

Fig. 5.4.2 Corroded hydraulic measuring lines of pressure gauge 61975

Fig. 5.4.3 Pressure gauge 61960 (bottom side) with corroded surface

Fig. 5.4.4 Pressure gauge 61972 (upper side) with damaged attachment lugs

Fig. 5.4.5 Pressure gauge 61966 (upper side) – damaged by the continuous miner during drift excavation

During drift excavation, two pressure pads were damaged significantly by the continuous miner and their filling ran empty (Fig. 5.4.5).

Proper function of all undamaged gauges was tested. For this purpose, the pressurization of the unstressed pressure cell was measured and compared with the initial pressurization (zero value). At 11 gauges, the percentage change of this zero value (relative to the total measuring range of 400 bar) was between 0.01 % and 0.08 % (Fig. 5.4.6). According to the manufacturer, zero deviations of up to 0.1 % are very tolerable after the long operation time of these measuring gauges. Their *in-situ* readings were hence assessed as very confidential.

At the pressure cells 61968 and 61971, the zero value was unsteady due to fouling of the valve diaphragm. Both gauges were considered to be defect. At pressure gauge 61968, signal irregularities had already been observed during the heating phase. Therefore, its *in-situ* readings had not been allowed for the evaluation. Gauge 61971 had already failed in 1992, probably due to damaged hydraulic measuring lines.

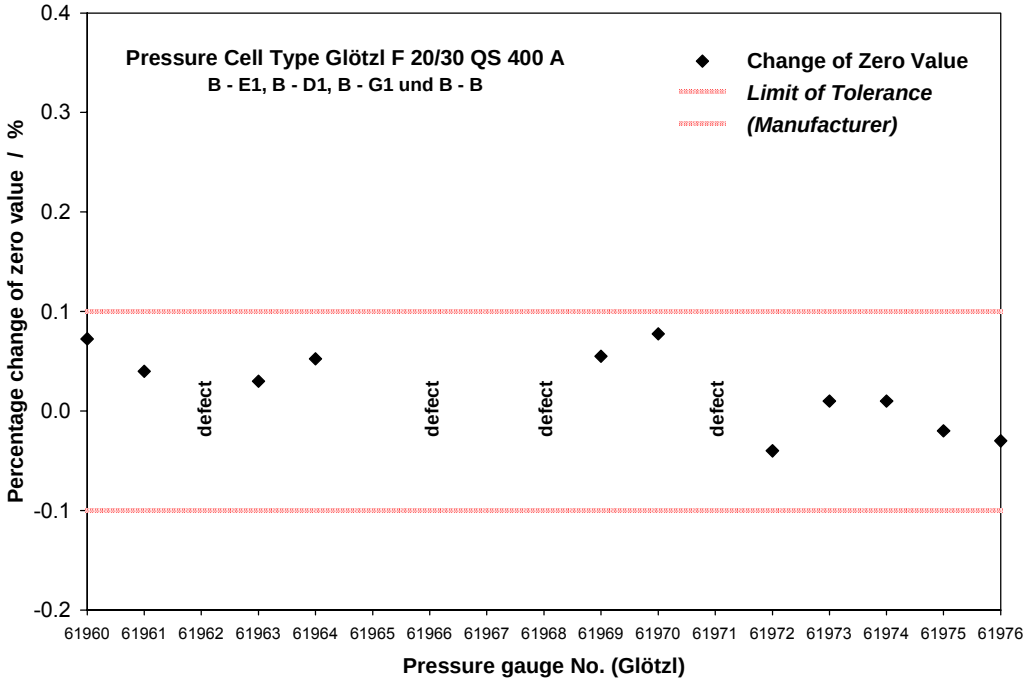

Fig. 5.4.6 Percentage change of initial pressurization (zero value) of backfill pressure gauges (relative to the total measuring range of 400 bar)

The post-test examination of the remaining failed measuring points (Tab. 5.7) revealed that four pressure gauges were functioning completely implying that their failure during the *in-situ* measurements was definitely caused by damaged hydraulic measuring lines. The failure reason of pressure gauge 61962, however, could not be verified definitely as the pressure pad had been damaged by the continuous miner during drift excavation.

For verification of their accuracy, two backfill pressure gauges were selected for precision calibration in an autoclave (Fig. 5.4.7). In the autoclave, the pressure cells were loaded stepwise by increments of 50 bar up to the final value of 400 bar. The readings were compared with the nominal pressure values, respectively. At lower pressures up to 40 bar, the maximum backfill pressure at the end of the *in-situ* measurements, the deviations from the nominal pressure were below 2 bar showing the high reliability of the cells in this pressure range. With increasing pressure, the deviations from the nominal pressure increased, but were still within the order of magnitude which had been expected by the manufacturer.

From the deviations with respect to the nominal pressure curve, the linearity was determined which is related to the total measuring range of 400 bar (Fig. 5.4.8 and 5.4.9). The linearity of both gauges was still largely within the manufacturer's limit of tolerance of ±0.5 %.

Fig. 5.4.7 Pressure gauge 61972 before calibration in the autoclave

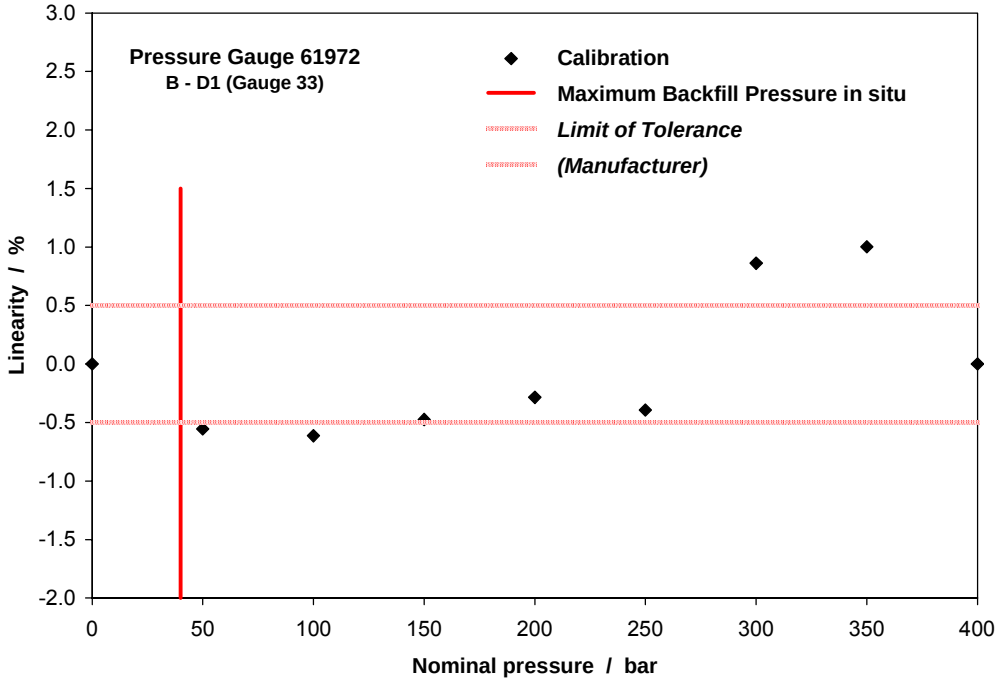

Fig. 5.4.8 Calibration of pressure gauge 61972 in the autoclave

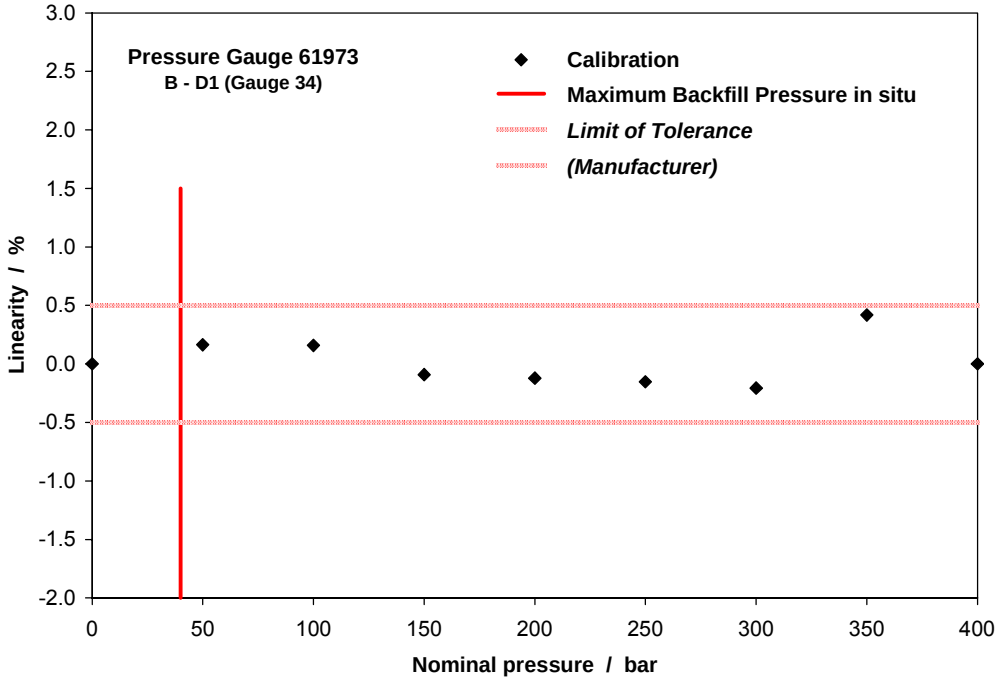

Fig. 5.4.9 Calibration of pressure gauge 61973 in the autoclave

5.4.2 AWID Gauges

At the surface of the heater casks, a determination of backfill pressure had not been possible with hydraulic measuring systems because the expected temperatures had been too high. For these measurements, AWID gauges had been applied which were operated electropneumatically. The AWID gauges had been fixed inside steel casings which had been welded at the surface of the heater casks (Fig. 5.4.10). After mounting, the AWID gauges had been embedded with saltcrete.

Almost all AWID measuring systems had failed soon after the beginning of the heating phase, probably due to damaged pneumatic and/or electric measuring lines. Therefore, the whole AWID measuring unit had been shut down early. With the post-test analyses, condition and functioning of selected AWID gauges were checked.

During drift excavation, three steel casings with their embedded AWID gauges were retrieved from the central heater cask in cross section B (Tab. 5.8). At the manufacturer Glötzl, the gauges were checked electrically and pneumatically under vacuum before the saltcrete was removed. The examination revealed that all AWID gauges were tight and completely functional. Consequently, their failure during the *in-situ* measurements was definitely caused by damaged measuring lines.

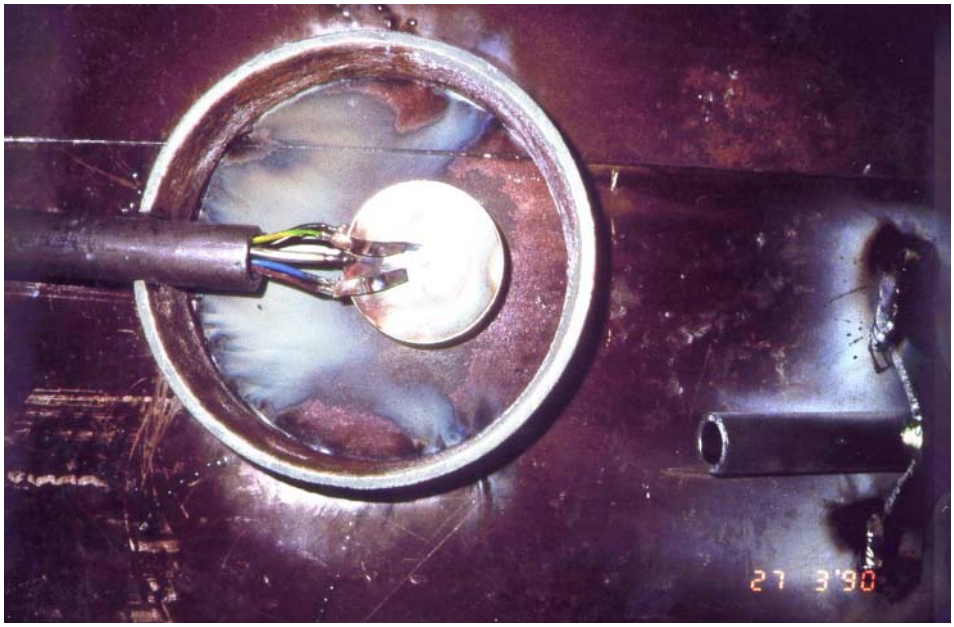

Fig. 5.4.10 AWID gauge *in situ* at the surface of a heater cask (before embedding with saltcrete)

For calibration in the autoclave, the saltcrete embedding of the AWID gauges was removed (Fig. 5.4.11). The retrieved pressure gauges were only slightly corroded. But during removal of the saltcrete, the delicate gauges were damaged. Therefore, a calibration in the autoclave was not possible any more.

Tab. 5.8 Retrieved AWID gauges

MCS	Position	Gauge Identification	Gauge No.	Gauge No. Glötzl	Status before Retrieval	Evaluation
B	cask surface (right) cask surface (top) cask surface (left)	EL B0 BBH S1 008 S2 015 S3 008	256 257 258	16 15 14	ok. ? ok. ? line failure	gauge ok. gauge ok. gauge ok.

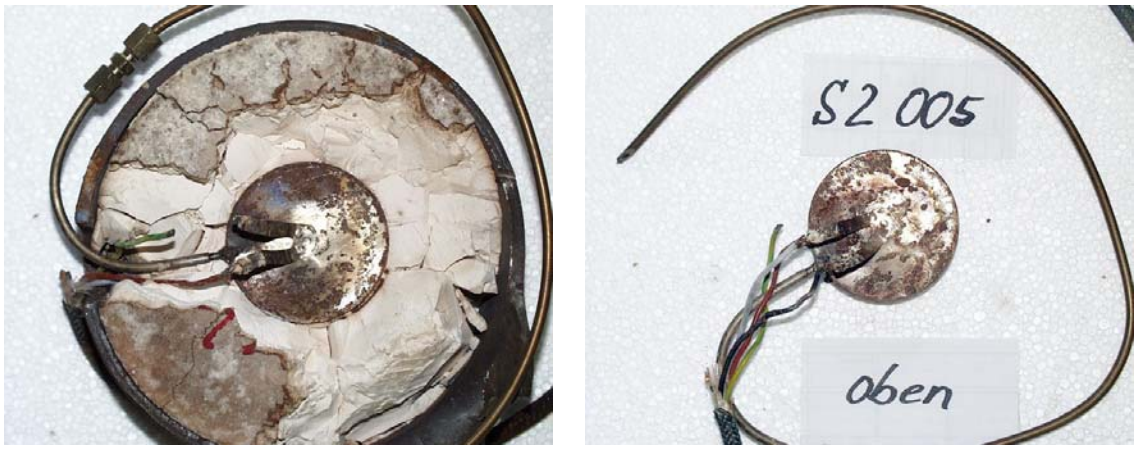

Fig. 5.4.11 AWID gauge 257 with pneumatic and electric measuring lines. a: During removal of its saltcrete embedding. b: After retrieval.

5.5 Gas Sampling Filters

For gas sampling from the heated backfill, permeable glass filters had been installed at the surface of the central heater casks, at the drift roof, and at the drift floor (Fig. 5.5.1). Each sampling point had been connected with a Teflon tube leading to the entrance of the test drifts where gas samples had been taken periodically by a membrane pump.

During the heating phase, sampling was generally satisfactory, but several gas sampling points had to be shut down. With the post-test analyses, the failure reasons were checked which could have been either plugged glass filters or damaged Teflon tubes.

During drift excavation, 12 glass filters were retrieved from cross sections A and B. Four filters were shipped to the manufacturer (Tab. 5.9 and Fig. 5.5.2). At the sampling points B/A4 and B/B4, gas sampling had been possible until the end of the *in-situ* test. The sampling points B/A2 and B/A3, however, had to be shut down during the heating phase.

Tab. 5.9 Retrieved gas sampling filters

MCS	Position	Gauge Identification	Status before Retrieval	Evaluation
B	roof (drift centre)	B / B4	gas sampling possible	glass filter ok.
A	cask surface (right) cask surface (top) roof (drift centre)	B / A2 B / A3 B / A4	gas sampling not possible gas sampling not possible gas sampling possible	glass filter ok. glass filter ok. glass filter ok.

At the manufacturer, the permeability to air of the gas sampling filters was checked by a flowmeter at a flow rate of 0.06 norm litres per minute. The examination revealed that the filters were not plugged, but still permeable and had no loss of flow. Consequently, the failure of the gas sampling points B/A2 and B/A3 was ascribed to damaged Teflon tubes.

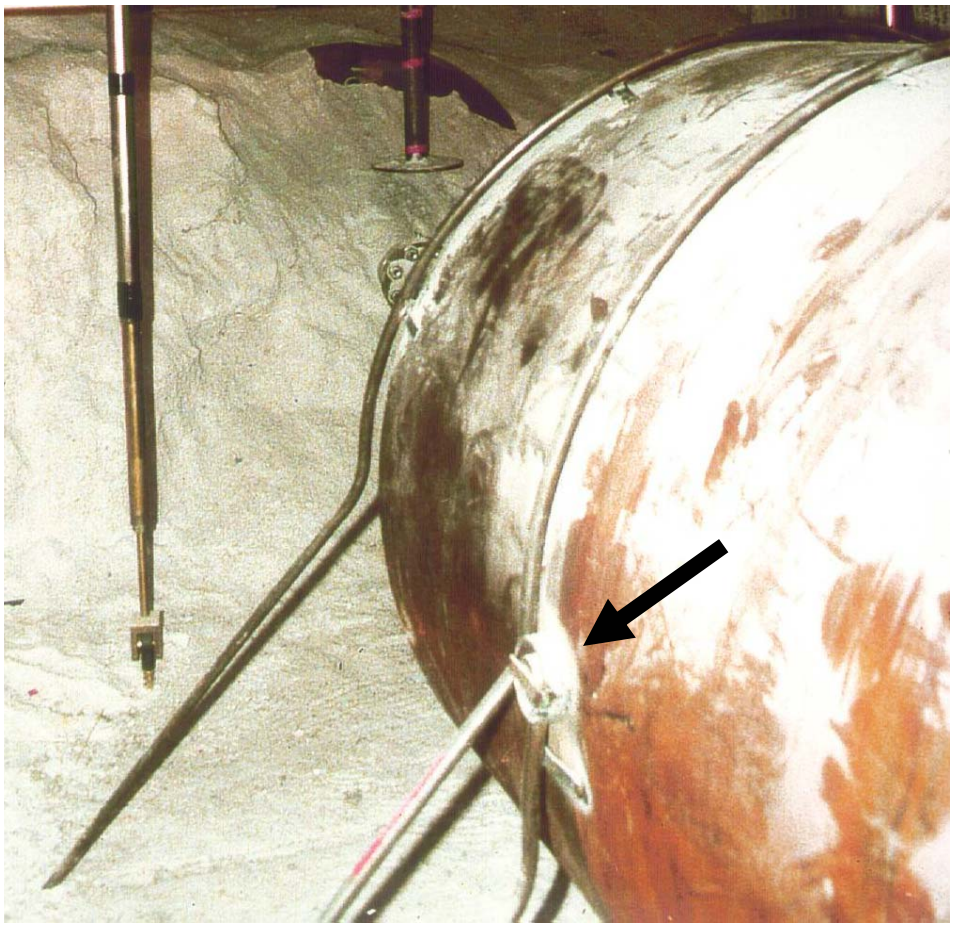

Fig. 5.5.1 Gas sampling filter *in situ* (welded at the heater cask surface)

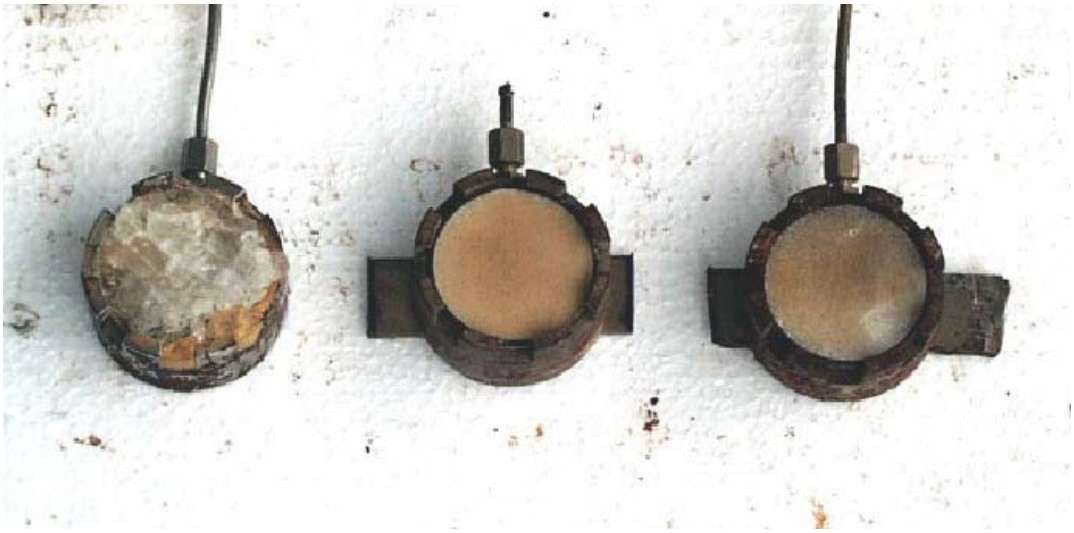

Fig. 5.5.2 Retrieved gas sampling filters B/A2, B/A3, and B/A4

6 Comparison of Objectives and Results

The objectives of the post-test evaluation programme of the TSDE project focused on test field excavation to enable sampling for post-test laboratory analysis of the achieved degree of backfill compaction and to inspect and re-calibrate the measuring instruments after more than a decade of operation for validation of the most valuable measuring results.

Regarding backfill sampling, the objective was completely achieved. On the basis of preliminary results, additional sampling cross sections were determined in the course of the project and the post-test analysis programme was enlarged.

Unfortunately, until re-opening of the test field and termination of the post-test laboratory analyses of the compacted backfill, measurements and predicted data could not be directly compared because the data which had been calculated with a 2D-model were only valid for the central part of the test field where plane symmetry prevailed. But the corresponding measuring data for this very warm part of the test field were not available due to early instrument failures. Therefore, measuring data from the peripheral part of the heated area had to be taken to assess the compaction rates during the heating phase (Fig. 1.3, cf. Section 1). The only possibility to check the real situation at the termination of the test was a careful analysis of the porosity distribution in the central part of the test field (cf. Section 4.1). The outcome of this analysis was extremely valuable for the whole project as the predicted data were impressively confirmed by the post-test data from the central part of the test field.

To enable a new comparison of measured and predicted data over the whole experiment duration, new porosity data were determined for the central part of the heated area. The new calculation based on the convergence data from cross section G1, which had been almost identical to the measurements in the central cross section B^{+1} until the failure of the convergence measuring devices in section B^{+1} after two years of heating. These data were additionally corrected by application of a new approach for the determination of the average *in-situ* porosity from the drift closure measurements, which is taking into account the volume of the incompressible heater cask in the backfill. The *in-situ* porosities determined in this way showed a much better agreement with the predicted data (Fig. 6.1) and confirmed the used models excellently. Thus, the objective of the post-test backfill analysis can be considered completely achieved.

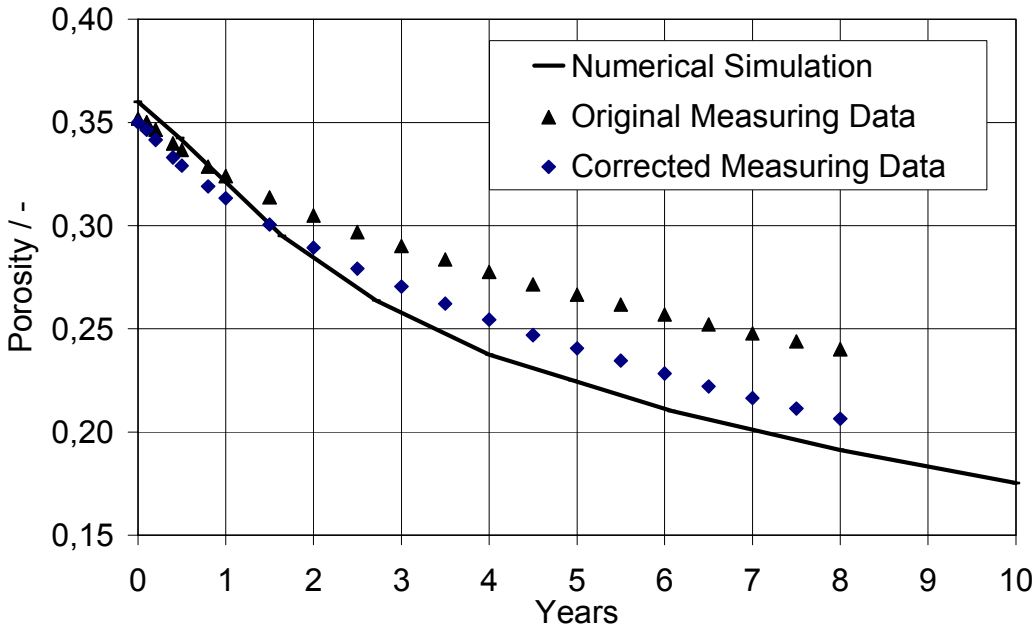

Fig. 6.1 Comparison of original and corrected porosity measuring data with predicted data

Post-test laboratory compaction tests on the pre-compacted backfill material have shown that large samples represent the backfill mass quite well. A comparison with data obtained by other investigators on non-consolidated material showed a good agreement of the strength behaviour (Fig. 4.2.12, cf. Section 4.2.2), thus confirming former laboratory data used to develop the constitutive models and the respective material parameters. Accordingly, this objective was achieved satisfactorily, too.

Post-test analyses of the measuring instruments yielded extremely useful experience in instrument and cable design for the operational and post-operational monitoring of a salt repository. Representative numbers of instruments could be recovered from the backfill after more than a decade of operation. Most instruments were re-calibrated successfully. The calibration results showed that most sensors were still functioning excellently at the termination of the test. It could be demonstrated that sensor drifts were low and their linearity was still within the respective limit of tolerance. This result is encouraging and the objective regarding instrument assessment for future deployment in a salt repository was also achieved.

7 Summary and Conclusions

Hydraulic Properties

With the porosity determinations, the results of the *in-situ* measurements were confirmed. The post-test analyses showed a decreasing porosity from the drift entrance towards the centre of the test field ranging from 0.31 to 0.19 on average. At the cask/backfill-interface, porosity values down to 0.135 were determined.

In the non-heated area, the porosity decreased from the floor to the roof. Obviously, this trend was caused by the slinger technique which had been used for drift backfilling leading to a high grade of sorting on the bottom of the drifts, but a low grade of sorting towards the top. A high grade of sorting implies a high porosity and a low density. By grain size analyzes, this assumption could be proved. Due to the inhomogeneous grain size distribution, variations of the thermomechanical and hydromechanical backfill properties are evident.

Porosity determinations around the heater casks, however, revealed a different situation showing increasing porosity values from the floor to the roof. The lower porosity at the heater cask level is explained by the smaller backfill volume which was affected by drift closure due to the presence of the cask leading to a higher backfill compaction.

In the central heater area, the post-test analyses revealed lower porosity values than derived from drift closure measurements. But with a new approach for the determination of the average *in-situ* porosity from the drift closure measurements, which takes into account the heater casks, the resulting porosity values were lower and in good agreement with the post-test values.

From permeability measurements on backfill samples, values in the range of 1E-11 m² were obtained. The results are corresponding to the value derived *in situ* during the heating period thus confirming the applied method for permeability determination.

From additional permeability tests on large core samples at different porosities that were reached by increasing hydrostatic load, a relation between permeability and porosity of $k = 1E\text{-}11 \cdot \Phi^{1.8}$ was determined. The results were compared with previous

tests on TSDE backfill samples and *in-situ* measurements. By fitting all data, a permeability – porosity relation of $k = 8E\text{-}11 \cdot \Phi^{2.5}$ was determined.

Mechanical Properties

Under laboratory conditions (ambient temperature and high compaction rates), an *in-situ* backfill pressure of 4.0 to 4.5 MPa was determined from hydrostatic compression tests, which was higher than the value of 2 to 4 MPa that had been observed *in situ* at higher temperatures and very low compaction rates. Beyond this backfill pressure, non-linear plastic compaction appeared following the normal compaction of initially loose backfill.

From the deviatoric compression tests, the stress – strain behaviour was obtained indicating very large deformation even after the peak strength was reached. The major component of the deformation was plastic. Volume increase or dilatancy of the compacted backfill was not significant under the imposed test conditions.

Comparisons with other laboratory results on Asse crushed salt allow an evaluation of the strength of the compacted TSDE backfill. Increasing strength is observed with decreasing grain size and with a higher initial density for the same grain size. Increasing temperature results in an increase in cohesion. Generally, the cohesion of crushed salt at ambient temperature is less than 0.6 MPa, and the internal friction angle is between 43°and 53°.

Chemical and Mineralogical Properties

Mineralogical investigations by optical microscopy and Scanning Electron microscopy (SEM) reveal a heterogeneous grain size distribution as well as a very high porosity of the TSDE crushed salt backfill material. Additionally, the cathodoluminescence method (CL) and neutron texture analysis using a diffractometer were applied for testing their applicability. Both methods proved to be promising for compacted crushed salt fabric analysis.

The observations and quantifications of microstructures and textures do not confirm the initial assumption of plastic deformation and/or dynamic or static recrystallization of salt grains. Preferred orientations can be seen in some domains, but cannot be confirmed

for the whole specimen. A grain-shape-preferred orientation based on the sedimentation process during backfilling cannot be verified.

Recrystallization, as known for solid rock salt, is not to be expected in the investigated crushed salt backfill, because grain-to-grain contacts only exist to a limited extent. Accordingly, grain boundary migration is not very likely.

Investigations must still be conducted into the processes that led to sintering/compaction of the backfill material. However, to conduct these examinations, sample preparation techniques must be improved. A question remains whether the observed grain domains were generated during the backfilling process or if there are domains in which accelerated sintering and compaction took place, i.e., if a sort of nuclei were existing. Furthermore, work is proposed to concentrate on distinct domain characterization and on identifying the time of their development.

Certainly, however, the observed compaction of the crushed salt can simply be explained by the breaking off of salt crystals as a result of the load induced by drift closure.

On backfill samples from the heated area, a residual water content of 0.03 to 0.05 wt% was determined which is identical to the average water content of rock salt. The residual gas concentrations corresponded to normal mine air. The carbon dioxide content was much lower than the maximum value of almost 1 % observed during the heating phase. Both hydrogen, which had probably been generated by corrosion of the heater casks, and methane, which had been released from the rock salt during heating, had completely vanished.

Instrument Performance and Analysis

Originally, the measuring equipment had been designed for a three to five years testing period, but was operated over almost ten years under final repository conditions. As expected, an increasing number of instruments failed during the long testing period. Therefore, the layout of the measuring systems had been designed redundantly.

In-situ test and post-test investigations revealed that the robust gauge design and the deployed sensors were very successful despite the harsh environment. Most failures were caused by damaged measuring lines. Especially, the multicore cable design

cannot be recommended for *in-situ* measurements in heated areas. A single cable design is more appropriate. The realized cable duct design is not recommended. As all measuring lines were enclosed in these cable ducts near the roof, local damage caused significant failures. Better protection of the measuring lines could be achieved by cable slots along the drift wall where rock deformation is not too high. For future experiments or the safety monitoring of a repository, the protection of the measuring lines is vital.

The re-calibration results proved the high reliability and low sensor drift of the applied sensors. After more than a decade of operation, the linearity of most gauges was still within the manufacturer's respective limit of tolerance. Especially, the linearity of the extensometer sensors hardly changed during operation. Therefore, the reverse extensometer design with the displacement transducers inside a tight instrument head in the deepest part of the borehole can be recommended for further application in heated areas. Even after high temperature histories of some drift convergence measuring gauges, the sensor drift was largely within the manufacturer's limit of tolerance. Significant deviations were observed only for the drift convergence devices which had been installed directly above the heater casks.

For backfill pressure measurements under harsh conditions, the robust Glötzl hydraulic pressure cells proved to be very reliable in the prevailing pressure range. The intricate AWID measuring equipment, however, is reasonable only for special applications. Satisfactory results had been obtained from the gas sampling systems. The applied gas sampling filters and Teflon tubes can be recommended.

Generally, dismantling of the test field and retrieving of the measuring equipment is recommended for any *in-situ* experiment with no maintenance possibilities. For quality assurance, sensor calibration before and after an *in-situ* test is indispensable. Basing on the post-test analyses, the *in-situ* measurements of the TSDE test could be assessed as very confidential. The applied measuring systems proved to be suitable for the long-term monitoring of a final repository.

References

/BEC 99/ BECHTHOLD, W., ROTHFUCHS, T., POLEY, A., GHOREYCHI, M., HEUSERMANN, S., GENS, A., OLIVELLA, S.: Backfilling and Sealing of Underground Repositories for Radioactive Waste in Salt (BAMBUS Project), Final Report, EUR 19124 EN, Brussels, 1999

/DIE 89/ DIEKMANN, N., SCHNIER, H.: Geotechnische Erkundung und Standsicherheitskriterien Bergwerk Gorleben, BGR-Abschlußbericht, 1989

/DRO 96/ DROSTE, J., FEDDERSEN, H.-K., ROTHFUCHS, T., ZIMMER, U.: The TSS-Project: Thermal Simulation of Drift Emplacement, Final Report Phase 2, Gesellschaft für Anlagen- und Reaktorsicherheit (GRS) mbH, GRS-127, 1996

/DRO 01/ DROSTE, J., FEDDERSEN, H.-K., ROTHFUCHS, T.: Experimental Investigations on the Backfill Behaviour in Disposal Drifts in Rock Salt (VVS-Project), Final Report, Gesellschaft für Anlagen- und Reaktorsicherheit (GRS) mbH, GRS-173, 2001

/JOC 81/ JOCKWER, N.: Laboratory investigation of water content within rock salt and its behaviour in a temperature field of disposed high-level waste, Proceedings Scientific basis for nuclear waste management, Vol. 3, Plenum publishing corporation, 1981

/LEI 03/ LEISS, B., ULLEMEYER, K.: Untersuchung von Textur und Kornstruktur aufgeheizter Versatzproben aus dem TSS-Versuchsfeld im Forschungsbergwerk Asse – Probe VVS-A-MI8, Ergebnisbericht zur Pilotstudie, Universität Göttingen, Institut für Strukturgeologie und Geodynamik, Göttingen, 2003

/NAT 91/ NATAU, O., KELLER, S.: Grundlagenuntersuchungen zu Salzhaufwerk mit Korndurchmessern bis 65 mm in Abhängigkeit von der Lagerungsdichte und des Spannungsniveaus, Forschungsbericht 02E80401, 1991

/PUD 98/ PUDEWILLS, A.: Thermomechanical analysis of the TSS experiment, Proc. Intern. Congr. Underground Construction in Modern Infrastructure, Stockholm-Sweden, June 7-9, 1998, Balkema Rotterdam, pp. 317-323.

/ROT 99/ ROTHFUCHS, T., FEDDERSEN, H.-K., KROEHN, K.-P., MIEHE, R., WIECZOREK, K., POLEY, A.: The DEBORA-Project: Development of Borehole Seals for High-Level Radioactive Waste – Phase II, Final Report, Gesellschaft für Anlagen- und Reaktorsicherheit (GRS) mbH, GRS-161, 1999

/ROT 01/ ROTHFUCHS, T., DROSTE, J., ZHANG, C.-L.: Determination of Coupled hydraulic-mechanical properties of salt backfill: Post-test analyses of *in-situ* measurements in the Asse mine, Proceedings EUROSAFE Paris 2001, 5 - 6 November 2001

/STE 00/ STEININGER, W.: Subtask – Laboratory Benchmark, WP I Backfill, 10.2000

/STU 95/ STÜHRENBERG, D., ZHANG, C.-L.: Results of experiments on the compaction and permeability behaviour of crushed salt, Proceedings 5th Conference on Radioactive Waste Management and Environmental Remediation, Berlin, 1995

/TPL 93/ Testplan zum Demonstrationsversuch "Thermische Simulation der Streckenlagerung" im Salzbergwerk Asse (Revidierte Fassung)" (1993), Hauptband, Kernforschungszentrum Karlsruhe.

/ULL 98/ ULLEMEYER, K., SPALTHOFF, P., HEINITZ, J., ISAKOV, N. N., NIKITIN, A. N., WEBER, K.: The SKAT texture diffractometer at the pulsed reactor IBR-2 at Dubna: experimental layout and first measurements, Nucl. Instr. Meth. Phys. Res. A412/1, 80-88, 1998

/URA 87/ URAI, J. L., SPIERS, C. J., PEACH, C. J., FRANSSEN, R. C. M. W., LIEZENBERG, J. L.: Deformation mechanism operating in naturally deformed halite rocks as deduced from microstructural investigations, Geologie en Mijnbouw, 66, 165-176, 1987

/ZHA 93/ ZHANG, C.-L., HEEMANN, U., SCHMIDT, M. W., STAUPENDAHL, G.: Constitutive model for description of compaction behaviour of crushed salt, Proceedings ISRM International Symposium, EUROCK 93, Lisbon, 1993

/ZHA 01/ ZHANG, C.-L., DITTRICH, J., ROTHFUCHS, T.: Laboratory Benchmark Tests on Crushed Salt, Test Report, Gesellschaft für Anlagen- und Reaktorsicherheit (GRS) mbH, 2001

List of Figures

List of Tables

Gesellschaft für Anlagen- und Reaktorsicherheit (GRS) mbH

Schwertnergasse 1
50667 Köln
Telefon +49 221 2068-0
Telefax +49 221 2068-888

Forschungsinstitute
85748 Garching b. München
Telefon +49 89 32004-0
Telefax +49 89 32004-300

Kurfürstendamm 200
10719 Berlin
Telefon +49 30 88589-0
Telefax +49 30 88589-111

Theodor-Heuss-Straße 4
38122 Braunschweig
Telefon +49 531 8012-0
Telefax +49 531 8012-200

www.grs.de

ISBN 3-931995-62-3